Development of a handheld confocal microscope for fluorescence-guided neurosurgery

Linpeng Wei

A dissertation
submitted in partial fulfillment of the
requirements for the degree of

Doctor of Philosophy

University of Washington
2019

Reading committee:
Jonathan T.C. Liu, Chair
Lih Y. Lin
Per G. Reinhall

Program Authorized to Offer Degree:
Mechanical Engineering

University of Washington

Abstract

Development of a handheld confocal microscope for fluorescence-guided neurosurgery

Linpeng Wei

Chair of the Supervisory Committee:
Bryan T. McMinn Endowed Associate Professor Jonathan T.C. Liu
Department of Mechanical Engineering

Surgery remains a critical step in the standard-of-care of many brain tumors, and the ability to identify tumor margins intraoperatively is central to achieving maximal tumor resection with minimal neurological damage. Unfortunately, the tumor boundary is often ambiguous under current imaging techniques for neurosurgical guidance (e.g. MRI and wide-field microscopy) due to their limited resolutions, and the assessment of tumor-brain interface can only be definite via slide-based histopathology, an invasive and laborious post-operative procedure. In recent years, there is a growing interest in developing handheld confocal fluorescence microscopy as a non-invasive and real-time imaging tool to distinguish normal and abnormal tissue with sub-cellular precision, ultimately improving the completeness of tumor resection. Although intraoperative confocal microscopes are commercially available, they typically provide either limited frame rates or suboptimal resolutions. In light of these concerns, we have developed a novel handheld confocal microscope for neurosurgical guidance based on the line-scanned dual-axis confocal (LS-DAC)

architecture, a more recent optical-sectioning design that provides both high-speed and high-resolution tissue imaging. This manuscript documents the development of the device, including 1) an early-stage feasibility study utilizing a tabletop prototype, 2) hardware and software development of the handheld device, with fully packaging into a clinically viable imaging system, 3) performance evaluation and optimization using animal models, and 4) a pilot clinical study collaborating with neurosurgeons to image human brain tumors. In the final chapter, a proposed surgical workflow is provided for the future clinical use of this device, along with a detailed discussion on the remaining challenges for the clinical acceptance of this new technology as a routine imaging tool for neurosurgical guidance.

Acknowledgment

This work would not have been possible without the support and guidance provided by my advisor, Professor Jonathan Liu. I am extremely grateful for having a mentor like him, who is always willing to spend time meeting with students, and providing them with timely and insightful advice on their research, communication skills, and career development. I would also like to express my gratitude to Professors Per Reinhall, Lih Lin, and Suzie Pun, for serving on my thesis committee as well as for their encouragement and help that elevates my thesis to a higher level. Thanks to Wanwisa Kisalang for being a knowledgeable and thoughtful counselor throughout my Ph.D. training at UW. I would like to thank neurosurgeons Drs. Nader Sanai and Yoko Fujita, and neuropathologist Dr. PJ Cimino, for their help with the clinical studies and their valuable feedbacks on my work from their perspectives as clinicians. It has also been a great pleasure working with and learning from my colleagues at the molecular biophotonics lab. Finally, I would like to thank my parents for everything. None of this would have been possible without their love and encouragement.

Table of Contents

List of Figures

LIST OF TABLES

Chapter 1: Introduction

1.1 Clinical needs

Gliomas are the most common primary malignant brain tumor in adults, and are considered one of the deadliest cancers. Patients with glioblastoma (World Health Organization [WHO] Grade IV glioma) have a median survival of 14.6 months and a 2-year survival rate of 26%, even when optimal treatment is provided. In the current standard-of-care, surgery remains the first step in effective management of all gliomas, in which the primary objective is to maximize the extent of resection while avoiding neurological damage [1, 2]. Mounting evidence suggests that more extensive neurosurgical resection of low- and high-grade gliomas is associated with increased overall survival and life quality of the patients [3-10]. Unfortunately, most patients do not receive an optimal extent of resection due to the diffusive nature of glioma cells, in which the tumor margins are indistinguishable from the surrounding normal brain with conventional visualization method, namely, visual inspection with standard low-power white-light surgical microscopes [11]. To improve glioma resection, a number of intraoperative techniques are currently in use. These include intraoperative neuronavigation based on pre-operative magnetic resonance imaging (MRI), intraoperative ultrasonography, and intraoperative MRI [1]. Of these methods, intraoperative neuronavigation – despite being well-known for shortcomings such as brain shift [12] – has emerged as a standard-of-care, whereas intraoperative ultrasonography and intraoperative MRI remain uncommon due to the high cost and/or technical expertise required [1]. However, despite the availability of these technologies, the reported rates of gross-total resection (GTR) – the complete resection of contrast-enhancing region based on post-operative MRI – remains low: ranging from 14-46% for low-grade gliomas (LGGs) [13-21] and 33-76% for high-grade gliomas (HGGs) [22-26]. A fundamental limitation of these low-power wide-field imaging techniques is that each pixel (i.e. the resolvable spot) in a low-resolution image represents an average over many cells, thus lacking the spatial resolution and the sensitivity to detect disseminated tumor cell populations at the tumor margins [27]. While frozen-section pathology has been routinely used to provide preliminary diagnosis during the course of glioma resection, this strategy is invasive (requires biopsy), time consuming (> 20 mins), and is known for introducing artifacts and sampling errors. Over and above the goal of achieving GTR, there is a need to visualize and quantify tumor burden beyond the radiographic margins, as it is well known that glioma cells infiltrate beyond the regions of MRI contrast-enhancement [28] (Figure 1.1).

-- **Figure 1.1** --

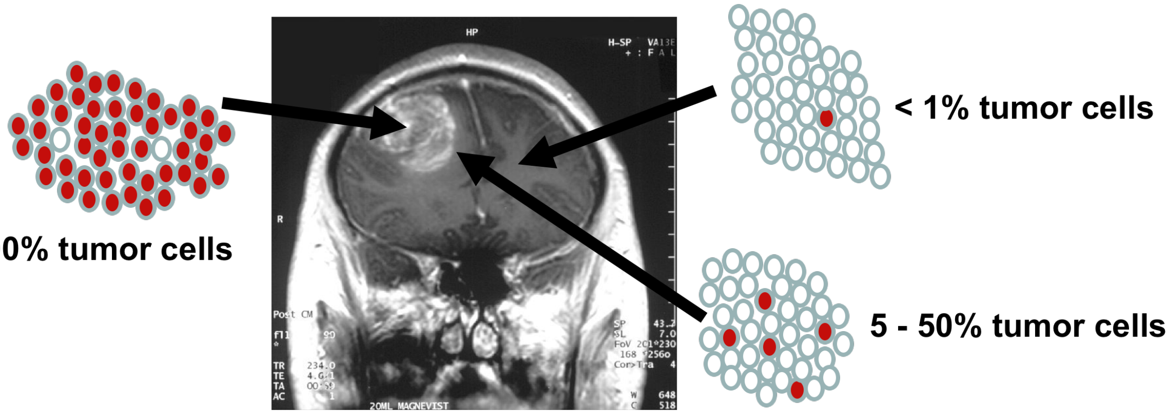

Figure 1.1 Simplified illustration of the distribution of tumor cells in glioma patients. The tumor margins are ambiguous since there is a gradient in the ratio of tumor to normal cells as a function of distance from the tumor core, with disseminated cell populations at the margins.

1.2 Fluorescence-guided surgery (FGS): an emerging technique

The idea of using fluorescence to improve visualization of abnormal cells with respect to the surrounding normal brain tissues is not new. It can be dated to 1948 when Moore reported the first fluorescence-guided neurosurgery using fluorescein [29, 30], a non-toxic fluorescent contrast agent that is now widely used for many *in vivo* applications in human. However, the efficacy of fluorescein-guided neurosurgery remains controversial over the past decades, because fluorescein does not show specific affinity to tumor cells [31, 32]. In recently years, the advancements of intraoperative imaging technologies and fluorescence contrast agents provide new opportunities for this old technique to improve brain tumor resections [28, 33-35] (Figure 1.2). For example, the adaptation of high-resolution optical-sectioning microscopy (e.g. confocal or two-photon microscopy) for neurosurgical guidance as a non-invasive real-time alternative for conventional neuropathological examination has emerged as an active research area [36-42]. In 2011, a pilot study led by Sanai first demonstrated the feasibility of using a confocal fluorescence endoscope (i.e. the Optiscan® system, now rebranded as the Convivo® system, commercially available through ZEISS®) for neurosurgical guidance, and successfully identified cancer-indicating histopathological features (e.g. vascular neoproliferation, neuronal satellitosis, *etc.*) with contrast provided by fluorescein. When used in guiding neurosurgery, fluorescein is typically administrated through intravenous injection right before imaging, providing a sharp contrast of the bright vasculature over a dark background to the normal brain [36]. In regions where the blood-brain barrier (BBB) is disturbed (e.g. the angiogenic or the enhancing regions of malignant gliomas), fluorescein leaks into the extracellular space, providing a bright background that contrast against the cells and other tissue structures that appear as dark shadows with different grayscale levels [31, 43]. In a follow-up blinded clinical study, diagnoses based on the cytoarchitecture and microvasculature of intraoperative confocal images showed a 92.9% accuracy when compared to the gold-standard approach [44].

In recent years, numerous reports have detailed the benefits of FGS for HGG resection using 5-aminolevulinic acid (5-ALA), the first ever metabolic (i.e. targeted) optical imaging agent approved by the United States Food and Drug Administration (U.S. FDA) for neurosurgical guidance. In brain tumor patients, 5-ALA has been used as an orally administered prodrug that is intra-cellularly metabolized by mitochondria to become the fluorescent molecule protoporphyrin IX (PpIX). This heme-synthesis pathway substrate accumulates preferentially in glioma cells and epithelial tissues, emitting red fluorescence (λ_{em} = 600-700 nm) when excited with violet light (λ_{ex} = 400-410 nm). A landmark phase III clinical trial in Europe led by Stummer demonstrated that the use of this technique in HGG surgery resulted in higher rates of GTR (65% vs. 36%) and 6-month progression-free survival (41% vs. 21.1%) compared to the control groups [45]. While this visualization method (i.e. standard wide-field surgical microscope) is simple and is effective in detecting strong fluorescence from HGG, it is less effective for identifying residual tumor infiltration beyond MRI contrast-enhancing regions, where the fluorescence signal declines (presumably due to a reduction of tumor cell density and PpIX levels). This method is also less effective in guiding the resection of LGGs, which often do not generate sufficient PpIX fluorescence to enable detection by conventional visualization technologies. Fortunately, it has been shown that with more advanced visualization technologies, intraoperative detection of PpIX fluorescence in LGGs [11, 46], at infiltrative margins [47-49], and from sub-surface tumors [50-56] is possible, potentially extending the utility of 5-ALA-based FGS. The recent FDA approval of 5-ALA-based neurosurgery in 2017 presents a timely opportunity to develop high-sensitivity molecular imaging technology to further improve the effectiveness of this emerging technique.

-- **Figure 1.2** --

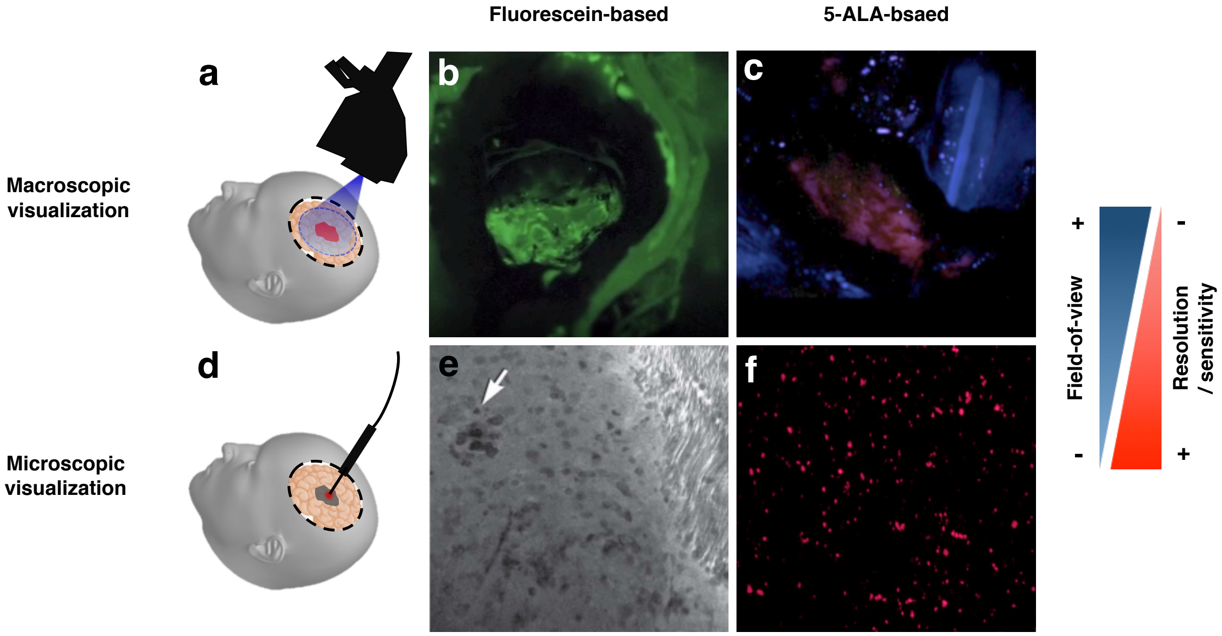

Figure 1.2 Overview and comparison of common visualization technologies for of fluorescence-guided neurosurgery. (a) Imaging methods based on free-standing microscopes typically provide the macroscopic fluorescence expression over a large field-of-view that can cover the entire surgical cavity. (b) Example image of macroscopic fluorescein accumulation in brain tumor, where the BBB is disrupted. (c) Example image of macroscopic accumulation of 5-ALA-induced PpIX fluorescence in a HGG case. The pink fluorescing region corresponds to the bulk tumor while the blue back-reflected light is from the illumination source at ~405 nm. (d) Alternatively, the fluorescence signal can be visualized with probe-based high-resolution methods, which are designed to be placed very close to, or in direct contact with the tissue surface, providing a number of advantages such as flexibility to access difficult-to-reach locations within the tumor cavity, and high optical-detection sensitivity, at the trade-off of a reduced field-of-view. (e) Example of microscopic visualization of the cytoarchitecture of brain tumors using fluorescein as the contrast agent, showing a neuronal satellitosis, which is an indicator of maglinant tumor. (f) Example of microscopic (sub-celluалr) expression of PpIX fluorescence using a high-resolution optical-sectioning microscope.

1.3 Current visualization technology for FGS

Visualization technologies for 5-ALA-induced PpIX fluorescence in gliomas can be grouped into free-standing systems and probe-based systems. Free-standing imaging systems consist of standard wide-field (WF) operating microscopes (e.g. ZEISS Pentero®, Leica M530®, *etc.*) or other custom microscopes that operate on a similar principle: namely, by illuminating a large field (usually the entire surgical cavity) at one excitation wavelength while imaging the resultant fluorescence signal onto a detector array (camera), or through an eyepiece, to the unaided eyes of the surgeon. Such techniques have the advantage of providing a large field-of-view (FOV), but are incapable of visualizing individual cells due to a trade-off between FOV and spatial resolution. Since each pixel of a low-resolution WF image represents an average signal from a large number of cells, all of which can produce non-specific autofluorescence and other background fluorescence, the sensitivity to detect sparse fluorescently labeled cell populations (e.g. disseminated tumor cells at the margins) is reduced (Figure 1.3a). In addition, the long working distance of free-standing surgical microscopes results in a further reduction in optical detection sensitivity (the inverse-square law). In contrast to free-standing microscopes, probe-based imaging systems are designed to provide a higher-magnification view of localized regions within the surgical site, with FOVs ranging from sub-millimeter to centimeter scales. Probe-based methods in general imply higher sensitivity because the probes are designed to be placed very close to (a few millimeters at most) or in direct contact with the tissue surface, resulting in more efficient light delivery and collection compared to non-contact visualization methods [57] (Figure 1.3b). This section provides a brief discussion of the strengths and weaknesses of the current technologies for intraoperative fluorescence visualization in neurosurgery.

-- **Figure 1.3** --

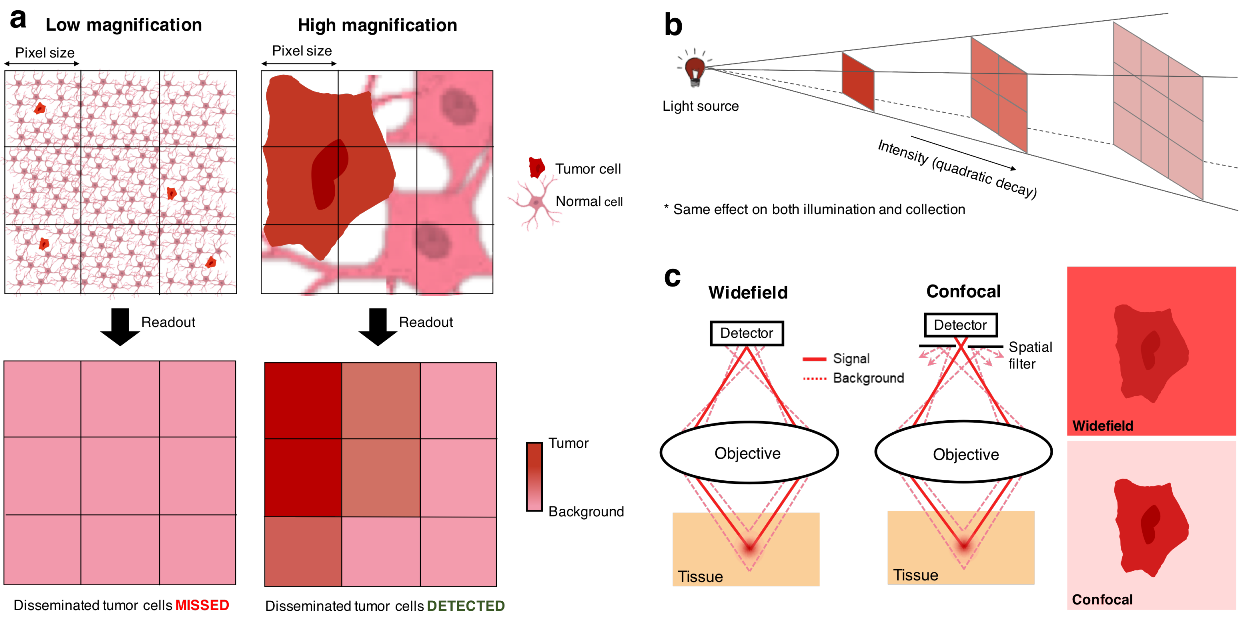

Figure 1.3 Factors that affect the sensitivity of fluorescence-based tumor detection. (a) The "averaging effect" due to low spatial resolution reduces the signal-to-background ratio of optical detection, which therefore reduces the ability to detect sparse disseminated tumor cells that exhibit a differentially higher level of fluorescence compared to the adjacent normal cells. (b) A longer working distance is typically associated with reduced sensitivity due to a reduction in signal collection with distance according to the inverse-square law. (c) Wide-field imaging in thick tissue is subject to a strong background due to insufficient rejection of out-of-focus and multiply scattered light. High-resolution optical-sectioning techniques, such as confocal microscopy, can enable sensitive detection of individually labeled cells and sub-cellular features.

1.3.1 Wide-field surgical microscopy

The first report on 5-ALA-based FGS of gliomas was published in 1998 by Stummer and colleagues in Germany [58, 59]. The benefits of this method were subsequently demonstrated and documented in a collection of reports from around the world, prompting the development of commercial wide-field fluorescence microscopy systems (e.g. ZEISS Blue400® and Leica FL400®)

for 5-ALA-based FGS. These systems consist of add-on modules to existing white-light surgical microscopes (e.g. ZEISS Pentero® and Leica M530®, respectively) with optimized filter sets for inducing and collecting PpIX fluorescence. For example, the Blue400® module consists of a filter set that provides an excitation wavelength at 400-410 nm and a collection wavelength at 620-710 nm, both of which are optimally matched to the excitation and emission spectra of PpIX. In comparison to the early systems used by Stummer *et al.* in 1998 (λ_{ex} = 375-440 nm; λ_{em} => 455 nm), the newer systems provide higher excitation efficiency as well as superior rejection of autofluorescence background and back-scattered excitation light, therefore improving the image contrast.

As a commercialized technology for 5-ALA-based FGS, free-standing WF surgical microscopy provides a straightforward and intuitive means to visualize macroscopic PpIX fluorescence in real time over a large FOV. However, as previously mentioned within this manuscript and other reports, this method has several limitations [28, 35, 57, 60, 61]. First, WF imaging often does not provide sufficient resolution or sensitivity to visualize sparse foci of fluorescence, such as the weak sub-cellular distribution of PpIX in LGGs and disseminated tumor cells at the diffuse margins of all gliomas. Second, WF imaging in thick tissue is subject to high levels of background signal due to the inefficient rejection of out-of-focus light, further reducing its sensitivity to detect weak fluorescence (Figure 1.3c). Third, there is often a steep angle of incidence between the focal plane of standard operating microscopes and the walls of a resection cavity, which results in defocused regions and blind spots, especially within sulci and behind bends. Finally, almost all current WF techniques for visualizing of PpIX fluorescence are not quantitative but rather rely upon the subjective judgements of the surgeon to determine what colors and intensities correspond to tumor, benign, and/or mixed cell populations. In short, since the detected fluorescence signal is influenced by a number of parameters such as tissue optical properties (e.g. scattering and absorption) and non-specific auto-fluorescence background, there is a nonlinear and often non-intuitive relationship between the detected fluorescence signal and actual fluorophore concentrations.

1.3.2 Wide-field fluorescence endoscopy

Initial efforts to develop endoscopic probes for 5-ALA-based FGS aimed to provide visualization of PpIX fluorescence from deep-seated tumors and other regions that are not easily accessed by standard free-standing surgical microscopes. In general, the detection sensitivity of such endoscopic imaging probes is superior to that of conventional surgical microscopes due to the shorter working distance of the miniature probes that are positioned much more closely to the tissue surface, but at the cost of a reduced FOV. In 2007, Tamura and colleagues reported on the use of a modified commercial endoscope to visualize PpIX fluorescence in an intraventricular malignant glioma and used this method to obtain an image-guided biopsy that was confirmed malignant by gold-standard histopathology [62]. As noted by the authors, the main modifications made to the endoscopic system, to enable PpIX visualization, were the use of a high power (300 mW) 405-nm laser source in addition to a high-sensitivity charge-coupled device (CCD) camera. This study did not report the effect of photo-bleaching, but it should be noted that the illumination power used was significantly higher than in other studies in which photo-bleaching was observed [47, 63]. At around the same time, Potapov and colleagues performed a pilot study using a custom endoscope (now commercially available through Karl Storz®) to visualize PpIX fluorescence in 17 patients (mostly grade IV gliomas) [64]. According to the surgeons involved in the study, the endoscope allowed for more-thorough inspection of the surgical cavity without applying traction to the brain tissue (the practice of using surgical tools to reveal blind spots, which can potentially be harmful to the patient). More recently, Belykh and colleagues showed that the use of a scanning fiber endoscope (SFE) enabled the detection of PpIX fluorescence near the margin of an infiltrative glioma in a preclinical mouse model for which the fluorescence level was below the detection limit of a standard WF operating microscope [47]. The SFE technology utilizes an innovative scanning mechanism to rapidly actuate a single-mode fiber tip, allowing for high-resolution imaging (spatial resolution of ~20 μm) at video rate with a compact probe head (Ø ~2 mm).

1.3.3 Quantitative spectroscopy

As previously mentioned, the raw intensity detected by a fluorescence microscope can be misleading because it is affected by tissue-dependent optical properties such as light absorption and scattering, as well as optical detection parameters such as working distance and angle of detection. Unlike fluorescence microscopy, which measures the total signal within a relatively broad range of wavelengths (tens to hundreds of nanometers), spectroscopy measures the signal within individual wavelength bins over a wide spectrum. Studies have shown that this spectrally resolved fluorescence signal can be used to infer certain tissue optical properties with the aid of numerical models, resulting in more accurate and more sensitive measurements of the relative, or in some implementations, absolute concentration of fluorophores such as PpIX. A number of different spectroscopic probes have been developed by research groups and companies for 5-ALA-based FGS of gliomas [65-69], and have also been demonstrated in a collection of clinical studies to improve the sensitivity of PpIX fluorescence detection in patients with LGGs [46, 65, 70]. In addition to providing more accurate and linear measurements of PpIX concentration, these spectroscopic probes share the advantages of other probe-based imaging modalities such as flexibility and improved sensitivity compared to free-standing imaging methods.

As mentioned in the previous paragraph, probe-based spectroscopy can provide accurate quantification of PpIX concentration at localized points of interests, and it is technically challenging to achieve PpIX quantification across an entire surgical cavity. In 2012, however, Valdes and colleagues developed a WF imaging version of intraoperative spectroscopy to quantify PpIX concentrations over a large and spatially resolved FOV (i.e. a PpIX heat map) at low magnification [48, 71]. This system was based on a standard surgical microscope (ZEISS Pentero®), in which the main modification was the placement of a liquid crystal tunable filter in front of a monochrome digital camera to achieve spectrally resolved detection over time. A trade-off is that the frame rate was limited to ~1 Hz to achieve sufficient spectral resolution and signal-to-noise ratio (SNR) for a spectrally resolved image over a large area [48, 71]. More recently, refined algorithms have been developed to process these hyperspectral images, in which improved sensitivity and accuracy of PpIX quantification has been demonstrated in image phantoms and in patients [72].

1.3.4 Deep-tissue imaging techniques

Deep-tissue imaging is desirable to detect tumor infiltrates and residual tumors below the surgical margin, but visualizing PpIX fluorescence at depth is challenging due to the fact that PpIX is optimally excited at 405 nm, a wavelength that is subject to strong scattering in tissue as well as strong absorption by blood [73]. If high-resolution (cellular resolution or better) imaging is desired, imaging depths are typically limited to ~100 microns in tissue. However, PpIX exhibits a broad excitation spectrum with a few minor absorption peaks at longer wavelengths, which allows for larger penetration depths at the cost of reduced efficiency of fluorescence generation. A number of fluorescence tomography systems have been designed to operate at near 630 nm and have been shown to successfully detect subsurface PpIX fluorescence at depths of up to a few millimeters in tissue [50, 54, 56], including intact mouse brains [51]. These tomographic systems typically have a limited frame rate due to the long integration time (on the order of a minute) that is necessary to achieve sufficient SNR, in addition to the time-consuming computational process of tomographic reconstruction. A major difference amongst various systems has been the illumination/detection method employed. For example, in 2009, Kepshire and colleagues developed a system that enabled tomographic PpIX imaging through an intact mouse skull, in which the illumination beams were launched at multiple angles using fan-beam scanners, and detection was performed with an array of time-resolved photomultiplier tubes (PMT) [51], a setup that is similar to standard X-ray-based computed tomography (CT). In 2012, Konecky and colleagues developed a fluorescence tomography system based on spatial frequency domain imaging (SFDI) [50], a relatively new technique that uses spatially modulated (i.e. patterned) illumination light to achieve quantitative depth-resolved imaging [74]. This system also utilized multiple wavelengths to correct for changes in tissue optical properties, and to therefore achieve more-accurate quantification of PpIX concentrations. Other model-based methods have also been explored to quantify fluorophores at depth by exploiting the redshift of the emission spectrum due to depth-dependent attenuation of light [53-55, 75]. Based on these models, wide-field imaging systems have been developed with red-light excitation to provide depth-resolved and quantitative measurement of PpIX up to several millimeters deep in turbid media with spatial resolution of about 1 mm [54, 55]. The clinical feasibility of this technique has also been demonstrated recently by Roberts and colleagues in a clinical study of 29 patients (including HGG, LGG, and other brain tumors), in which PpIX fluorescence was successfully detected at depths up to 5 mm, using red-light (620-640 nm) illumination and detection through a 650-nm long-pass filter [56].

1.3.5 Probe-based confocal microscopy

Confocal microscopy is perhaps the most ubiquitous optical-sectioning microscopy technique, in which spatial filters (such as pinholes and slits) are used to reject out-of-focus and multiply scattered background light. Confocal microscopes can generate high image contrast and sub-micron spatial resolution at imaging depths of up to ~100 microns within thick tissues. In terms of *in vivo* imaging, in 2011, Sanai and colleagues reported on the use of a handheld confocal microscope probe to visualize microscopic PpIX expression in LGGs within patients, in which PpIX fluorescence was undetectable with low-magnification WF fluorescence surgical microscopy [11]. It should be noted that the commercial intraoperative confocal microscope (ZEISS Optiscan®) utilized in the pilot study was not optimized for visualizing PpIX fluorescence since an excitation wavelength of 488 nm was utilized instead of a more-optimal wavelength of 405 nm. Furthermore, this device, which was based on a conventional point-scanned single-axis confocal architecture, had a relatively slow frame rate of <1 Hz that was limited by the miniature 2D scanning mechanism used in the device, which made it susceptible to motion artifacts (blurring and image distortion) during handheld use (Figure 1.4a). A number of other intraoperative confocal probes have also been developed based on coherent fiber bundle technology [76, 77] (Figure 1.4b), which eliminate the need to incorporate a complex scanning mechanism in the probe head and thus provides advantages such as high flexibility, small form factors, and high frame rates, at the cost of a reduced spatial resolution and sampling density due to the use of the fiber bundles. A commercial fiber-bundle confocal endomicroscope (i.e. the Cellvizio® system by Mauna Kea

Technologies) has recently received FDA approval for neurosurgical use, with separate devices designed to operate at 488 nm and 800 nm, which are the optimal wavelengths to visualize fluorescein and indocyanine green (ICG), respectively. The major limitation of this technology for visualizing PpIX fluorescence is that the ion-doped fiber bundles in these systems generate significant auto-fluorescence in the 600-700 nm wavelength range when the fibers are used to transmit 405-nm illumination light, which overwhelms the PpIX signal from biological tissues [78]. In addition, the Cellvizio® system does not allow for adjustment of the imaging depth without switching the fiber-bundle probes.

In order to overcome some of the limitations of previous confocal microscopy probes, an alternative confocal architecture has been proposed [79, 80] and continues to be refined for high-speed high-resolution technique for intraoperative visualization of PpIX fluorescence in gliomas. This new confocal design utilizes a line-scan dual-axis confocal (LS-DAC) architecture (Fig. 1.4c) with spatially separated illumination and collection beams to achieve high image contrast – due to more efficient rejection of out-of-focus and multiply scattered light in comparison to conventional single-axis confocal microscope – with the added advantage that chromatic differences between the beams are less problematic since the illumination and collection beams can be independently aligned. The device utilizes a line-by-line scanning mechanism that easily enables a high frame rate of >15 Hz, which minimizes motion artifacts during handheld use and preserves the dynamic information (e.g. blood flow). Technical details about DAC microscopy will be discussed in the next chapter.

Figure 1.4

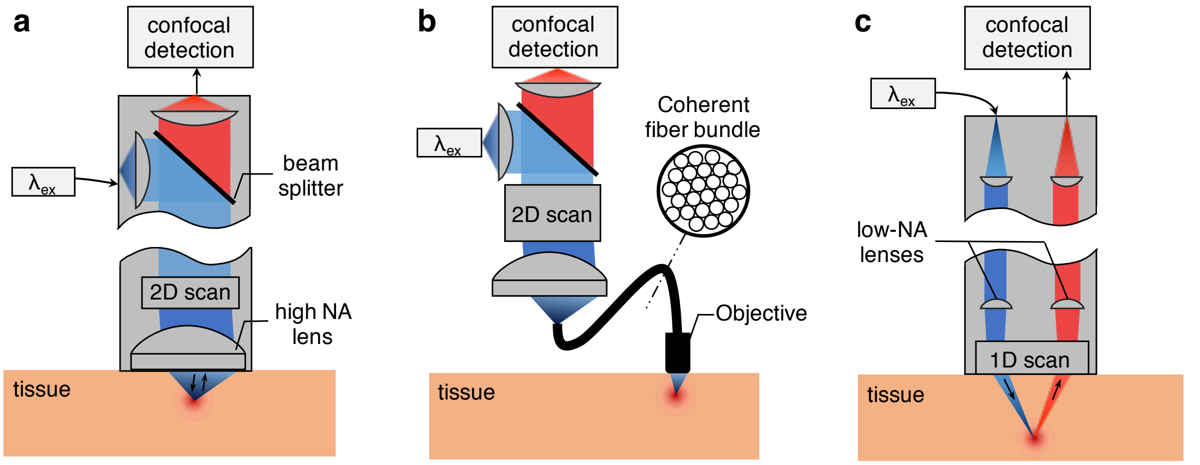

Conventional point-scanned single-axis confocal
(e.g. Zeiss Optiscan/Convivo system)

Fiber-bundle-based point-scanned single-axis confocal
(e.g. MKT Cellvisio system)

Line-scanned dual-axis confocal

Figure 1.4 Comparison of major probe-based confocal systems. (a) The conventional point-scanned single-axis confocal microscope (e.g. the Optiscan®/Convivo® systems) utilizes a high numerical-aperture (NA) scanning objective lens to achieve high-resolution optical-sectioning, but typically has limited frame rates (~1 Hz) due to the use of a miniature 2D scanning mechanism. (b) Coherent fiber bundle based confocal microscopy (e.g. the Cellvizio® system) does not require the incorporation of a complex high-speed 2D scanning mechanism in the probe head and thus provides advantages such as high flexibility, small form factors, and high frame rates (>10 Hz), but at the cost of reduced image quality. (c) Line-scanned dual-axis confocal (LS-DAC) microscopy utilizes spatially separated low-NA line-focused beams and a simple low-speed 1D scanner to achieve video-rate diffraction-limited confocal imaging.

1.3.6 Summary & discussion

Free-standing, non-quantitative WF microscopy remains the most widely used visualization technology for FGS of gliomas, and has been shown to be a clinically safe and simple method to enhance the intraoperative visualization of malignant gliomas compared to conventional methods. However, this method still lacks the sensitivity to effectively guide the resection of tumor in LGGs, or at the infiltrative margins of all gliomas, where tumor burden decreases. As summarized in Figure 1.3, some of the key factors that limit the sensitivity of free-standing WF microscopy are: 1) the “averaging effect” due to low spatial resolution, which reduces the contrast for detecting disseminated and sparse cells; 2) the poor optical detection sensitivity due to the long WD of a free-standing microscope; and 3) the higher background due to out-of-focus and scattered light, in comparison to optical-sectioning techniques that suppress this tissue-induced optical background. Furthermore, it is necessary to maintain a constant working distance and a perpendicular angle between the WF microscope and the tissue to ensure image quality, whereas tumor cavities are often out-of-range or not completely in focus for fluorescence microscopes with fixed working distance. In addition, sidewalls are difficult to visualize because of their steep angle with respect to the illumination source and optics. WF systems that are capable of quantitative and subsurface fluorophore imaging have been developed but are not yet commercially available. A number of WF fluorescence tomography systems have been developed to detect deep-seated tumors below the surgical surface, but have typically improved the imaging depth at the cost of further reducing optical detection sensitivity. Probe-based imaging methods have been developed to mitigate many of the limitations of WF imaging systems, aiming to provide more sensitive and quantitative detection of PpIX fluorescence in gliomas, at the cost of a smaller FOV and increased design complexity. The key trade-offs and the status of clinical translation of these imaging systems have been summarized in Table 1.

Table 1

Technology	Free-standing systems			Probe-based systems			
	Wide-field microscopy	Wide-field spectroscopy	Fluorescence tomography	Wide-field endoscopy	Fiber-optic spectroscopy	Point-scanned confocal	Line-scanned confocal
Field of view	☆☆☆☆	☆☆☆☆	☆☆☆☆	☆☆	☆☆	☆	☆
Spatial resolution	☆☆	☆☆	☆	☆☆☆	☆	☆☆☆☆	☆☆☆☆
Imaging depth	☆	☆	☆☆☆☆	☆	☆☆☆	☆☆	☆☆
Frame rate	☆☆☆☆	☆☆	☆	☆☆☆☆	☆☆☆	☆☆	☆☆☆☆
Sensitivity of PpIX detection	☆	☆☆	☆	☆☆☆	☆☆☆	☆☆☆☆	☆☆☆☆
Direct contact with patients	No	No	No	No	Yes	Yes	Yes
Commercially available	Yes	No	No	Yes	No	Yes	No

Chapter 2: Dual-axis confocal (DAC) microscopy

The microscopic evaluation of slide-mounted surgical and biopsy specimens with tabletop microscopes is currently regarded by the medical community as the "gold standard" for disease diagnosis. However, this core technology for clinical pathology has certain limitations that can lead to poor inter-observer concordance and limited diagnostic accuracy for prognostication and prediction of treatment response. For example, the invasive physical resection of tissues is often not desirable for a patient, especially in cases where the tissues are of functional importance (e.g. brain), cosmetic value (e.g. skin), and in cases where there is a low probability of malignancy (e.g. biopsies of suspicious lesions in the oral cavity). In addition, dynamic information (e.g. blood flow) and physiological parameters (e.g. pH, oxygenation, electrolyte concentration, *etc.*) are often lost or altered during *ex vivo* tissue processing, which reduces diagnostic accuracy. Once tissues are excised, the standard procedure of sample preparation – involving fixation, dehydration, wax embedding, sectioning, mounting of tissue sections on glass slides, and staining – is labor-intensive and time-consuming, potentially resulting in treatment delays. Moreover, the multi-step procedure is known to introduce artifacts (e.g. shrinkage and cracking due to dehydration and/or other process-induced errors) as well as sampling errors since only a small fraction of most tissue specimens are processed onto glass slides for imaging. Therefore, there has been a long-standing interest in developing *in vivo* microscopes for real-time non-invasive microscopic examination of vital tissues. Such *in situ* evaluation circumvents the drawbacks of *ex vivo* tissue processing and provides immediate (and potentially more accurate) feedback to the clinicians, thus accelerating (and improving) the diagnostic and therapeutic processes.

Over the past few decades, various research prototypes and commercialized portable *in vivo* microscopy systems have been developed to address a host of clinical needs [39, 42, 80-105].

Many of these devices have been based on the technology of confocal microscopy [106], which provides cross-sectional images of intact samples (i.e. optical sectioning) with high resolution and contrast (i.e. the signal-to-background ratio, SBR). In confocal microscopy, a spatial filter (e.g. a pinhole or slit) is placed at a conjugate image plane so that only the signal originating from a localized focal volume within the tissue is efficiently transmitted onto a detector, while out-of-focus and multiply scattered photons (from tissue regions away from the focal volume of interest) are largely blocked by the pinhole (or slit). In order for a conventional confocal microscope (referred to as a single-axis confocal, SAC, microscope in this document) to achieve subcellular resolution while retaining adequate FOV and working distance, a bulky high numerical aperture (NA) objective lens and a complex scanning mechanism are typically needed. A portable SAC microscope that images with high resolution and contrast is technically difficult to engineer but has been realized by several academic or industrial groups [81-89, 91, 94-97]. As an alternative to conventional SAC microscopy, DAC microscopy relaxes, to some degree, the requirements for high-NA focusing in order to achieve efficient optical sectioning, and provides certain benefits (as described later in this chapter) for the miniaturization of confocal microscopes down to the scale of several millimeters. In addition, DAC microscopy has demonstrated superior enhancement of contrast and depth (which is useful for tissue imaging) compared to SAC microscopy [79], further improving its clinical value as a non-invasive and real-time alternative to conventional biopsy and histopathology.

2.1 Theory

Dual-axis confocal (DAC) microscopy, which was inspired by the concept of “theta” confocal microscopy [107-109], was developed in the early 2000s to overcome many of the limitations of conventional SAC microscopes for miniaturization and for achieving a long working distance [110, 111]. DAC microscopy achieves optical sectioning using the same basic principle of confocal detection as conventional SAC microscopy, in which a spatial filter is used to reject out-of-focus light. The fundamental difference between SAC and DAC is how the focal volumes are generated and defined. In the SAC configuration, the illumination and detection optics share the same objective (Figure 2.1a), which alone defines the focal volume of the system. However, in a DAC system (Figure 2.1b), the illumination and collection beam paths (blue and green lines, respectively) do not overlap except at their foci. The effective focal volume of a DAC system is therefore defined by the region where the two individual foci intersect (black oval).

The spatially separated illumination and collection path of the DAC architecture provides many advantages. First, in a DAC configuration, the effective axial resolution (i.e. optical sectioning thickness) of the system is proportional to 1/NA, rather than $1/NA^2$ as in a SAC configuration, allowing a DAC system to achieve more effective optical sectioning using low-NA lenses (NA <0.5), which are often lower in cost and more easily miniaturized. Second, the use of low-NA lenses creates a longer working distance such that it is possible to place a scanning mirror between the focusing optics and the sample [112]. This post-objective scanning ensures that the beam always travels on-axis through the focusing optics regardless of the angle of the scanning mirror. Since off-axis aberrations are no longer of concern, simple inexpensive low-NA lenses such as injection-molded aspheres may be used. The use of low-NA lenses is valuable for miniaturization because they allow the objective lenses to be scaled down to a few millimeters while maintaining a reasonable FOV and working distance. Third, the DAC architecture has been shown to improve the imaging contrast (thus imaging depth) in highly scattering fresh tissues, mainly because that the smaller acceptance cone of the low-NA collection lens, and the well-separated illumination and collection beam paths, are better at rejecting the multiply scattered photons [113, 114], which are the main contributors to the background for confocal images of thick tissue. Finally, the illumination and collection beam paths can be independently aligned to compensate for any chromatic effects due to the Stokes shift of fluorophores.

-- **Figure 2.1** --

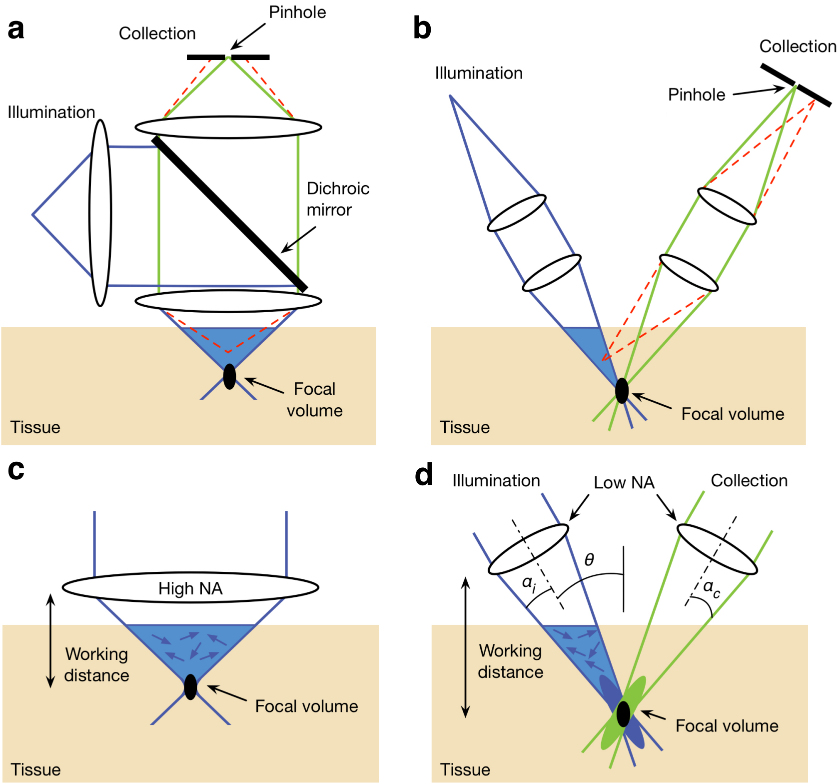

Figure 2.1 Comparison of the optical configurations for a conventional single-axis confocal (SAC) microscope and a dual-axis confocal (DAC) microscope. (a) In SAC microscopy, out-of-focus light (an example beam path is shown with the dashed red lines) is not completely rejected by the pinhole. (b) In DAC microscopy, out-of-focus light is directed away from the pinhole and is more effectively rejected, thereby improving the signal-to-background ratio (i.e. image contrast). (c) In order to achieve a tight focal volume (black oval), a SAC microscope requires a high-NA objective lens. This results in a short working distance that makes miniaturization and beam scanning more difficult. (d) A DAC microscope uses low-NA off-axis illumination and collection

beams, in which the focal volume is defined by the overlapping foci of the two beams. The use of low-NA beams allows for a longer working distance, which provides advantages for miniaturization and beam scanning.

-- **Figure 2.2** --

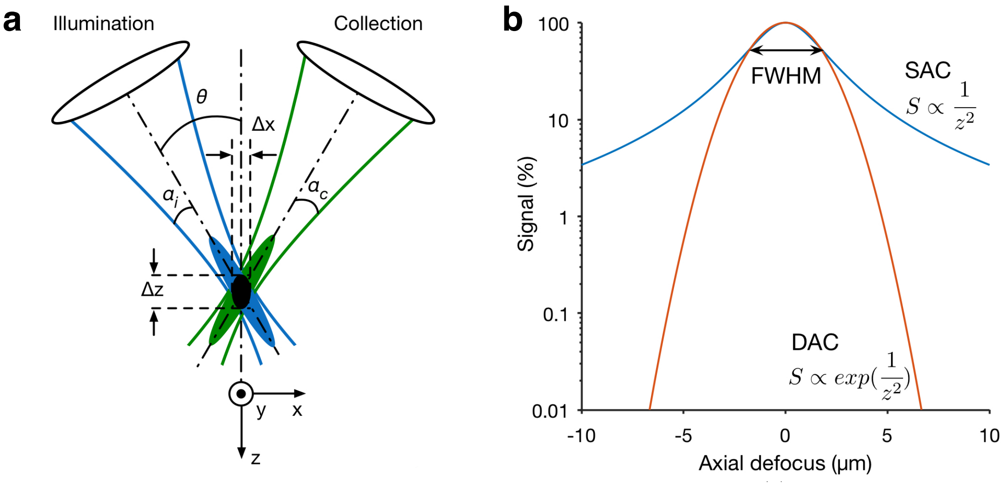

Figure 2.2 The theory of DAC configuration. Two low-NA beams (illumination and collection) with focusing angles of α_i and α_c, respectively, intersect at a half-angle of θ. The focal volume (black oval) of the system is defined by the product of the intersecting point spread functions (PSFs) of the illumination (blue) and collection (green) beams. The dimensions of the focal volume (Δx, Δy, and Δz) correspond to the spatial (lateral and axial) resolutions of the system. (b) The theoretical axial response of a SAC and DAC microscope is shown, in which a point object is translated through the focus of the microscope in the z direction. In this case, the SAC and DAC microscopes have equivalent axial resolutions. The signal rolls off more quickly in a DAC system (red) than in a SAC system (blue), showing that the axial sectioning performance (rejection of out-of-focus light) is superior for the DAC configuration.

The point spread function (PSF) derived from diffraction theory predicts the theoretical response of an imaging system under ideal conditions (i.e. the diffraction-limited performance). In a typical DAC system (Figure 2.2), two low-NA beams with focusing angles of α_i and α_c, respectively, intersect at a half-angle of θ. Using diffraction theory under the paraxial approximation [110, 115], the PSF of each beam can be calculated and is depicted by the blue and green cigar-shaped ovals in Figure 2.2. The overall PSF of the DAC microscope is defined by the product (the black oval) of the intersecting PSFs of the illumination and collection beams. For truncated circular Gaussian beams, the amplitude PSF, U, which describes the spatial distribution of the electric-field amplitude of a beam, is proportional to the Huygens-Fresnel diffraction integral [116]:

$$U \propto \int_0^a W(\rho) J_0(\rho) \rho d\rho \tag{1}$$

where W is the weighting function that accounts for the beam truncation, J_0 is the zero-order Bessel function, and ρ is a normalized spatial variable that describes the distance from the optical axis of the beam (i.e. the beam radius).

The response of the DAC system to a delta-function point object (power received at the detector), I_{DAC}, is proportional to the square of the product of the illumination and the collection amplitude PSFs, U_i and U_c:

$$I_{DAC} \propto |U_i \cdot U_c|^2 \tag{2}$$

The full-width at half-maximum (FWHM) extent of I_{DAC} is often used to quantify the dimensions of the DAC focal volume, and provides an approximation of the spatial resolution of the imaging system. By assuming that the illumination and collection wavelengths are identical ($\lambda_i = \lambda_c = \lambda$), and that the focusing NAs of the illumination and collection beams are also identical ($\alpha_i = \alpha_c = \alpha$), the FWHM spatial resolution along each dimension can be calculated as [12]:

$$\Delta x = \frac{0.297\lambda}{n\alpha \cdot cos\theta}, \Delta y = \frac{0.297\lambda}{n\alpha}, \Delta z = \frac{0.297\lambda}{n\alpha \cdot sin\theta} \tag{3}$$

where n is the refractive index of the medium, and $0 < \theta < \pi/2$. Note that these formulae assume the use of pure Gaussian beams that are not truncated by apertures. For the case of apodized (truncated) beams, a more-detailed treatment may be found in a previous publication [115].

In comparison, the theoretical resolution derived from diffraction theory for a SAC microscope system with uniform illumination are [111, 117-121]:

$$\Delta x = \Delta y = \frac{0.4\lambda}{NA}, \Delta z = \frac{1.4n\lambda}{NA^2} \tag{4}$$

These results indicate that the spatial resolution of a DAC system in the x and z directions (the plane of intersection of the DAC beams) are θ-dependent, and that the axial response, Δz, of a DAC system is inversely proportional to the NA of the lenses, rather than to the square of the NA as with a SAC microscope. This suggests that a DAC system is able to provide effective optical sectioning even when low-NA lenses are used, especially when NA < 0.5, as is the case for DAC microscopy. In addition, as shown in Figure 2.2b, the axial response of a DAC microscope will be steeper compared with a SAC microscope that has an identical FWHM axial resolution.

The PSF and axial response derived from diffraction theory do not account for the effects of scattering, which prevents ballistic photons (i.e. unscattered photons that are "diffraction-limited" in terms of their trajectory and focusing abilities) from penetrating deeply within tissues. Therefore, Monte-Carlo ray tracing models were developed to simulate the performance of various DAC microscope configurations in scattering media [113, 114], including the role of α and θ on sectioning performance (contrast) [114, 122, 123]. The simulation results show that both the imaging contrast (i.e. SBR) and axial resolution consistently improve as θ is increased, suggesting that the crossing angle of the two beams in a DAC system should be maximized when possible. In general, the contrast is more sensitive to the crossing angle whereas the resolution is sensitive to both α (approx. the NA of beams) and θ [122]. Maximizing both parameters typically gives the best performance, but also implies larger device sizes and/or shorter working distances, and potentially creates additional aberrations in the system.

2.2 DAC imaging systems

2.2.1 Basic components

2.2.1.a Geometric orientations

DAC microscope prototypes were initially developed as tabletop systems with primarily off-the-shelf optical components. For example, in several early systems [79, 110, 112, 114, 115, 124, 125], two low-NA (typically around 0.2) objective lenses were oriented at a half crossing angle of 30 deg. Note that the NA and the crossing angle has been varied in different DAC systems, and has often been determined by pragmatic concerns such as working distance and device size, as well as the position and size of the scanning mechanism (e.g. galvanometric or MEMS-based scanning mirrors).

2.2.1.b Post-objective scanning

As discussed previously, the long working distance of low-NA lenses provides room for a scanning mirror to be placed after the focusing optics, making the system less sensitive to the off-axis aberrations that can occur with pre-objective scanning. This scanning scheme allows for large FOVs to be achieved even when small and simple focusing optics are used. Note that the same scanning mirror may be used to steer both the illumination and collection beams simultaneously (scanning the illumination beam while de-scanning the collection beam), which helps to ensure that the beams remain well-aligned and that they always intersect at their foci.

2.2.1.c Hemispherical solid immersion lens

The use of a hemispherical fused-silica solid immersion lens (SIL) has been a distinguishing feature of many previous DAC microscope prototypes. The SIL provides several advantages:

i. Minimizing off-axis aberrations: the curved surface of the hemisphere provides a normal interface to both the illumination and collection beams, so that off-axis aberrations (e.g. coma and astigmatism) are minimized.

ii. Minimizing spherical aberrations: the wave-front curvature of the focused beams is matched to the curved surface of the hemisphere, minimizing spherical aberrations that would result from focusing a beam through a flat interface of two media (e.g. from air to glass). Note that small aberrations will still occur during scanning when the beams deviate from their neutral positions.

iii. Refractive index matching: since the refractive index of fused silica (n = 1.45) is similar to that of most biological tissues, aberrations are minimized as the beams travel across the interface between the tissue sample and the flat surface (distal surface) of the hemisphere.

iv. Increasing the effective focusing NA: if a beam is being focused from air into a higher index material, the NA is typically preserved due to Snell's law (where NA = $n \sin a$). However, the curved surface of the hemisphere, when well-aligned, preserves the ray angles of the focused beams, thus increasing the NA by a factor n. On the other hand, the curved surface of the hemisphere also acts to de-magnify the scanning range of the beams, to first order, by $1/n$. For example, in the case of fused silica (n = 1.45), a 250-

μm axial translation of the stage causes the focal volume to translate ~150 μm within the sample. Similarly, lateral translations are also de-magnified by roughly 1/*n*.

2.2.2. Variations of dual-axis confocal microscopy

Early DAC microscopes utilized point-focused Gaussian illumination in conjunction with point-by-point confocal detection with a raster-scanned [105] or Lissajous-scanned trajectory [42]. While these systems successfully demonstrated the advantages of the DAC architecture, their frame rates were often limited due to the point-scanned method of imaging. In addition to speed, the ability to image deeper was also desired for many *in vivo* imaging applications. To extend the potential of DAC microscopy, a wide range of DAC-variants have been explored. These approaches can be grouped into two main categories based on their aims: 1) improving the imaging speed by modifying either the scanning mechanism (e.g. with complex scanning mirrors [105, 126]) or the illumination patterns (e.g. line scanning [79, 123]); 2) improving the imaging depth (i.e. image contrast) by using different light sources (e.g. near infrared lasers [105, 112], Bessel beams [127]) or through advanced detection methods (e.g. temporal gating, lock-in detection [112, 115, 128]). This section surveys the variants of DAC system that were developed in the recent years.

2.2.2.a Line-scanned dual-axis confocal (LS-DAC) microscopy

In vivo imaging with a handheld device is subject to motion artifacts induced by the subjects and users. For example, early miniaturized point-scanned (PS) DAC systems had a limited frame rate of < 5 Hz, which lead to frequent motion artifacts (blurring and distortions) during *in vivo* use. Although it is possible for a PS-DAC system to acquire images at video rate [105, 118], the FOV is often limited or the scanning mechanisms are complicated, expensive, and difficult to scale down in size. As a result, a simpler line-scanned (LS) DAC microscopy (Figure 2.3) approach has been utilized in recent years to improve the imaging speed, with a trade-off in image contrast due to the loss of confocality along one dimension (along the focal line). In brief, LS-DAC microscopes illuminate a focal line in the sample, instead of a localized point. The focal line is then imaged by the collection optics onto a linear detector. Since an entire line of pixels is imaged and acquired simultaneously, the focal line only needs to be scanned in one direction to generate a 2D image. In addition to reducing the cost and complexity of the scanning mechanism, line-by-line data collection also has the potential to improve the SNR of the images because of the longer effective pixel dwell times.

The first LS-DAC microscope utilized a cylindrical lens in the illumination path to generate a long line-focus along the *y* axis of the imaging plane [79]. On the detection side, instead of using a single mode fiber as in PS-DAC, a digital slit (cropped area-of-interest) was defined within a detector array to serve as a spatial filter for confocal detection. This configuration eliminated the need for a fast 2D scanning mirror to create an image, and high-speed imaging was easily achieved with a slow 1D galvanometric mirror [125, 129]. The frame rate was thus primarily limited by the sensitivity of the detector, rather than the mechanical scanning mechanism. It has been shown that LS-DAC and PS-DAC microscopy exhibit comparable imaging performance at shallow depths (< 150 μm), but that the image quality (especially the contrast) of LS-DAC microscopy deteriorates at deeper depths because of the compromised confocality of a LS system.

Figure 2.3

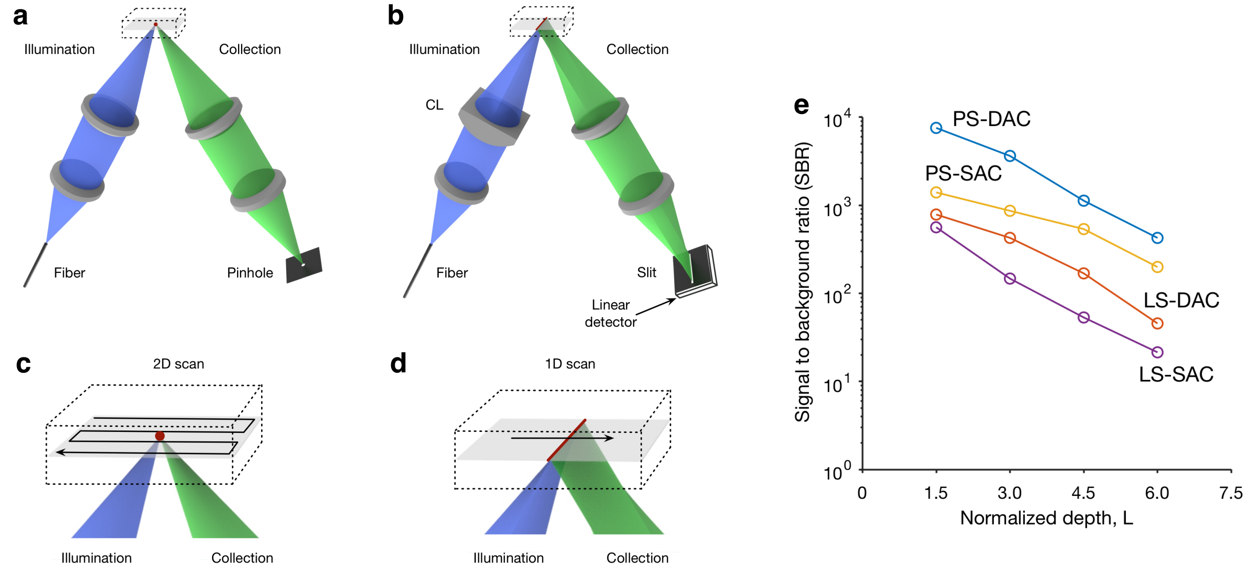

Figure 2.3 (a) In a point-scanned (PS) DAC system, light is tightly focused to a point within the sample, and a pinhole is used for confocal detection. To create an image, the point is scanned in two dimensions (e.g. following a raster- or Lissajous-scanned trajectory) and the image is generated point by point. (b) In the case of a line-scanned (LS) DAC system, the illumination objective lens is replaced with a cylindrical lens (CL) so that light is focused to a thin line within the sample, and a slit is used for confocal detection. The focal line only needs to be scanned in one dimension to create a 2D image. (c-d) Zoomed-in views of the scanning trajectories described in (a) and (b) are shown, respectively. (e) Monte-Carlo scattering simulations to compare the signal-to-background ratio (i.e. image contrast) of various microscope configurations when imaging an in-focus reflective object within highly scattering biological tissues, as a function of depth. The results show that both PS and LS versions of DAC microscopy provide superior image contrast in scattering media when compared with their SAC counterparts. The normalized depth refers to the number of mean free paths that ballistic photons would travel in a round-trip perpendicular path from the tissue surface to the focal volume, i.e. $L = 2\mu_s d$, where μ_s is the scattering coefficient, and d is the imaging depth in the direction normal to the tissue surface.

2.2.2.b Sheet-scanned dual-axis confocal (SS-DAC) microscopy

As discussed in the previous section, one of the drawbacks of LS-DAC microscopy is the deteriorated image contrast due to the loss of confocality along the focal line. Sheet-scanned (SS) DAC microscopy was developed to mitigate the reduced performance in LS-DAC microscopy by utilizing the additional spatial information provided by a 2D detector array [130]. The key principle of this approach is to partially mitigate the loss of confocality by utilizing the useful information contained in the slightly “out-of-focus” regions near the focal line that are typically rejected by a physical slit in a LS confocal microscope. In particular, if the crossing angle of a DAC microscope approaches 90 deg, then the collection arm essentially images a “light sheet” generated by the illumination arm, from which additional information is provided that can be used to perform 3D deconvolution.

The SS-DAC concept was first demonstrated with a scientific complementary metal–oxide–semiconductor (sCMOS) detector array to image an oblique light sheet (effectively, an angled light sheet). By scanning the angled light sheet, a thin 3D volume of data was acquired, which could then be used for deconvolution of the main LS-DAC image given the PSF of the system (either measured or simulated). This simple technique was shown to improve the spatial resolution and contrast of the LS-DAC system [130]. Note that SS-DAC is slightly different from the recently developed light-sheet microscopy (LSM), also known as selective plane illumination microscopy (SPIM) [131, 132]. In a SS-DAC microscope, the illumination beam is focused with a moderate NA to generate a fairly localized focal line, whereas LSM typically utilizes a lower NA to generate a thicker light sheet with a long depth of focus (in order to image a larger 3D volume by scanning the light sheet in only one direction). With LS-DAC and SS-DAC microscopy, the goal is to generate a 2D image by scanning in one direction, rather than a 3D volume of data.

However, with SS-DAC, some 3D information is captured (similar to LSM), but for the purposes of 3D deconvolution to improve one 2D image, rather than to obtain volumetric information. LSM generates more data (in 3D) but sacrifices contrast due to the use of a very low-NA illumination beam (small α) whereas LS-DAC and SS-DAC generate 2D images, but with higher contrast [133]. In general, DAC microscopy is more ideal for imaging highly scattering fresh tissues (including *in vivo*) whereas LSM is ideal for rapid 3D microscopy of relatively transparent model organisms and optically cleared tissues *ex vivo*.

2.2.2.c Modulated-alignment dual-axis (MAD) confocal microscopy

Modulated-alignment dual-axis (MAD) confocal microscopy is a technology that combines the inherent strengths of focal-modulation microscopy [134] and PS-DAC microscopy, with the aim of improving image contrast and depth. In a PS-DAC microscope, illumination and collection beams are spatially separated except at one single point (at the focus of the microscope). Optical sectioning with DAC microscopy relies on the precise alignment of the illumination-beam's focus and detection-beam's focus at the sub-micron level. For example, it has been shown that the confocal signal is reduced by an order of magnitude when the two beams are spatially offset by only one micron (a distance that is equivalent to 1.4 times the beam radius). This feature provides the opportunity to implement a "spatial overlap modulation" technique that was originally used in the context of nonlinear microscopy [135]. The first MAD confocal microscope utilized an acousto-optical deflector (AOD) in the illumination beam path to sinusoidally scan the illumination beam over a small range (+/- a few microns from the well-aligned condition) in the direction perpendicular to the plane defined by the dual-axis beams. This spatial modulation was performed at a frequency f, resulting in a modulated signal at a frequency of $2f$, which could be detected and distinguished from the static (non-modulated) background signal using $2f$ lock-in detection. This strategy was shown to improve the image contrast (SBR) by ~6 dB in scattering media in comparison to standard PS-DAC microscopy. There are a few limitations to the MAD confocal microscopy approach. First, the first order diffracted light used as a spatially modulated illumination source in this system can vary in intensity over time due to the fact that the AOD diffraction efficiency typically varies with scanning angle, which can lead to a modulated background signal that competes with the MAD signal. Second, the acoustic wave within an AOD crystal has a limited propagation speed (~3.63 mm/μs in the early prototypes), which limits the modulation rate and thus the maximum frame rate for MAD imaging. Finally, the MAD technique may be limited in tissues with refractive heterogeneities, which can introduce aberrations and misalignments of the beams that will reduce the modulation depth of the MAD signals.

2.2.2.d Bessel illumination DAC microscopy

Bessel beams have been investigated as a means of improving deep-tissue microscopy in highly scattering and heterogeneous media [136-139]. As discussed in the previous sections, DAC microscopy requires the precise intersection of two beams at their respective foci (micron scale). Therefore, the pointing accuracy of the beams and the quality of their foci are critical for optimal performance. A few recent studies have explored the adaptation of Bessel illumination for DAC microscopy and have shown that Bessel beams exhibit improved pointing accuracy and beam quality in samples with refractive heterogeneities, in comparison to conventional Gaussian beam [127, 139]. Consequently, spatial resolution is maintained more effectively with Bessel-DAC microscopy compared with standard Gaussian-DAC microscopy. One major drawback of Bessel illumination is that the diffraction side lobes contain a significant amount of the beam energy, and contribute to an out-of-focus background that reduces image contrast [127]. Various approaches have been proposed to mitigate this effect for other imaging modalities, such as through the use of two-photon excitation and structured illumination, *etc*. [140-143] Similar strategies are still under investigation for DAC microscopy systems.

2.2.2.e Divided-pupil systems

As an alternative to using two separated objectives as discussed in the previous sections, off-axis illumination and collection has also been achieved using a single high-NA lens with a "divided pupil", i.e. using one half of the lens for illumination and the other half for collection [144-148]. It should also be noted that a few variants of newly developed light-sheet microscopes – for example, oblique plane microscopy [149] and swept confocally aligned planar excitation (SCAPE) microscopy [150] – have also utilized a similar configuration (off-axis illumination and collection sharing one large objective lens) to achieve high-speed volumetric imaging.

2.3 Existing miniature DAC systems

The greatest constraint for the design of *in vivo* microscopes is size. Although the DAC architecture has many unique properties that significantly simplify its miniaturization, smaller form factors are typically associated with reduced performance, as well as increased design complexity and cost. Each clinical device is designed for a specific biomedical application and careful deliberation is necessary to arrive at the most optimal design trade-offs. This section surveys some of the miniature DAC systems that have been built to address clinical applications such as gastrointestinal (GI) endoscopy, dermatopathology, neurosurgery, and the detection of head and neck cancers.

2.3.1 Endoscopic microscopy of hollow organs

There is a clinical need for improved early detection and image-guided biopsy/therapy of diseases in hollow organs such as the GI tract. The most critical requirement for such applications is that the device should be small enough to fit within the instrument channel of a standard GI endoscope, which has a diameter of several millimeters. An endoscope compatible DAC microscope with a diameter of 5.5-mm was developed at Stanford University, and was first tested on human skin *in vivo* at a frame rate of 5 Hz [91]. The device was also deployed through the instrument channel of an endoscope, and was used to image the colonic mucosa of patients after topical application of the FDA-approved fluorophore, indocyanine green (ICG). [151]. Facilitated by the advancement of microelectromechanical systems (MEMS) technology, a number of variants of this DAC endo-microscope have been developed with improved performance for a broad range of clinical applications [83, 96, 126, 152]. For example, a recent publication described a state-of-the art 3D MEMS scanner that can alternate between a "tilting mode" (with actuation along the *x*- and *y*- axes)" and a "piston mode" (with actuation along the *y*- and *z*- axes) to image either in the *en face* plane or the vertical plane in real time [152].

2.3.2 Label-free *in vivo* reflectance microscopy of skin and the oral cavity

Imaging the nuclear morphology and tissue architecture down to the dermal-epidermal junction (~100 μm below the skin surface) is valuable for the diagnosis and treatment of basal cell carcinoma, one of the most common cancers of the skin and oral cavity. As an alternative to invasive biopsy and laborious histopathology, label-free reflectance confocal microscopy can provide a powerful method to allow suspicious lesions to be non-invasively and rapidly examined in real time. These clinical applications require the imaging device to be able to achieve (1) a resolution of 5 µm or less to distinguish nuclear morphology, (2) an imaging depth of at least 100 µm to reach the deeper layers of interest (dermal-epidermal junction), (3) a small imaging head that can fit within the oral cavity, and (4) a high frame rate to reduce motion artifacts during handheld use. The portable divided-pupil line-scanned confocal microscope developed at Memorial Sloan Kettering Cancer Center is an example of label-free *in vivo* confocal microscope of human skin [153]. In this divided-pupil system, the pupil of a high-NA (0.9, water-immersion) objective is divided into two halves, one for the illumination beam and the other for the collection beam. An endoscopic relay lens was incorporated at the distal end so that the oral cavity could be accessed. With such reflectance-based devices, sub-cellular resolution optical sectioning has been achieved at a depth of ~100 µm in human skin, while achieving a frame rate of 8 Hz over a FOV that is comparable to that of a standard 20x objective lens. Note that reflectance confocal microscopy has also been used as a complementary imaging modality to another common reflectance-mode optical imaging technique, optical coherent tomography (OCT), in which reflectance confocal microscopy provides high resolution images at a limited imaging depth while OCT provides lower resolution images at a greater imaging depth [154].

2.3.3 DAC microscopy for fluorescence-guided neurosurgery

As discussion in Chapter 1, surgical resection (i.e. debulking) is the first step in the treatment of many brain tumors including gliomas, in which a greater extent of resection (EOR) has been associated with improved life expectancy and life quality for the patients. However, achieving the optimal EOR of gliomas is challenging because the tumor margins are often indistinguishable from the surrounding normal brain, and there is no quantitative metric (e.g.

tumor-cell density) by which to optimize the EOR for these diffuse tumors that infiltrate far beyond the radiologically defined margins. For many decades, there have been only a small set of untargeted fluorescence contrast agents (e.g. fluorescein, ICG, *etc.*) are approved for clinical use, until the recent FDA-approval of 5-ALA, a metabolic byproduct of the orally ingested agent is used to specifically highlight the bulk tumor regions. However, image contrast is often still ambiguous and weak near the diffuse margins of the tumor. It has been suggested that intraoperative microscopy, which can provide images that approach the gold-standard of histopathology, may have value for neurosurgical oncologists to maximize the EOR while minimizing neurological damage. In particular, portable optical-sectioning microscopes provide sufficient resolution to detect and potentially quantify the sparse and disseminated tumor-cell populations at the margins of diffuse gliomas. Such sparse cell populations are often not visualized by other imaging technologies (e.g. low-power WF microscopes, MRI, CT) since they lack the spatial resolution to detect disseminated cells, even if such isolated cells are effectively labeled by a contrast agent.

A pen-sized handheld DAC microscope with a distal diameter of 1.8 mm was described in 2010, in which images were obtained from the brains of living mice that were genetically engineered to develop medulloblastoma [42]. The device has a cellular resolution (4-µm laterally and 8-µm axially, which are not ideal for histology examination) and an imaging depth of up to 250 µm with the use of low-NA (~0.075) beams focused with a parabolic mirror. A biaxial MEMS scanning mirror was used for post-objective scanning of the focal volume over a FOV of approximately 400 by 400 µm. The MEMS mirror was axially translated with a piezoelectric actuator to adjust the imaging depth by up to 250 µm. In addition, a customized gradient-index (GRIN) “needle lens” located at the distal tip was used, with a diameter of only 1.8 mm. A major limitation of this prototype was its slow frame rate (~4 Hz) due to the point-by-point Lissajous scanning pattern that was used, which made the device vulnerable to motion artifacts.

In 2016, a proof-of-concept miniature LS-DAC design was reported with significantly improved frame rates and spatial resolutions [80]. As discussed in the previous section, the LS-DAC architecture significantly simplifies the requirements of the scanning mechanism for high-speed imaging. A robust commercial MEMS mirror was used to scan the focal line in one dimension to create *en face* images at video rate (>16 Hz). The improved resolution was achieved by using a custom developed 1:3 de-magnifying relay objective at the distal end of the device. The relay lens effectively increased the NA of the beams as well as the crossing angles, at the cost of reducing the FOV. The system was able to achieve a lateral resolution of 1.1 μm with 2.0-μm axial resolution (optical sectioning thickness) at a FOV of around 350 μm by 350 μm. A trade-off for using line scanning in miniature devices is that confocal detection must be achieved with a digital line detector that is directly integrated mounted within the device, instead of using a fiber-coupled point detector (in the case of a miniature PS-DAC microscope). The preliminary design in 2016 was not portable nor capable of real-time image visualization, in additional to a number of technical limitations (such as significant field curvatures, lack of lens cap for imaging depth control, etc.) that were not ideal for tissue imaging. In Chapter 4, a fully packaged handheld LS-DAC system that is feasible for clinical applications will be described in details.

2.4 Summary

This chapter surveys the technology of DAC microscopy, an optical imaging modality that utilizes low-NA lenses to achieve effective optical sectioning and superior image contrast in biological tissues. In contrast to the conventional confocal microscope invented by Minsky in 1957

[106], a DAC microscope utilizes spatially separated off-axis illumination and collection beam paths that only intersect at their foci – an optical architecture inspired by the initial works of Stelzer *et al.* [107, 109], and Webb *et al.* [111] in the 1990s – to improve image depth and to reduce the complexity of miniaturization. Several portable DAC systems have been developed for a wide range of clinical applications such as intraoperative guidance and pre-cancerous region screening, and a successful prototype of the miniature LS-DAC microscope that provides high-speed high-quality imaging, is continue to be refined as a handheld clinical device for the emerging field of fluorescence-guided neurosurgery.

Chapter 3: Quantitative PpIX imaging with LS-DAC microscopy: a feasibility study

3.1 Background

Wide-field fluorescence microscopy of macroscopic PpIX fluorescence has become the standard-of-care for guiding the resection of HGGs in Europe, and has also been approved by the FDA in 2017 for clinical use in the USA. While this visualization method (i.e. standard surgical microscope) is simple and is effective in detecting strong fluorescence from HGG, it is less effective for detecting PpIX fluorescence in LGG and for identifying the infiltrative margins of all gliomas. Although it has been shown that high-resolution microscopy can visualize PpIX fluorescence in regions where standard WF microscopy failed, the biological insights of the microscopic PpIX expression remains poorly understood [36]. There is a growing interest in correlating the patterns of PpIX expression to known tumor biomarkers such as IDH1m (overexpressed in >80% of LGGs), Ki-67 (proliferative marker), and pHH3 (mitotic index), *etc.* If a biological correlation can be established, it will facilitate the clinical acceptance of this method. This chapter describes a pilot study that aims to address three major objectives: 1) assessing the feasibility of using LS-DAC microscopy, a high-speed high-resolution optical-sectioning imaging technique, for microscopic PpIX quantification in human biopsy; 2) performing a clinical study over a course of 15-months to show that LS-DAC results agree with conventional slide-based histology results; 3) providing a set of tools (e.g. image phantoms, potential quantification metrics, *etc.*) for accurate and reproducible PpIX quantification at the microscopic level, which is currently a void in this nascent field.

3.2 Methods

3.2.1 Tabletop LS-DAC microscope

The microscope system used in this study is a modified version of the tabletop LS-DAC microscope system described previously [79, 129]. In brief, as shown in Figure 3.1, a single-mode fiber-coupled 405-nm diode laser (OBIS-405, Coherent Inc., Santa Clara, CA) is collimated and focused into the sample with unity magnification (NA ~ 0.12). A plano-convex cylindrical lens (*f* = 50 mm, Optosigma, Santa Ana, CA) is inserted in the collimated region of the illumination path to intentionally create a large degree of astigmatism, resulting in a focal line that is 500-µm long and 1.4-µm wide (FWHM). A single-axis galvanometric scanning mirror (6210H, Cambridge Technology, Bedford, MA) scans the focal line laterally (along the *x*-axis), to create an image that is parallel to the tissue surface (*en face*). The sample rests on a custom hemispherical solid immersion lens (SIL, n = 1.45) that is mounted on a linear translation stage. As described in Chapter 2, the hemispherical SIL performs index matching of the illumination and collection beams as they obliquely propagate from air into the sample. The SIL also acts as a lens that increases the effective NA of the illumination beam from 0.12 to 0.17 (a factor of n). Fluorescence photons generated at the focal line of the illumination beam are imaged by the collection optics, which are oriented off-axis at a half-crossing angle of 30 degrees with respect to the illumination axis. The collection optics images the focal line onto a scientific complementary metal-oxide-semiconductor (sCMOS) detector (Hamamatsu ORCA Flash 4.0 v2) with 5x magnification via a pair of lenses (f_{L1} = 20 mm; f_{L2} = 100 mm). A 600-nm long-pass fluorescence filter (Semrock BLP01-594R-25) is placed in the beam path to filter out the excitation photons (405 nm). Raw images were collected via a camera link frame grabber (Firebird 1xCLD, Active Silicon, UK) at 1000 raw exposures per second (1 ms per exposure). A custom LabVIEW (National Instruments, Austin, TX) program was used to crop out and bin the central three lines of each camera frame (corresponding to the image of the focal line) to create a digital confocal slit (19.5 µm in width, corresponding to approximately 2.7 µm in tissue). These lines were stitched serially in the *x* direction into *en face* images in real time at a 2D imaging rate of 2 Hz. It should be noted that the LS-DAC microscope is capable of acquiring images at video rates, but for the purposes of this study, which aimed to develop a standardizable phantom and quantitative imaging methods, a lower frame rate was utilized to maximize SNR and to demonstrate the feasibility of our methods. Volumetric data was collected by translating the sample holder along the *z* axis with a motorized linear actuator (TRA12CC, Newport Cooperation, Irvine, CA).

-- **Figure 3.1** --

Figure 3.1 Schematic of the LS-DAC microscope. A cylindrical lens “C” is inserted in the collimated region of the illumination path to transform a point focus into a line focus. The focal line is scanned by the scan mirror in the *x* direction to create a 2D *en face* image of the sample (in the *x*-*y* plane). The hemispherical solid immersion lens (SIL) acts as a sample holder that is translated along the axial (*z*) direction by a motorized stage (not shown) to enable volumetric imaging. The inset (red dashed box) shows a zoomed-in view of the LS-DAC microscope near the sample.

-- **Figure 3.2** --

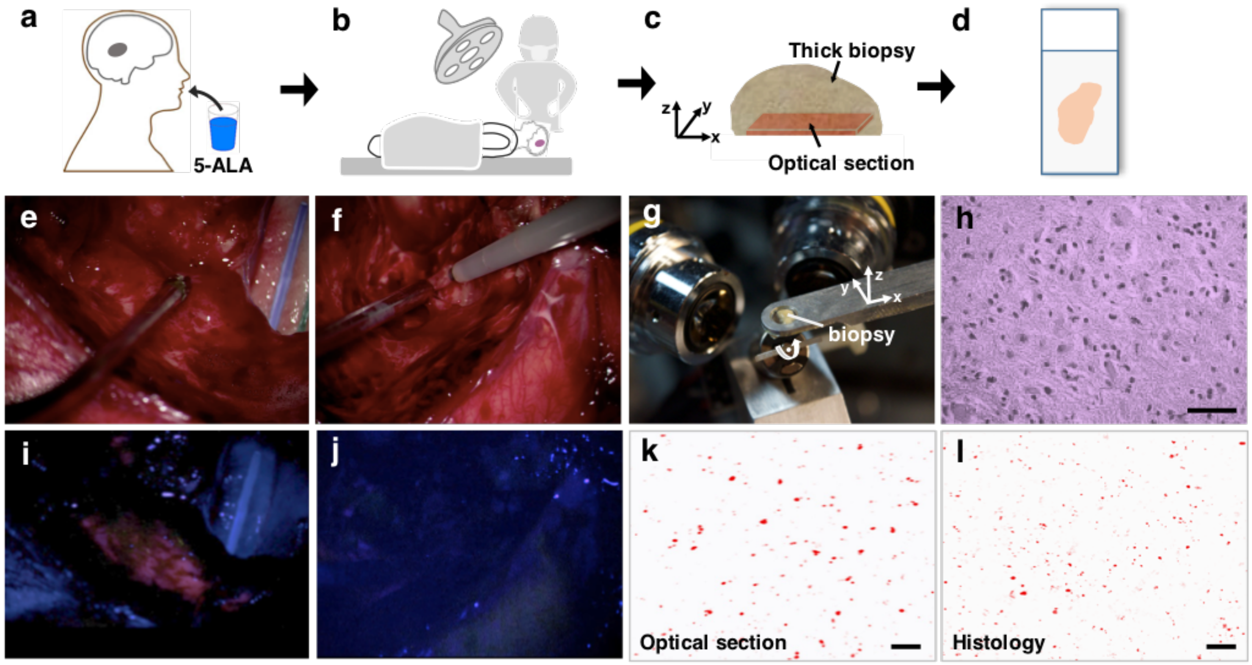

Figure 3.2 Workflow of the study with example images. (a)(b) Glioma patients were orally administered with 5-ALA prior to the surgery. (c) A brain biopsy was then imaged with a tabletop LS-DAC microscope to obtain images of PpIX expression with sub-cellular resolution. (d) Corresponding images from histology slides (both H&E staining and PpIX fluorescence) were obtained to validate the optical-sectioning results. (e)(f) Example of WF intraoperative images from a HGG and a LGG case, respectively, showing that the tumor resembles the surrounding normal tissues under white light imaging in both cases. (g) Photograph of a biopsy specimen placed on the sample holder of a tabletop LS-DAC microscope. (h) Image of a H&E-stained histology section at 40x, as a confirmation of the presence of glioma cells in the biopsy specimen. (i)(j) Intraoperative WF images of macroscopic PpIX fluorescence (pink color) from the regions shown in panels (e) and (f), showing that WF surgical fluorescence microscopy was capable of detecting PpIX fluorescence from the HGG but not from the LGG. (k) Example LS-DAC image of the biopsy, showing subcellular PpIX expression. (l) PpIX fluorescence histology image of the same biopsy imaged in (k), showing a similar pattern of microscopic PpIX expression. All scale bars represent 50 μm.

-- **Figure 3.3** --

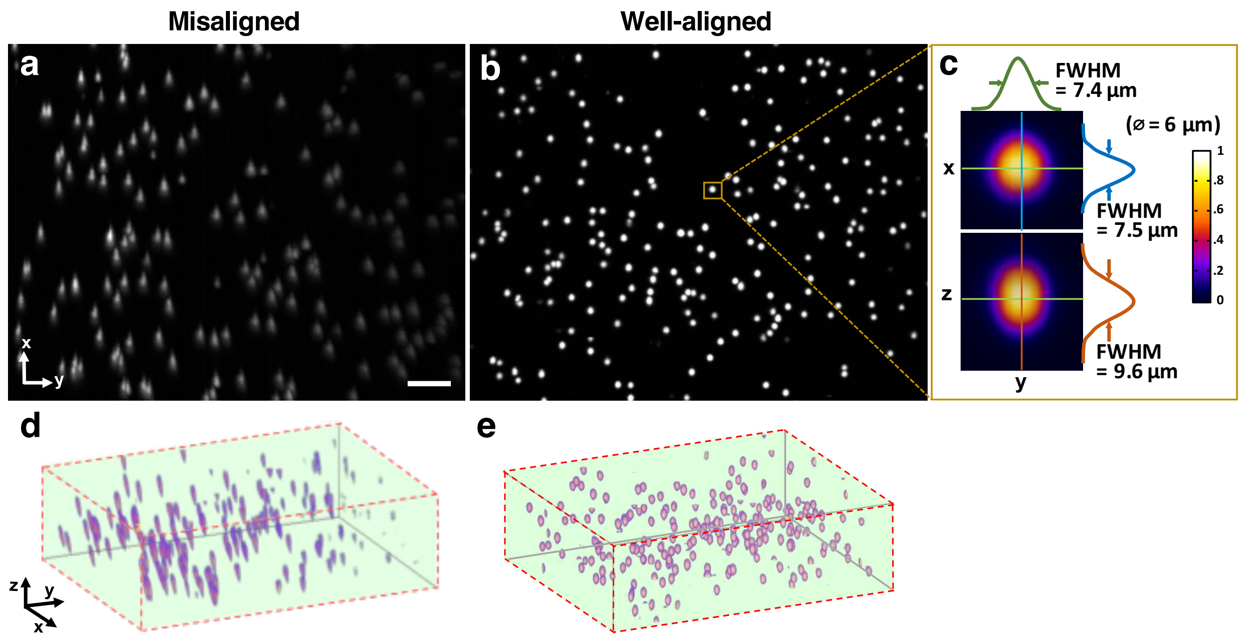

Figure 3.3 (a) A maximum-intensity depth projection (along the *z* axis) of a volumetric image of the alignment phantom is shown for a misaligned LS-DAC microscope. (b) A maximum intensity projection of a volumetric image of the phantom is shown from a well-aligned system, in which the intensity of the fluorescent beads is uniform across the FOV with <15% deviation (center to edge), and all beads are well-resolved across the entire FOV of 350 µm (*x*) by 520 µm (*y*) by 150 µm (*z*). (c) Example cross-sectional views of one bead. The FWHM dimensions of the microsphere allow for the assessment of the spatial resolution of the system. (d)(e) Alpha-blending volume renderings of (a) and (b), respectively, illustrate the uniformity of the detected fluorescence signal from the beads as well as the uniformity of the spatial resolution across the entire FOV. The scale bar represents 50 µm.

3.2.2 System standardization with an agarose-based fluorescent bead phantom

3.2.2.a Phantom preparation

The standardization phantom consisted of fluorescent microspheres (Fluoresbrite® polychromatic red #19111-2, Polysciences Inc. Warrington, PA) embedded in an agarose gel. The polystyrene-based fluorescent microspheres are "NIST-traceable" size standards, and are designed to be optimally excited at a wavelength of near 525 nm, with an emission peak at 565 nm. In this study, the beads are purposely excited with low efficiency at 405 nm and only the tail of the fluorescence spectrum is collected with a 600-nm long-pass filter. While this causes the detected fluorescence signal to be relatively weak (compared with the fluorescence signal from the beads at their optimal excitation/emission wavelengths), this weaker signal approximates the strength of the PpIX fluorescence seen in glioma tissues from patients who have been administered 5-ALA, and allows the alignment and performance of the microscope to be assessed under realistic conditions (*in situ* fluorescence signal levels). The stock concentration of microspheres (2.5% aqueous suspension) was diluted 40 times in a 0.8% agarose solution (Sigma Aldrich® A9539) at 70 °C, and the mixture was allowed to solidify while cooling to room temperature.

3.2.2.b Phantom-assisted alignment

Because PpIX has an unusually large Stoke's shift (λ_{ex} = 405 nm; λ_{em} = 625 nm), the proper alignment of the illumination and collection beam paths of the DAC microscope (or any alternative microscope technology) must account for the chromatic differences between these disparate wavelengths. The fluorescent bead phantom developed in this study is used to provide a high-resolution target (the beads are 6-µm in diameter with <1% variation) that may be used to optimize the alignment of the microscope at an illumination and collection wavelength of 405 nm and >600 nm, respectively. Volumetric imaging data of the phantom is collected to verify that both the sensitivity (i.e. the SNR) and the 3D spatial resolutions (FWHM dimensions of the beads) are uniform across the FOV, confirming satisfactory alignment of the dual-axis beams with respect to each other (for high resolution) and with respect to the hemispherical SIL (for uniform resolution across the FOV). For clinical use, a method to verify that the performance of an optical-sectioning microscope is reproducible is to measure the SNR and spatial resolution of the microscope in a volumetric phantom. Here, the SNR is calculated as:

$$\mathrm{SNR} = \frac{S-B}{\sigma_B}, \tag{1}$$

where S is the mean of the peak pixel intensity of all beads in an image; B is the mean pixel intensity of the background, and σ_B is the standard deviation of the background signal. Note that the standard deviation of the peak signal from each bead cannot be reliably measured due to the small size of the beads and their spherical geometry, with only a single pixel corresponding to the peak of each bead.

3.2.3 *Ex vivo* imaging of PpIX-expressing human brain tissues

3.2.3.a Tissue preparation

Glioma tissue samples (n = 14) were collected from consenting patients at the Barrow Neurological Institute (BNI, Phoenix, AZ) in accordance with an approved protocol (IRB #10BN159). Patients were orally administered with 5-ALA at a concentration of 20 mg/kg three hours prior to surgery, and brain biopsies obtained during surgery were fixed in 3% paraformaldehyde for 24 hours, and then stored in 1x phosphate-buffered saline (PBS) at 4 °C before being imaged with a tabletop LS-DAC microscope. All tissue specimens were obtained from MRI-enhancing regions corresponding to the bulk tumor. After the LS-DAC images were taken, the imaged tissue surfaces were physically sectioned (10-µm in thickness) in the *en face* direction (as close and parallel to the tissue surface as possible), and mounted on standard microscope slides. Histology slides were imaged with a conventional epifluorescence microscope (Leica DM-IRB® inverted system) to visualize intracellular PpIX expression. In addition, adjacent sections were stained with hematoxylin and eosin (H&E), and imaged with a standard bright-field pathology microscope.

-- **Figure 3.4** --

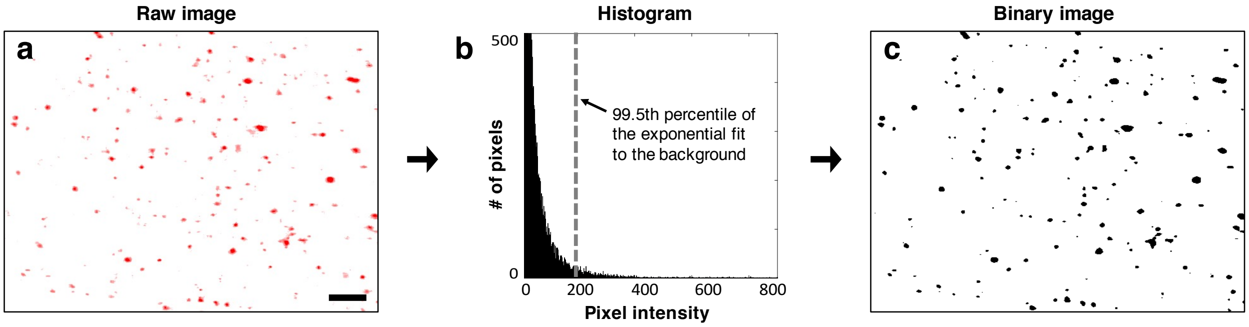

Figure 3.4 The same quantification algorithm was used for both LS-DAC images and histology images. (a) Example image of PpIX-expressing glioma tissue obtained with the LS-DAC microscope. The scale bar represents 50 µm. (b) Histogram of the raw image, in which the intensity distribution of the background is approximated as an exponential decay. The dotted line denotes the threshold for segmentation, in which pixels with intensities above this threshold are considered "positive" for PpIX expression. (c) A binary image of (a) obtained after segmentation, utilizing a 99.5th percentile threshold to the exponential fit.

3.2.3.b Image acquisition and quantification

For LS-DAC microscopy, volumetric imaging data was collected at three random region-of-interests (ROIs) of each tissue specimen. The FOV of the image datasets was 350 µm (*x*) by 520 µm (*y*) by 150 µm (*z*, depth), and the sampling pitch in these three dimensions was 0.79 µm, 0.88 μm, and 0.69 μm, respectively. From each volumetric dataset, 10-μm-thick average-intensity projections (i.e. "optical sections") were visualized to simulate images of 10-μm-thick slide-mounted histology sections. For the quantitative comparison study of LS-DAC microscopy vs. fluorescence histology, three ROIs (350 μm by 520 μm each) were randomly selected for correlative analysis. Identical microscope settings were used for the imaging of all histology slides. In this study, we attempted to quantify the density of the expression of punctate and localized spots of PpIX that appear in glioma tissues [155, 156]. The density of PpIX expression was quantified using an identical algorithm for both the LS-DAC microscopy and fluorescence histology images. This algorithm identifies and quantifies the density of localized spots of PpIX that are brighter than the tissue background (mostly autofluorescence), in which the background is assumed (and observed) to be relatively uniform. The quantification algorithm was implemented via a custom MATLAB script:

i. Based on the intensity histogram of each image, an exponential curve fit was performed on the low-intensity background distribution, and a threshold was defined that corresponded to the 99.5th percentile of the background distribution (area under the curve).

ii. Once the threshold was identified, a binary image was created by setting all pixels above the threshold as positive (black in Figure 3.4c) and everything else as negative (white in Figure 3.4c).

iii. A "PpIX-positive spot" was defined as a group of adjacent positive pixels that exhibit a "8-connected" pattern according to a widely used connected-component labeling algorithm [157] (i.e. any two positive pixels that share an edge or a vertex will be classified into the same "PpIX-positive" feature). The PpIX density is then defined as the total number of "PpIX-positive spots" per mm^2 (note that each image has a FOV of 350 µm x 520 µm).

3.3 Results

A total of 14 high- and low-grade glioma samples were imaged during a 15-month period. To ensure the identical performance of the imaging system on different days, the SNR of detection was quantified from images of the fluorescent phantom. In addition, the spatial resolution of the system (in all three dimensions), and the uniformity of performance across the FOV were also assessed to confirm the proper alignment of the LS-DAC system. With the system settings fixed, the following parameters could be attained in multiple experiments over the entire course of the study (15 months): the SNR of detection was 30.05 dB ± 3%; the average measured dimensions (FWHM) of the fluorescent beads (Ø = 6 µm) were 7.5 µm ± 0.2 µm in the lateral directions, and 9.6 µm ± 0.5 µm in the axial direction (enlarged due to diffraction and minor aberrations). No noticeable fluorescence degradation was observed in the microspheres within a shelf life of 12 months. Using the aforementioned quantification, PpIX density from LS-DAC images shows a strong linear correlation with that from standard fluorescent histology images, with a determination coefficient (R^2 value) of 0.958 (Figure 3.5).

--- **Figure 3.5** ---

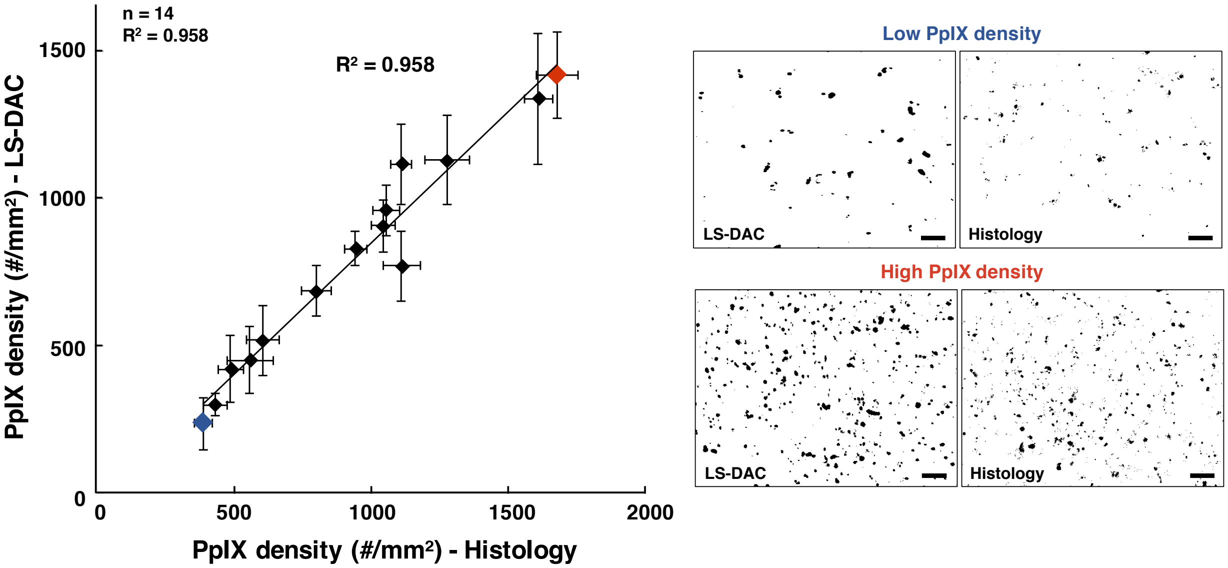

Figure 3.5 Quantitative comparison of LS-DAC microscopy images vs. corresponding fluorescence histology images in terms of PpIX density. Each point on the scatter plot represents the average PpIX density from three random ROIs within each biopsy sample, with the error bars indicating the standard deviation from the measurements. Example binary images of lowest PpIX density (blue dot) and highest PpIX density (red dot) are shown on the right. Note that a volumetric dataset was collected at each tissue location but only a 10-µm optical section at the surface was quantified to simulate a 10-µm slide-mounted histology section. The scale bars represent 50 µm.

3.4 Conclusion and discussion

This study developed a set of tools to enhance the clinical translation of optical-sectioning microscopes for real-time pathology and quantitative surgical guidance of glioma resections. First, a standardization method based on a fluorescent bead phantom was developed. This custom phantom is highly reproducible, stable, simple to prepare, and provides uniform microscopic structures that mimic the sparse and weak fluorescence from 5-ALA-induced PpIX generated by subcellular organelles within glioma tissues. As shown in Figure 3.3, this phantom is a valuable tool to ensure the proper alignment of an optical-sectioning microscope, enabling quantitative characterization of the sensitivity, resolution, and uniformity of the imaging system. As a result, it is possible to obtain reproducible quantitative images of PpIX-expressing brain tissues, which will be necessary to standardize the performance of clinical devices in single-site clinical studies over time, and/or in multi-site clinical studies. This standardization method is applicable to a variety of optical-sectioning microscopy technologies for intraoperative guidance of glioma resections based on PpIX fluorescence. Second, we showed that quantitative PpIX images obtained with LS-DAC microscopy correlate positively with fluorescence histology, suggesting that LS-DAC microscopy can potentially serve as a minimally invasive and real-time alternative to conventional biopsy and histopathology.

In this study, the density of localized spots of sub-cellular PpIX expression was chosen as a quantitative metric of interest because it is a potential surrogate measure of tumor burden. We show that PpIX density is an objective quantity that can be extracted from both DAC microscopy and histology images, with excellent correlation between these two techniques. Importantly, we note that PpIX density alone may not be an accurate indicator of tumor burden. For example, as shown in Figure 3.6, although PpIX density is high, the intensity of the PpIX fluorescence may be low, and/or the size of the PpIX-expressing spots may be smaller than in other specimens with lower PpIX density. This observation suggests that the intensity and sizes of the signal should also be taken into account when developing a surrogate measure of tumor burden or proliferative index. The observations are consistent with our biological understanding of PpIX generation, as the volumetric production of PpIX granular inclusion bodies in brain tumor cells can vary from cell to cell. Ultimately, the clinical significance of these different metrics, for the purposes of achieving GTR for glioma patients, must be validated through outcomes-based clinical studies. Towards this aim, a handheld version of the LS-DAC microscope is currently under development. This pilot clinical study is of value for the clinical translation of handheld intraoperative fluorescence microscopes to guide the resection of gliomas and to improve outcomes for glioma patients.

-- **Figure 3.6** --

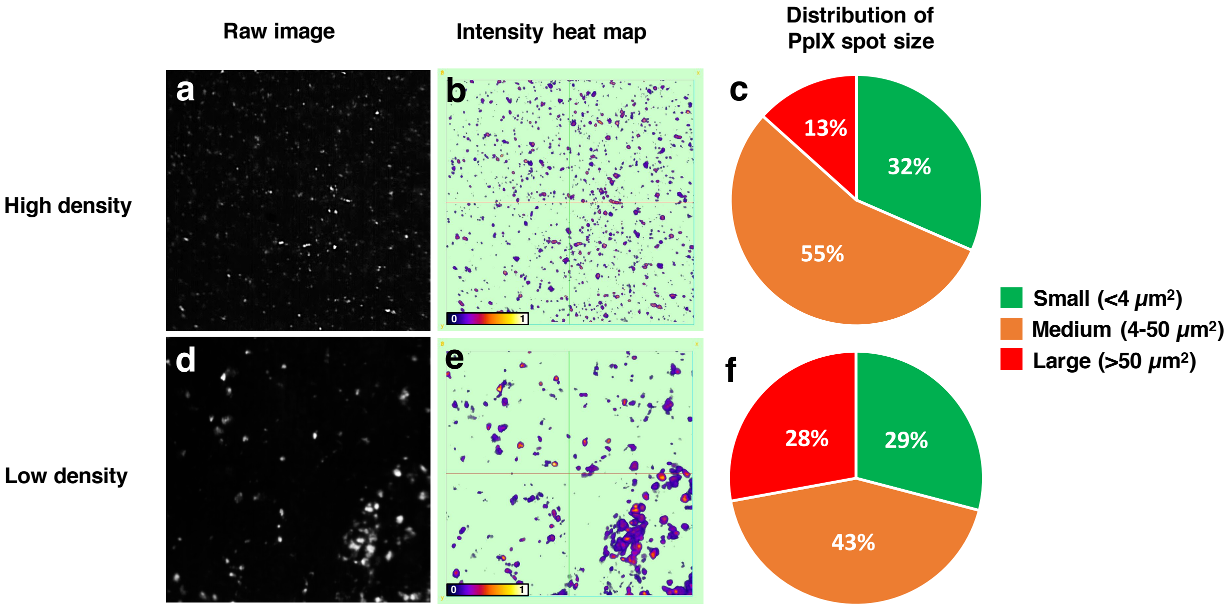

Figure 3.6 An example showing that PpIX density alone may not be an accurate indicator of tumor burden. (a-c) A sample with high PpIX density shows a lower fluorescent intensity as well as smaller fluorescent spot size, when compared with another sample with low PpIX density that is imaged with identical system settings. The biological insight of the microscopic expression of PpIX fluorescence is still poorly understood, but this observation suggests that the intensity and sizes of the signal should also be taken into account when developing a surrogate measure of tumor burden or proliferative index.

Chapter 4: Handheld LS-DAC microscope for fluorescence-guided neurosurgery

4.1 Background

The microscopic evaluation of slide-mounted tissue specimens on tabletop microscopes remains the “gold standard” for the diagnosis of diseases in clinical practice. However, this method of histopathology is invasive, time-consuming, and introduces imaging artifacts. There is a growing interest in developing portable systems for real-time non-invasive microscopic examination of tissues *in vivo* [42, 80, 83-85, 89-92, 94, 98, 99, 101, 103, 104, 158]. Many of these devices have been based on scanning confocal microscopy, an optical imaging technique that provides high-resolution cross-sectional images of intact specimens. Conventional confocal microscope systems utilize point-focused illumination and a pinhole at the detector to reject out-of-focus and multiply scattered background light. With point detection, a 2D scanning mechanism is required to create a 2D image. However, high speed (kHz range) 2D scanning mechanisms are typically complex and technically challenging to miniaturize, and many portable point-scanned (PS) confocal systems have limited frame rates, which leads to motion artifacts during handheld use. Although confocal endoscopes based on coherent fiber bundle technologies can achieve relatively higher frame rates (by scanning the laser focus at the proximal end of the fiber bundle), their spatial resolution is typically inferior to that of non-fiber-bundle-based devices.

Dual-axis confocal (DAC) microscopy is an alternative confocal architecture that utilizes spatially separated low-numerical-aperture (NA) beams to achieve effective optical sectioning and superior image contrast in biological tissues [110, 115]. Recently, line-scanned versions of DAC microscopy (LS-DAC) have been shown to enable video-rate imaging with simple low-speed scanners (20-30 Hz), while maintaining comparable image quality to their PS counterparts at depths of up to ~150 μm in tissue [79, 123, 129]. A proof-of-concept miniature LS-DAC design that incorporated a commercial MEMS-based scanning mirror to achieve video-rate confocal imaging was previously reported in 2016 [80]. However, the previous system utilized a bulky and expensive tabletop sCMOS (scientific complementary metal oxide semiconductor) camera that was mounted on a precision alignment stage rather than being fully integrated into a portable package. Second, the preliminary image acquisition hardware and software were not capable of providing image visualization in real time. In addition, the scanned imaging field of the proof-of-concept system was curved (rather than a flat 2D plane, as in an ideal scenario) due to the geometry of the scanning mechanism, which can result in misleading images especially of thin layered structures and is thus not ideal for tissue imaging.

This chapter describes the most recent development of a fully packaged handheld LS-DAC system that has properly addressed the limitations in the previous system and is feasible for clinical use. The new system utilizes a compact and inexpensive line detector to provide high-speed fluorescence imaging at 16 Hz with sub-nuclear resolution in tissue. Compared to our previous prototype, resolution and contrast have been improved, as described in the following paragraph. In addition, to enable flat-field imaging, the device also incorporates a novel scanning mechanism in which the MEMS mirror is simultaneously tilted (to scan a 2D image) and pistoned (to compensate for field curvature). Examples of *en face* imaging of layered structures (with and without field curvature), as well as image mosaicking, which is enabled by the flat-field correction, are also provided. Finally, the entire system (including the PC and monitor) has been designed to fit into a standard surgical cart, and is controlled through a user-friendly software interface for real-time imaging by clinicians.

4.2 Packaging of handheld LS-DAC system

-- **Figure 4.1** --

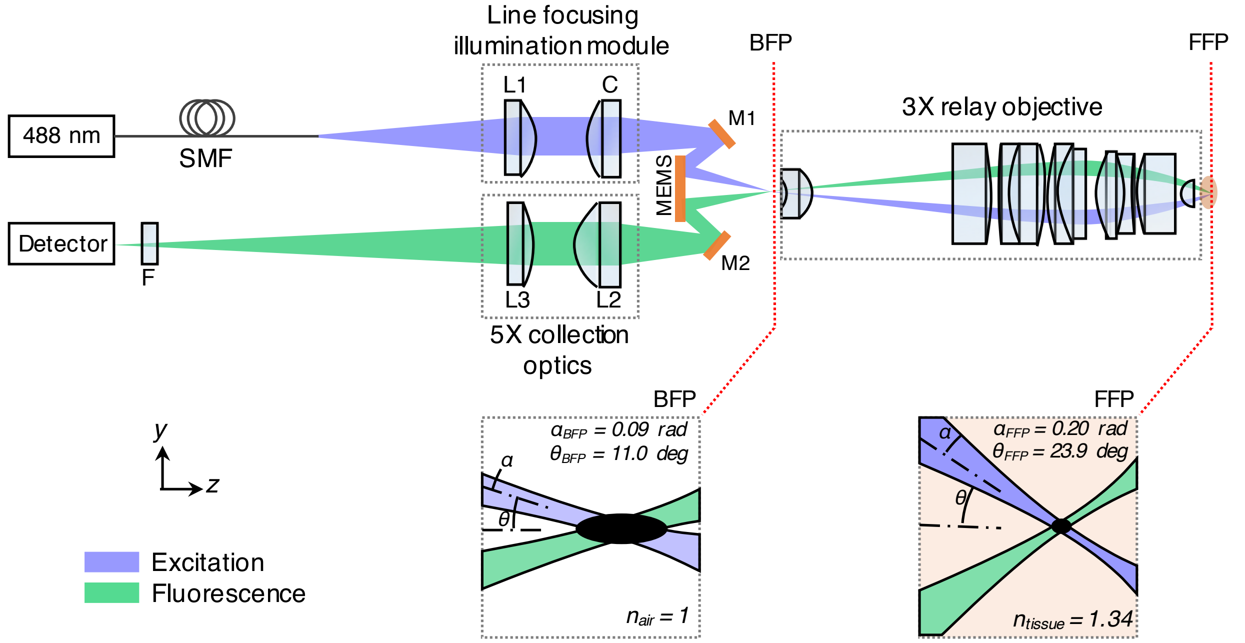

Figure 4.1 Optical circuit of the handheld LS-DAC microscope. A custom line-focusing fiber module shapes the illumination beam into a focal line at the back focal plane (BFP) of a custom relay objective. A MEMS mirror scans the focal line in one dimension to create an *en face* 2D image. The objective provides 3x magnification, which boosts the focusing NAs ($\sim\alpha$) and the half-crossing angles (θ) of the beams from the BFP to the front focal plane (FFP). L1, L2, and L3 are simple low-NA spherical doublets. C is a low-NA cylindrical doublet. M1 and M2 are alignment mirrors. F is a fluorescence filter.

The optical design (Figure 4.1) of the LS-DAC device is an optimized version of the aforementioned prototype. In the current system, the illumination beam from a 488-nm diode laser

(LuxX 488-100, Omicron-Laserage GmbH, Rodgau, Germany) is coupled into a custom illumination fiber module (Ø = 3.2 mm, assembled by Grintech GmbH, Jena, Germany) via a single-mode fiber. The illumination module consists of two low-NA doublets (L1, spherical lens, $f = 9.0$ mm; C, cylindrical lens, $f = 12.0$ mm), which shape the illumination beam into a line focus with a FWHM length of 1.2-mm and a focusing NA of approximately 0.09. This illumination module exhibits improved diffraction-limited focusing with less diffraction side lobes (apodization) compared with our previous system due to the use of a simpler optical layout (two lenses instead of three) and improved fabrication methods (elimination of interior retaining rings that resulted in beam clipping in the previous illumination module). On the collection side, a pair of low-NA spherical doublets (L2, $f = 12.0$ mm, and L3, $f = 60.0$ mm) are used to image the focal line with 5x magnification from the back focal plane (BFP) onto the detector array. A 495-nm long-pass filter (AT495lp, Chroma Technology Corp, Bellows Falls, VT) can be inserted along the collection beam path via a quick-release adaptor (QRC05A, Thorlabs Inc., Newton, NJ) to reject back-scattered illumination light. A pair of angled mirrors (fabricated by Tower Optical Inc, Boynton Beach, FL) with rotational and translational (axial) adjustability are used to ensure the precise alignment of the illumination and collection foci, at a half-crossing angle of 11.0 deg at the BFP of the device. A commercial MEMS scanning mirror (Mirrorcle Technologies Inc., Richmond, CA), with three degrees of freedom (tip, tilt, and piston) is used to scan the focal line for *en face* imaging at 16 Hz, as well as to correct the aforementioned scanning-induced field curvature (described in the next section). All spherical lenses (L1, L2, and L3) were purchased from Edmunds Optics (Barrington, NJ, catalog # 45090, 63692, and 45345, respectively), and were then reduced in diameter by BMV Optical Technologies, Inc (Ottawa, Canada). The cylindrical lens, C, was fabricated by BMV based on the design of a spherical doublet from Edmund Optics (catalog

45262). Finally, a 3x relay objective with a diameter of 14 mm (custom designed by Photon Gear Inc, Ontario, NY) is used to relay the front focal plane (within the sample) to the BFP with 3x magnification. Since the focusing NAs of both the illumination and collection beams as well as their crossing angles are enhanced by a factor of ~3x, the spatial resolutions of the DAC system are significantly improved at the trade-off of a reduced FOV of approximately 350 μm by 350 μm.

-- **Figure 4.2** --

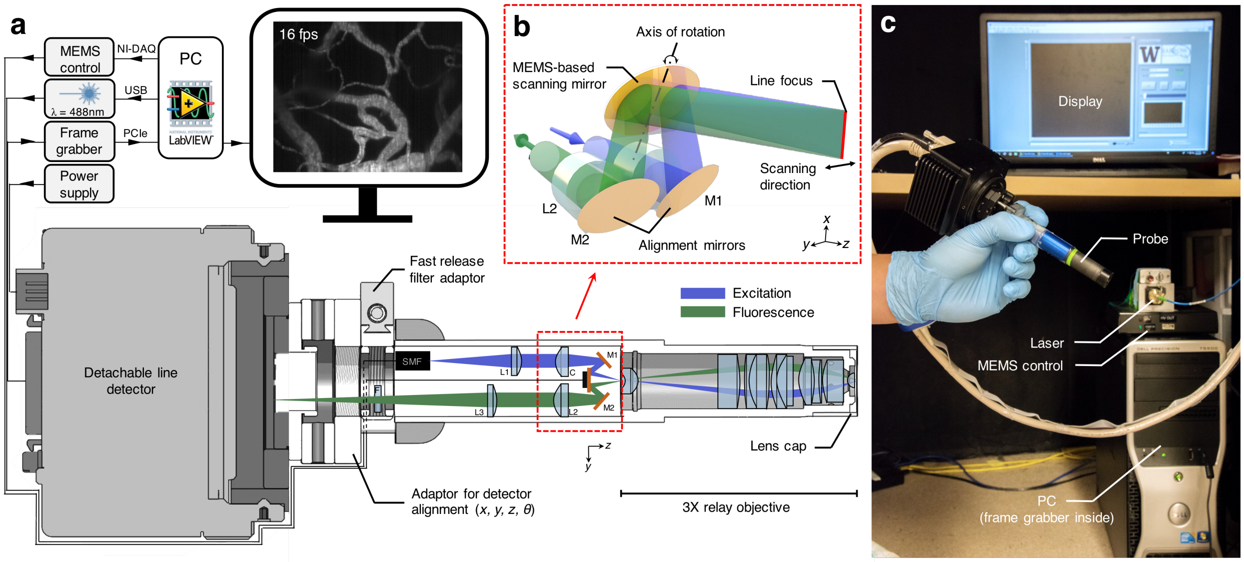

Figure 4.2 Components of the handheld LS-DAC system. (a) A detachable detector is threaded onto the main body via a custom adaptor that provides four degrees of freedom for precise alignment of the detector. All electronics and optics are connected through quick-release connectorized cables. The modular design allows convenient disassembly for shipping and setup in a clinical setting. (b) A zoomed-in view of the LS-DAC scan head, showing the use of a MEMS mirror to scan a focal line in one direction to achieve high-speed 2D imaging. (c) Photograph showing the setup of the entire system, which can fit into a standard surgical cart.

A commercial high-speed complementary-metal–oxide–semiconductor (CMOS) line detector (spL2048-70km, Basler AG, Ahrensburg, Germany) with a pixel spacing of 10 μm is used to sample the focal line at slightly below the Nyquist criterion. Note that the lateral resolution of the system is ~1 µm in the sample, or ~15 µm at the detector plane after magnification by the objective (3x) and collection-path optics (5x). The detector is threaded onto the main body of the device via a custom adaptor that provides a universal SM05-thread interface and four degrees of freedom (x, y, z, and θ) to ensure the precise alignment of the detector (Figure 4.2). The Basler line detector contains two rows of pixels, which are binned to act as a confocal slit with a width of 20 µm. The line images are then streamed into a high-speed frame grabber (PCIe-1473R, National Instruments, Austin, TX) at a line rate of 125.0 µs via a single camera-link cable. The individual line images are stitched into 2D images (500 lines per image) by the on-board processor of the frame grabber before being transferred to the host PC at 16 frames per second (fps). A custom LabVIEW-based user interface was developed to display the images in real time and to allow the user to perform basic operations such as zoom, white- and black-level adjustments, video recording, *etc*.

4.3 Lens cap design and optimization

4.3.1 1st generation lens cap

One limitation of our device is that the objective lens has a fixed working distance, and the imaging depth will be determined by the length the lens cap, i.e., a shorter lens cap allows the tissue to get closer to the probe tip and thus provides a deeper imaging depth. As a proof-of-concept prototype, the first generation lens caps were made of biocompatible Delrin® using an in-house table-top computer numerical control (CNC) milling machine (Othermill®, now commercialized through Bantam Tools, Inc.) with fast turnaround time (<30 minutes per iteration) and low cost (<

$0.1 per unit). Two designs were originally proposed, in which the main difference is the material of the imaging window:

i. the first design incorporates a flexible imaging window made of transparent plastic film, which allows the user to change the imaging depths through changing pressure, providing a convenient and intuitive method to quickly screen for the layer of interests in the tissue.

ii. once a rough imaging depth is determined, a lens cap with a rigid glass cover slip can be used to image a constant depth as the device is being translated. The glass cover slip provides two major advantages: first, better refractive index matching and thus better imaging quality; second, a constant imaging depth that enables the image mosaicking algorithm to extend lateral field-of-view of the device over time. These designs were used at the initial stage of the clinical study and have enabled us to acquire the preliminary results.

-- **Figure 4.3** --

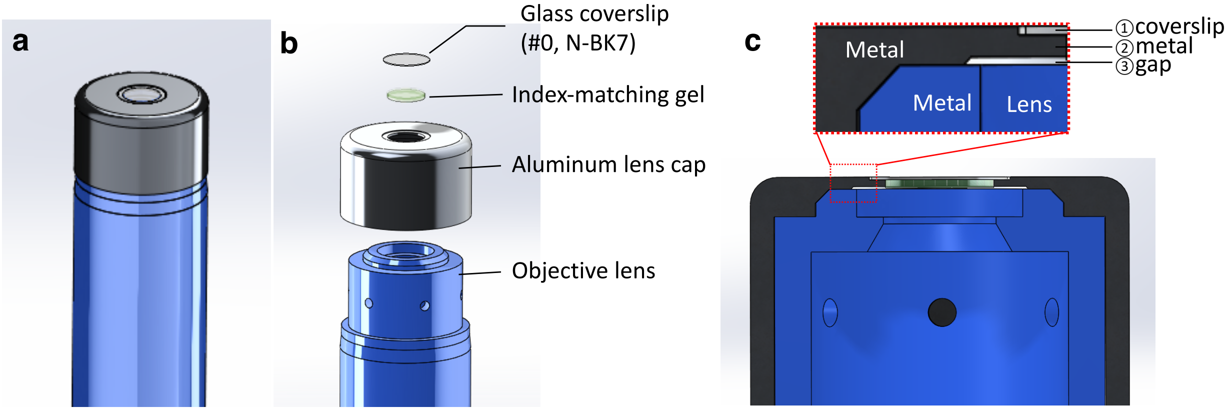

Figure 4.3 The 2nd generation lens cap that is optimized for image-mosaicking. (a) 3D rendering of the imaging head of the microscope with the lens cap on. (b) Exploded view of (a) showing the components of the imaging head. (c) Zoom-in view of the interface between the lens cap and the objective lens.

-- Figure 4.4 --

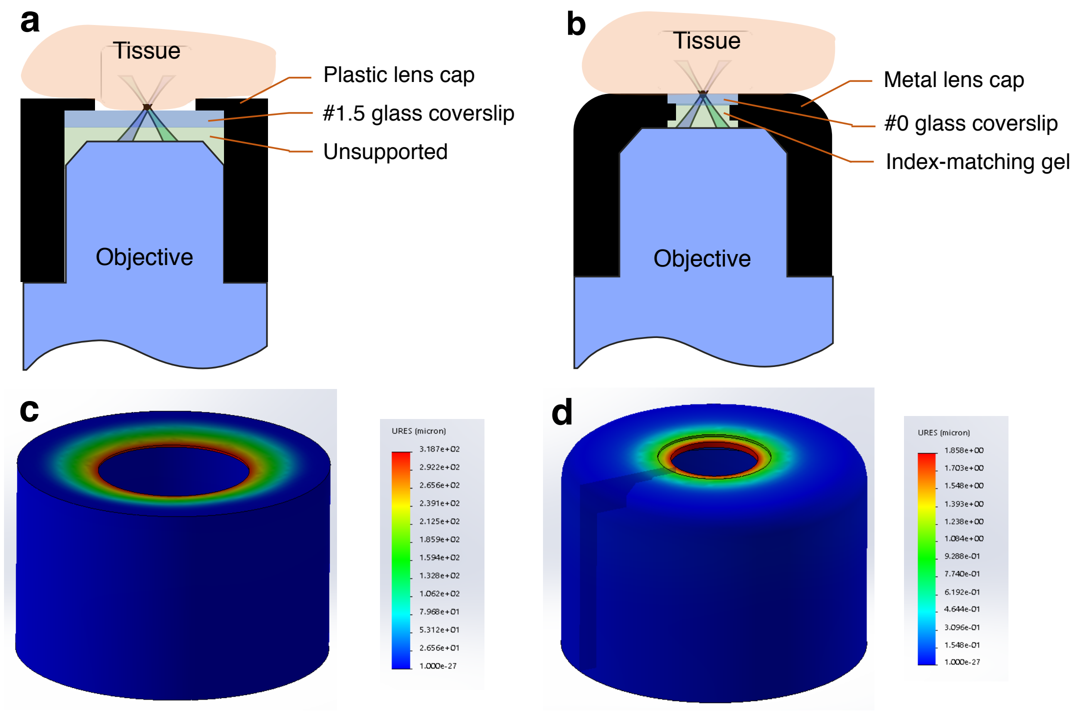

Figure 4.4

Optimization of lens cap designs for image mosaicking. (a) The 1st gen proof-of-concept lens cap that provides imaging depth control of tissue imaging during handheld use and can be iterated rapidly and at low cost. (b) The 2nd gen lens cap is designed to provide maximal mechanical strength and surface flatness to enable high-quality image mosaicking. (c) FEA simulation of the 1st gen design shows a maximal displacement of 318 µm at the front surface in response to a normal force of 5 N. (d) In the 2nd gen design, the displacement is reduced to 1.8 µm with the identical simulation settings.

4.3.2 2nd generation lens cap

During the clinical testing, we found that although the original lens cap design enabled us to acquire the preliminary images with satisfactory performance, it was non-ideal for image mosaicking. As mentioned in the previous chapters, ensuring good feature registration between consecutive image frames is critical for most image-mosaicking algorithms, but with the first generation lens cap design, it was challenging to achieve this task mainly due to two reasons. First, the thin front surface of the lens cap is flexible so that the imaging depth is sensitive to the pressure applied against the tissue. Second, the stepped outer surface results in significant frictions during the translation the device at the tissue surface so that it is challenging to maintain smooth motion. Based on what we have learned from the first-gen lens cap design and from our experience working with clinicians, we designed a new lens cap (Figure 4.3) that is optimized for image mosaicking by providing minimal flexibility to axial pressure changes as well as minimal friction to lateral translations by making the following modifications. First, Delrin was replaced with aluminum, a biocompatible and sterilizable metal with higher mechanical strength and high machinability. Second, the thickness of the glass coverslip was reduced from 180 µm (standard #1.5) to 100 µm (standard #0) in order to maximize metal thickness (Layer 2 in Figure 4.3c). Through ray-tracing simulations in ZEMAX and through imaging experiments, we confirmed that this change in glass thickness does not result in any noticeable change in the image quality, but only a slight focal shift of approximately 20 µm, i.e. the thickness of the metal is effectively increased by 60 µm instead of 80 µm. To mitigate the brittleness and vulnerability of the thinner coverslip, we also reduced the diameter of the window from 10 µm to 5 µm. Third, we re-designed the interior of the lens cap to match to the contour of the objective lens (except for along the optical path) thus maximizing the material (metal) content and supporting structure to withstand pressure. In a finite element analysis (FEA) that simulates the flexibility of the front surface in response to a normal force of 5 N (the estimated maximal force that an user would typical apply), we show that the maximal resultant displacement has been reduced to 1.8 µm from 320 µm as in the original design (Figure

4.4). Furthermore, enabled by high-precision machining, the coverslip is mounted from the outer surface through a groove in a way that the front surface is completely flat (within 10-µm error), in contrast to the previous design in which the coverslip is mounted inward and results in a stepped surface. The metal surface is also polished and the edges are filleted to further minimize friction.

4.4 MEMS-based flat-field scanning & *ex vivo* imaging

To correct for scanning-induced curvature, the MEMS mirror is pistoned with a nonlinear waveform to actuate the surface of the mirror in the vertical direction as the mirror tilts to create an *en face* image (Figure 4.5a). Specifically, based on our preliminary modeling of the mechanically induced field curvature, we determined that an optimal field-flattening waveform would be a rectified sine function $V_z = |A sin(\omega t + \phi)|$, where V_z is the driving voltage of the MEMS mirror along the z-axis, A is the amplitude of the pistoning motion, ω is the frequency of the actuation, which is identical to the frame rate of the system, and ϕ is used to synchronize the field-flattening waveform to the scanning waveform. Importantly, maximal pistoning is performed at the center of the scan (zero tilt) rather than at the edges of the FOV in order to maintain the full tilting range of the MEMS mirror (+/- 5.5 deg), and thus maintaining the FOV of the microscope. Unlike other methods for field flattening [22, 23], our method does not require custom optics or mechanical parts that are difficult to miniaturize, and can be conveniently applied to a high-speed handheld scanning microscope. The field curvature both before and after flat-field correction was characterized by acquiring an image stack in which a flat mirror was scanned in the axial (depth) direction using a linear actuator, and the contour plots are shown in Figure 4.6b.

-- **Figure 4.5** --

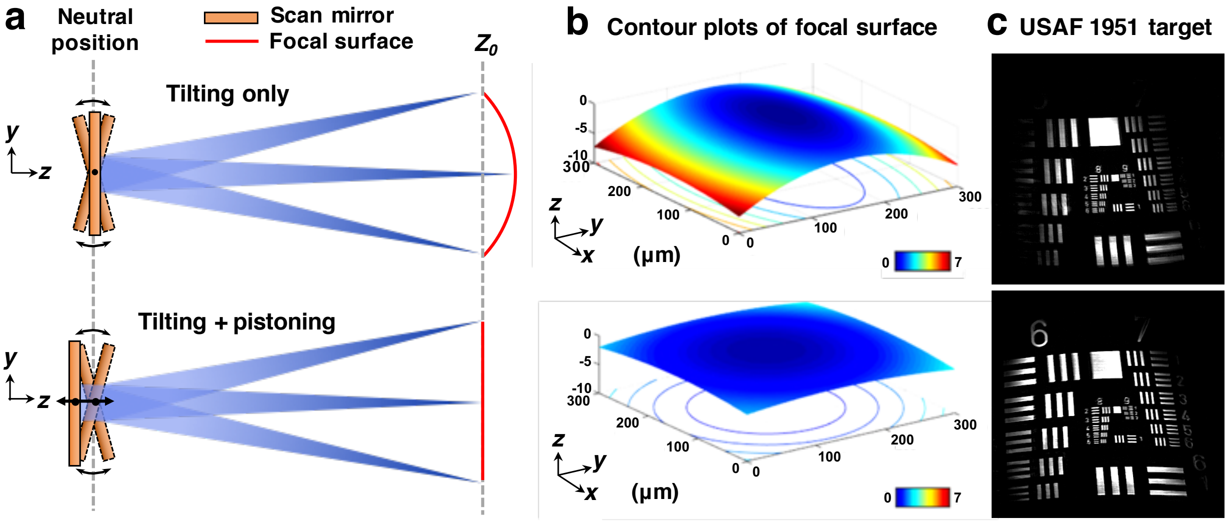

Figure 4.5 Concept and characterization of MEMS pistoning for flat-field correction. (a) A simplified diagram of the scan head, showing that axial pistoning of the MEMS scanner can counteract the curvature induced by the tilting motion. (b) A contour plot of the focal surface showing that the uncorrected field curvature along the *y*-axis (scan direction) of the FOV is > 7 µm in the axial extent, but is reduced to < 2 µm after flat-field correction (which is comparable to the axial resolution of the system). (c) Images of a flat resolution target showing that more of the target is in focus after the flat-field method is applied.

One advantage of a flattened FOV is that it allows more-accurate visualization of thin layered structures. For example, a fresh mouse spleen was stained with 1-mM acridine orange (A6014, Sigma-Aldrich Inc., St. Louis, MO) solution for 30 seconds and then rinsed with 1x phosphate buffered saline (PBS, pH 7.4). As shown in Figure 4.6, the uncorrected system displays a misleading image of the thin mesothelium layer (a cell monolayer) because the image “curves” into the deeper capsule layers (Figure 4.76 c-d). With flat-field correction, a more-realistic *en face* image of a continuous mesothelium is generated (Figure 4.6 f-g).

-- **Figure 4.6** --

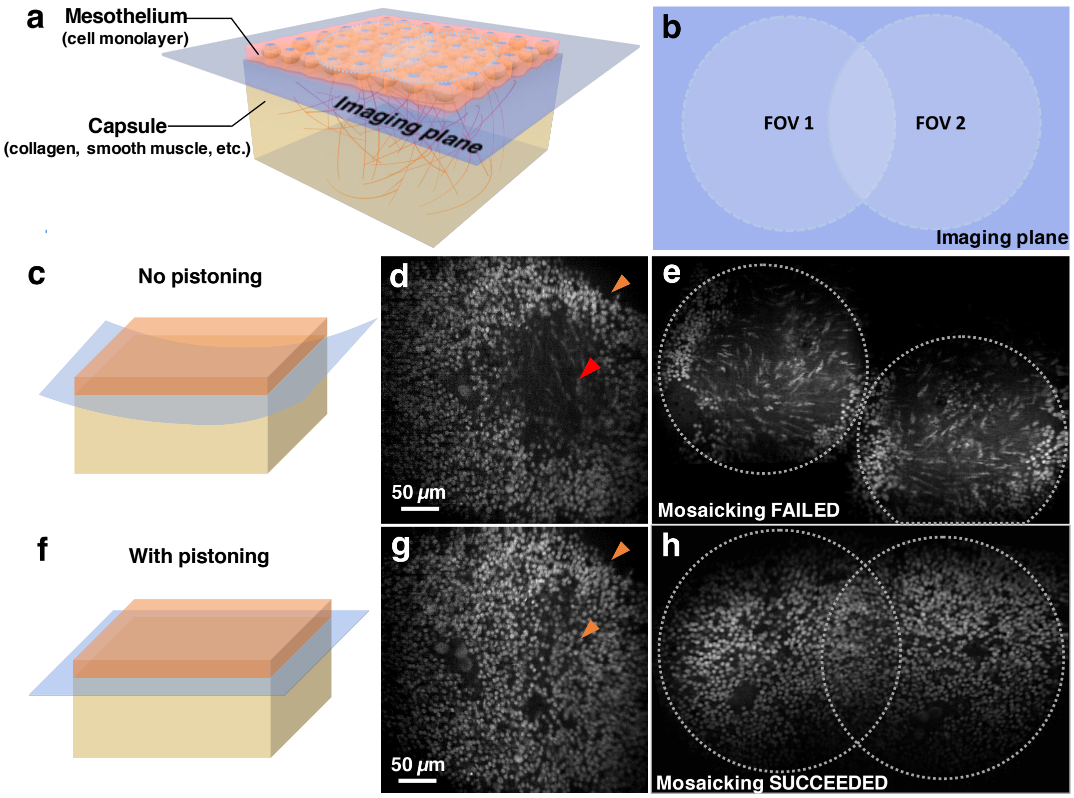

Figure 4.6 A flattened *en face* imaging field improves the ability to image thin layered structures as well as to perform image mosaicking. (a) A 3D model showing the structure at the surface of a mouse spleen. (c, d) The uncorrected system does not display a continuous image of the mesothelium monolayer, but rather shows an image that "curves" into the deeper capsule layers. (f, g) With flat-field correction, a more-accurate image of a continuous mesothelium layer is visualized. (b, e, h) The image mosaicking algorithm fails to stitch together two overlapping image frames acquired with the uncorrected system due to poor registration of features, but succeeds after the field-flattening algorithm is applied.

-- **Figure 4.7** --

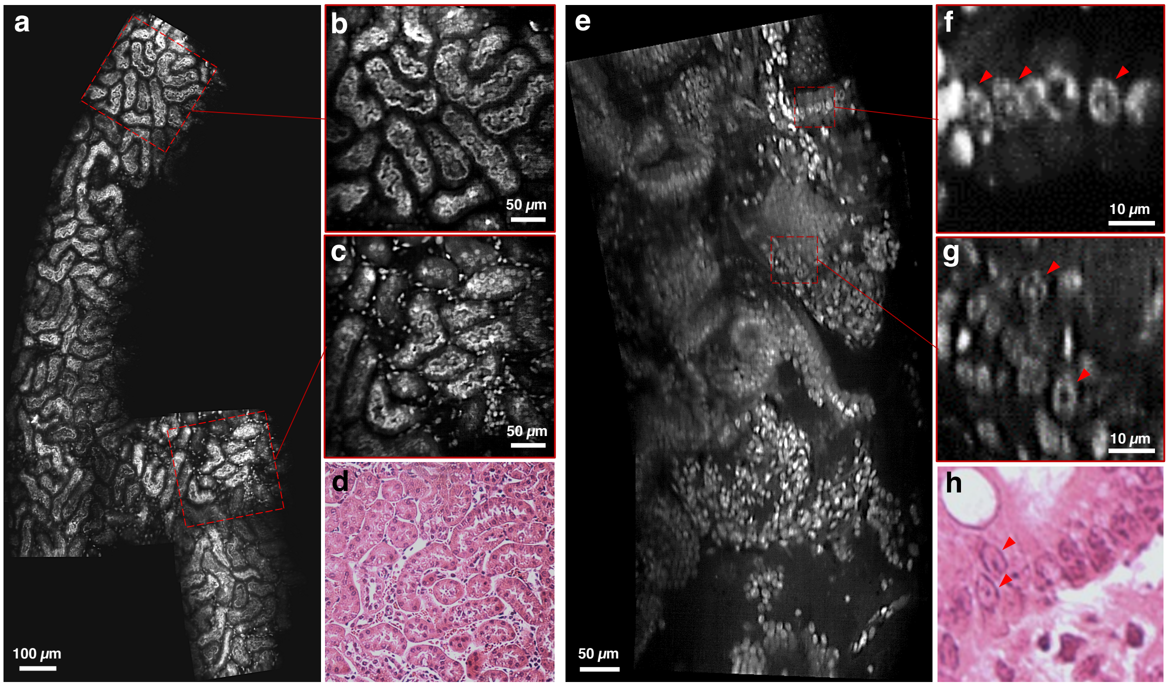

Figure 4.7 Video mosaicking of fluorescently label fresh mouse tissues imaged at 16 fps. (a-c) Sub-tubular structures in the cortex of a fresh mouse kidney are clearly visualized, and (d) agree with corresponding H&E histology. (e-g) Another example in a mouse colon shows that sub-nuclear structures are distinguishable, with good agreement with (h) corresponding H&E histology.

Another critical advantage of flat-field correction is that it improves image mosaicking of overlapping images in order to create a large-FOV image over time (Figure 4.7 e, h). As shown in Figure 4.8, a mosaicked image of a lateral FOV of > 2 mm was obtained from a video sequence of fluorescently labelled mouse tissues obtained at 16 fps. Image mosaicking was achieved through post-processing with MosaicJ [159], an open-source image mosaicking plug-in of ImageJ (National Institutes of Health, Bethesda, MD). For tissue imaging, the sample was placed against a glass coverslip that was mounted on a custom disposable lens cap, and the laser power was measured as 1 mW at the tip of the microscope. The gap between the objective lens and the coverslip was filled with ultrasound gel for refractive index matching.

4.5 *In vivo* imaging in animals

In additional to reducing motion artifact during handheld use, the high frame rate of LS-DAC microscopy, when compared with slower devices, is able to preserve the dynamic information (e.g. the blood flow) in living subjects, providing an invaluable visual dimension *in vivo* imaging. We show that our device is able to monitor the blood flow trafficking in the ear vasculature of a living mouse after injected retro-orbitally with FITC-conjugated high molecular weight dextran (#52471, Sigma-Aldrich Inc., St. Louis, MO). Example still image of the video is shown in Figure 4.8.

-- **Figure 4.8** --

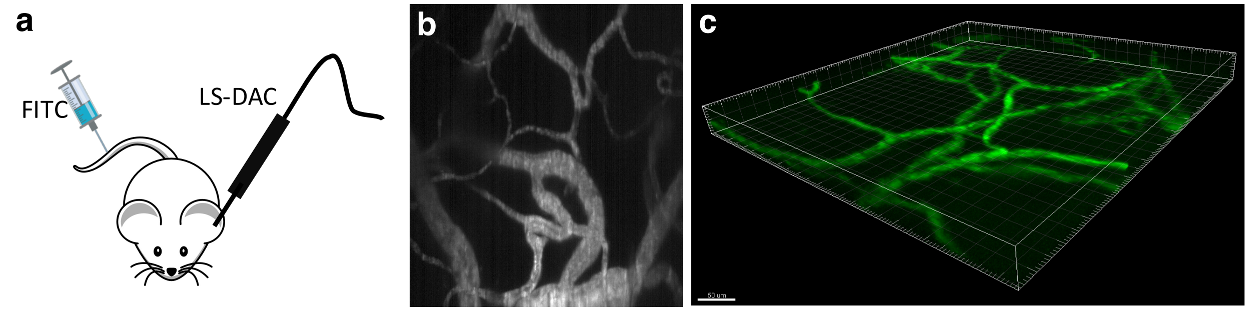

Figure 4.8

In vivo imaging of the vasculature of a mouse ear. (a) The mouse was injected with FITC-conjugated high-MW dextran immediately before imaging. (b) Maximum-intensity projection of a depth range of 50 to 100 µm. The high frame rate (16 Hz) is able to preserve the dynamic information of the red blood cell trafficking. (c) Volumetric rendering of vascular architecture.

4.6 Summary

In summary, we have developed a handheld LS-DAC microscope to provide physicians and other healthcare professionals (e.g. dentists, therapists, etc.) with a real-time and non-invasive alternative to conventional histopathology for the assessment of superficial tissues. Our device is able to achieve a high frame rate of 16 Hz, which preserves dynamic information for *in vivo* imaging and minimizes motion artifacts during handheld use, while maintaining excellent image contrast and resolution that can serve as a real-time surrogate for conventional slide-mounted histology. This device is the first fully packaged handheld LS-DAC microscope, in which a portable line detector has been integrated into the device, along with improved illumination optics (better resolution and contrast than a preliminary prototype). We also developed a novel scanning method that utilizes piston-based actuation of a MEMS scanner to correct for the field curvature induced by the tilting motion of the scanner. This flat-field correction enables more accurate *en face* imaging as well as more effective image mosaicking to sample a large lateral field. In the future, the ability to perform real-time image mosaicking should be of practical value for guiding clinical end users as they strive to sample a large area of tissue. For example, the mosaicks will guide users towards regions that are missed, and will also minimize redundant imaging of other regions. The current system is optimized for imaging fluorescein, a FDA-approved fluorophore that excites at 488 nm. An clinical imaging study of fresh human brain tumors collaborating with the Barrow Neurological Institute (Phoenix, AZ) will be shown in the next chapter. It should be noted that the unique DAC architecture and the modular design of our handheld device will enable the conversion of the current system for other applications, including imaging fluorophores at different wavelengths (e.g. 5-ALA-based), or reflectance imaging, with minimal modifications.

Chapter 5: Clinical evaluation: a pilot study in human gliomas

5.1 Background

In the previous chapter, we described the successful development of a novel handheld line-scanned dual-axis confocal (LS-DAC) microscope system, with preliminary imaging results (both *ex vivo* and *in vivo*) of animal models to demonstrate the satisfactory performance of our imaging system. The promising results have motivated us to move on to collaborate with neurosurgeons and perform a pilot clinical study of seven glioma patients. Through our first experience working with clinicians to image fresh human tumor tissue, we assessed the feasibility of adopting this new technology in the clinical workflow of neurosurgery, and will continue to refine the device to further improve its clinical viability. Furthermore, we have established the first LS-DAC image atlas of human gliomas, and compared our results to similar clinical studies in the literature utilizing commercial handheld confocal microscopes. We show that the unique features of LS-DAC microscope – high-speed, high-resolution, image-mosaicking capability – have properly addressed the aforementioned limitations of commercial systems and have enabled better visualization of histological features in heterogeneous glioma tissue.

5.2 Methods

5.2.1 Ethical approval and patient selection criteria

This study was conducted at the Barrow Neurological Institute (BNI, Phoenix, AZ) and St. Joseph's Hospital and Medical Center, with approval from the St. Joseph Institutional Review Board (IRB No. PHXB-17-0378-30-12). Patients with gliomas undergoing craniotomy for tumor resection were considered to be candidates for the study. Patients under 18 years of age were excluded. Preoperative informed consent was obtained for all patients.

5.2.2 Imaging system

The imaging system (Figure 5.1) used in this study is based on the handheld LS-DAC microscope system described in the previous chapter. In brief, the handheld imaging probe has an outer diameter of 14 mm and a small contact window of 5 mm. The device is capable of providing a field-of-view (FOV) of approximately 350 μm by 350 μm with a lateral resolution ~1 μm and an axial resolution of <2 μm in brain tissue up to 100-μm deep. In this study, we utilize a 488-nm blue diode laser (Omicron LuxX 488) with a maximum power of 1 mW (in tissue) to simulate the laser intensity that would be used for future *in vivo* imaging. All images in this work are acquired at 16 frames per second (fps) and displayed dynamically on the screen in real time. It should be noted that the frame rate can be further increased if necessary at the trade-off of a reduced signal-to-noise ratio (SNR), but in this study, we found that 16 Hz is an optimal frame rate to effectively reduce motion artifacts during handheld use while retaining sufficient SNR. As discussed in the Section 4.3.2, a custom lens cap has been optimized to provide a constant imaging depth at approximately 50-μm beneath the tissue surface. It should be noted that, however, a set of lens caps have also been made to enable multiple imaging depths ranging from 0 to 100 μm, and these lens caps can be swapped conveniently during operation. Importantly, enabled by the high frame rate and the new lens cap design, the device provides smooth and continuous images and is therefore capable of video mosaicking – stitching overlapping video frames to create an extended FOV over time using image processing algorithms – to sample a tissue region comparable in size to a physical biopsy specimen (a few millimeters in scale). The raw video clips from the LS-DAC microscope is processed into large mosaics using Image Composite Editor (Microsoft Inc., Redmond, WA) with the default settings. The probe could be operated as either a handheld unit or mounted onto a mechanical system (such as a translation stage or a Greenberg retractor) for localization of the probe tip.

-- **Figure 5.1** --

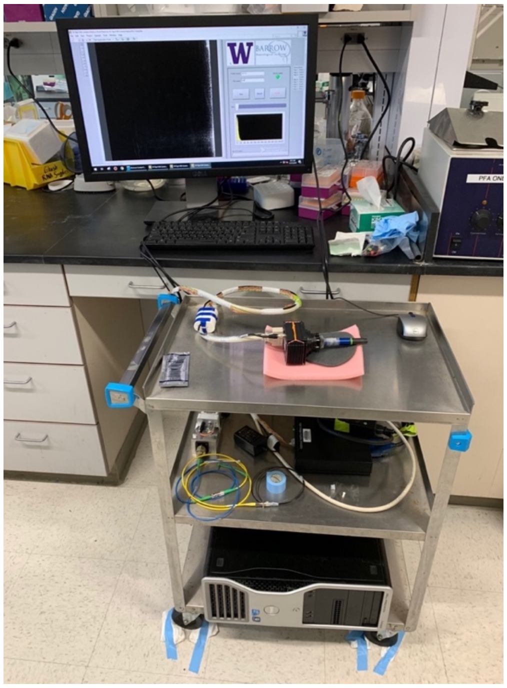

Figure 5.1 The handheld LS-DAC system set up in a standard surgical cart at the BNI. The system can safely transport between the operation room for imaging and a safe location for storage.

5.2.3 Workflow of clinical study

As shown in Figure 5.2, consenting patients at the BNI follow the standard-of-care for glioma management, in which they receive a cytoreductive surgery as the first step to debulk the tumor. During the course of the surgery, biopsies were taken for routine histopathological analysis, and per the IRB protocol, part of the biopsy was collected for our study. The tumor specimen was immediately wrapped with saline-soaked gauze, stored on ice in a sealed container, and then shipped to the University of Washington with overnight freight services.

Upon receipt, the tumor specimen was topically stained with 1-mM acridine orange (A6014, Sigma-Aldrich Inc., St. Louis, MO) for one minute, followed by thorough rinsing with 1x phosphate-buffered saline (PBS) to remove non-specific staining. The exposed surface was imaged with the handheld LS-DAC microscope at 16 fps. Subsequently, the tissue was physically sectioned in the *en face* direction (as close and parallel to the tissue surface as possible) and mounted on glass slides following standard histopathology procedures. The slides were then stained with hematoxylin & eosin (H&E), and reviewed by a board-certified neuropathologist at the University of Washington Medical Center to identify hallmarks of glioma tissues, as a reference for the LS-DAC images.

-- **Figure 5.2** --

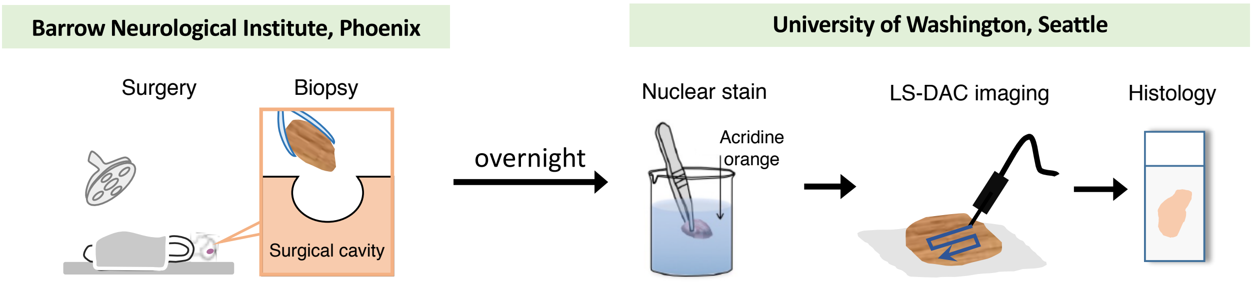

Figure 5.2 Workflow of the clinical study. Glioma patients at the BNI undergo a standard surgery to remove the bulk of the tumor, and a biopsy is taken for routine histopathology. A portion of the biopsy is saved for the pilot clinical study. At UW, the specimen is topically stained with acridine orange and imaged with the LS-DAC microscope to identify histological features of gliomas. The same specimen is then submitted for gold-standard hematoxylin & eosin (H&E) staining and the histology slides are reviewed by a board-certified neuropathologist to confirm the results.

5.3 Results

One of the limitations of high-resolution microscopy for neurosurgical guidance is the difficulty of ensuring that a sufficiently large area of the brain is sampled at each imaging location. While comprehensive imaging of the entire tumor cavity is not needed, there is enough tissue heterogeneity such that the 350 by 350 µm FOV of a handheld confocal microscope may not represent the average properties of the tissue within a particular region of the brain. Therefore, real-time video mosaicking would be of value to provide a larger effective FOV as the device is manipulated over the tissue surface over time. Such mosaicking would not only free the user from mentally integrating the tissue properties (histological features), but would also guide the user to image regions that have been missed, and/or to avoid regions that have already been imaged (i.e. covering the surface as efficiently as possible). Indeed, from the clinical testing, we find that the unique image-mosaicking capability of our LS-DAC system is highly valuable for neurosurgical guidance as it provides a more accurate representation of the overall cytoarchitecture of heterogeneous tissue (Figure 5.3), as well as large histopathological hallmarks of gliomas such as necrosis (Figure 5.4) and vasculature (Figure 5.5).

5.4 Image atlas: LS-DAC images of human gliomas

This section showcases the first image atlas of human glioma histology using LS-DAC microscopy to provide the community with a reference for future large-scale clinical studies. The LS-DAC images are categorized based on the four main criteria used for glioblastoma diagnosis (i.e. cellularity, mitosis, vasculature, and necrosis) and the corresponding gold-standard H&E histology is also provided. This atlas is available at full resolution on an online repository maintained by our group, and will be updated as more images become available.

-- **Figure 5.3** --

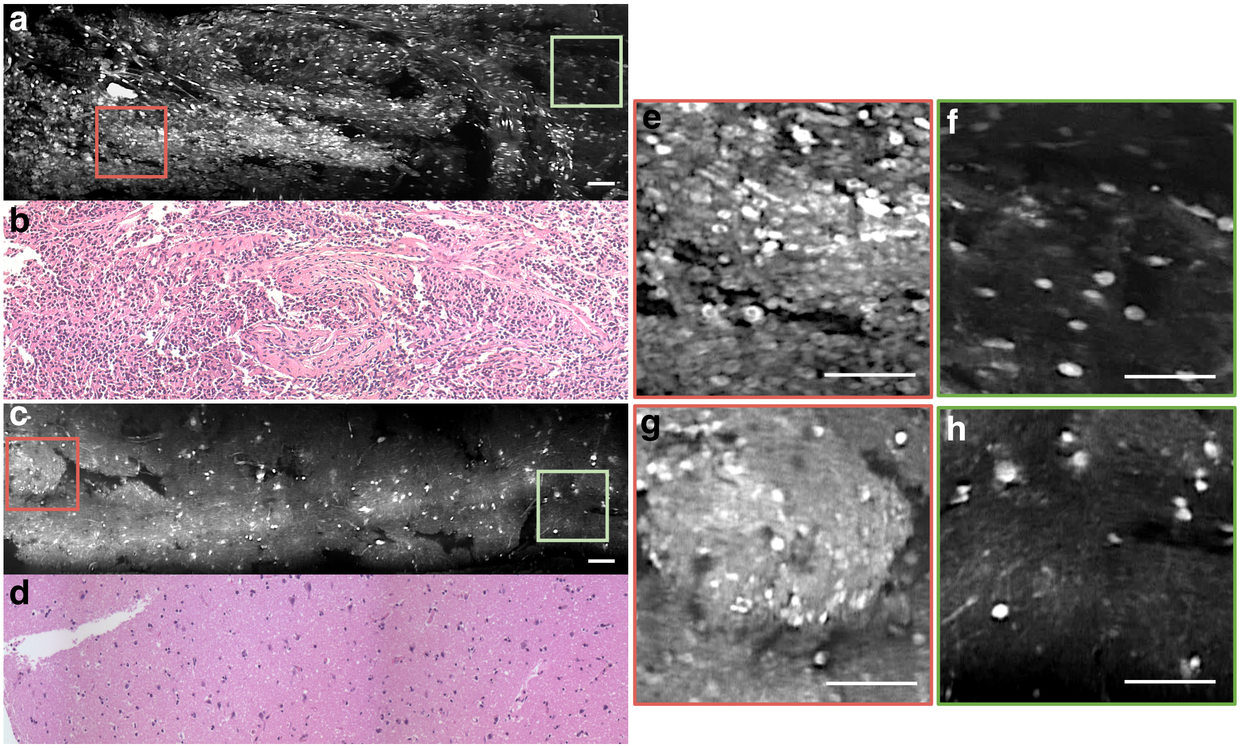

Figure 5.3 (a) Mosaicked LS-DAC image of a human brain biopsy with hypercellularity, confirmed with (b) the corresponding H&E image. (c) Mosaicked LS-DAC image of human brain biopsy with an overall normal cytoarchitecture, confirmed with (d) the corresponding H&E image. While the mosaics provide a non-ambiguous assessment of the distinct characteristics of the two regions, (e, f) the individual image frames of (a) can present similar characteristics to those of (g, h), the individual image frames of (c). Scale bars represent 100 μm.

--- **Figure 5.4** --

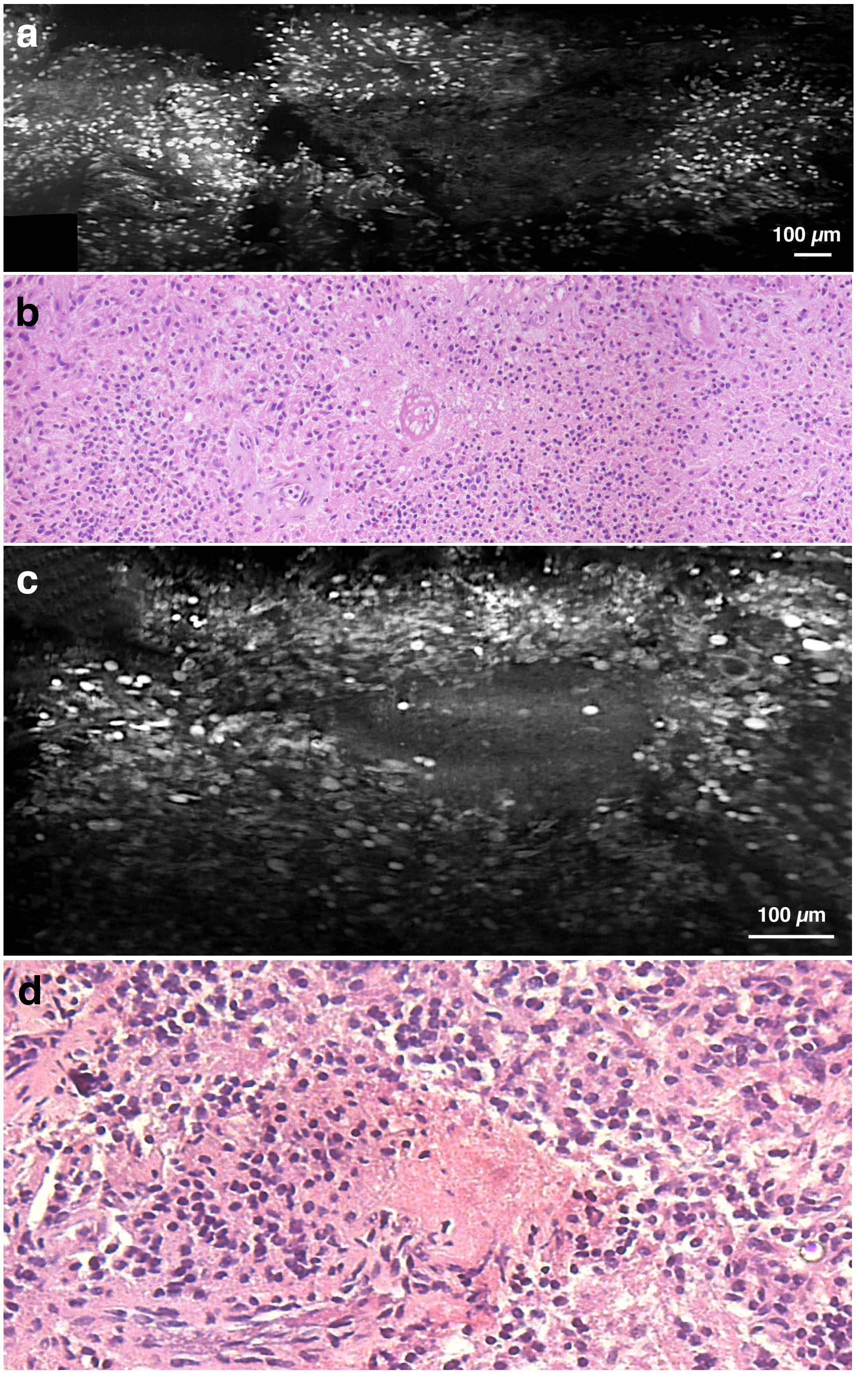

Figure 5.4 Examples of LS-DAC images showing the necrotic regions in human gliomas (topically stained with acridine orange), with the corresponding H&E-stained histopathology.

-- **Figure 5.5** --

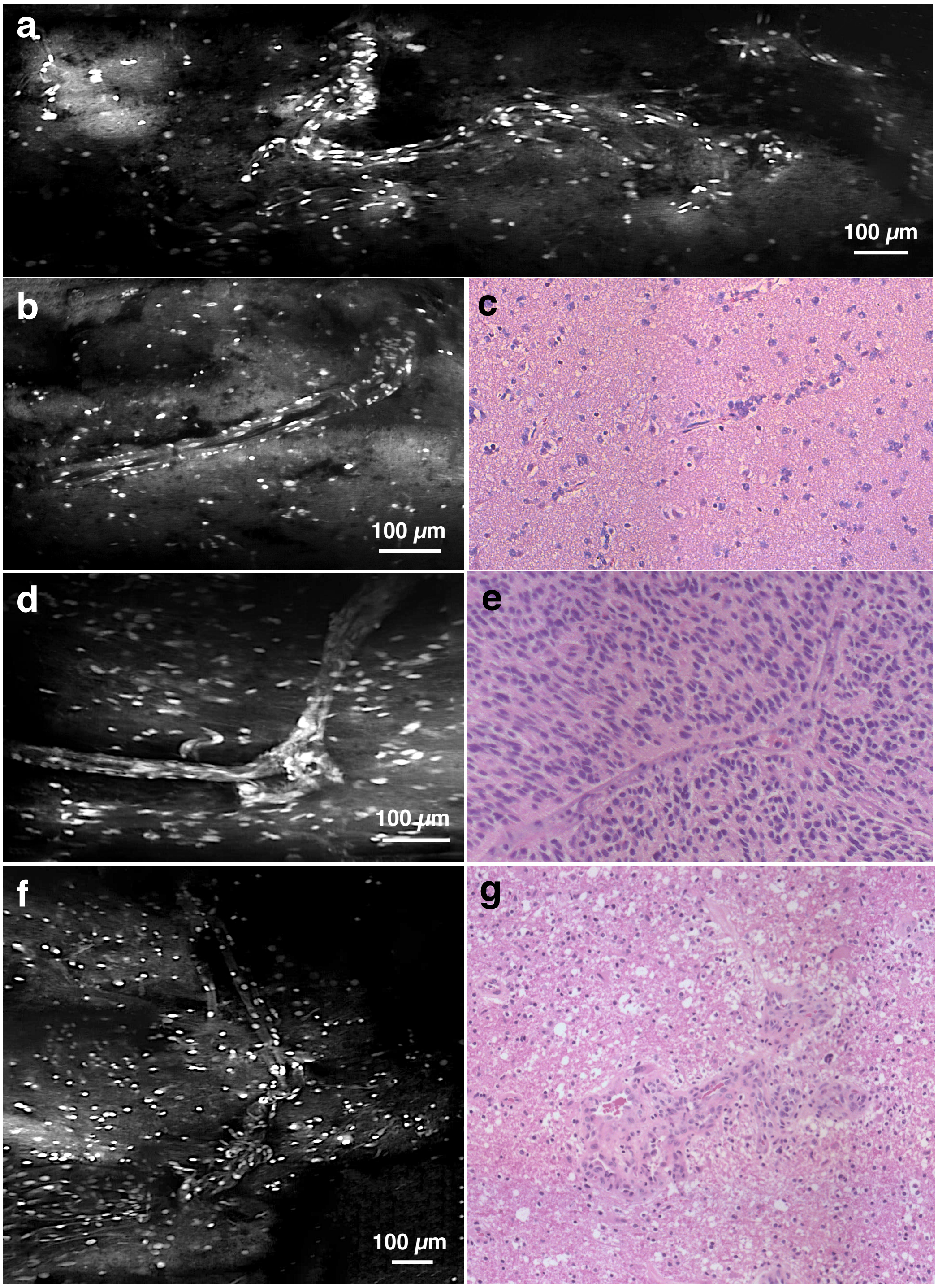

Figure 5.5 Examples of LS-DAC images showing the vasculature in human gliomas (topically stained with acridine orange), with the corresponding H&E-stained histopathology.

-- **Figure 5.6** --

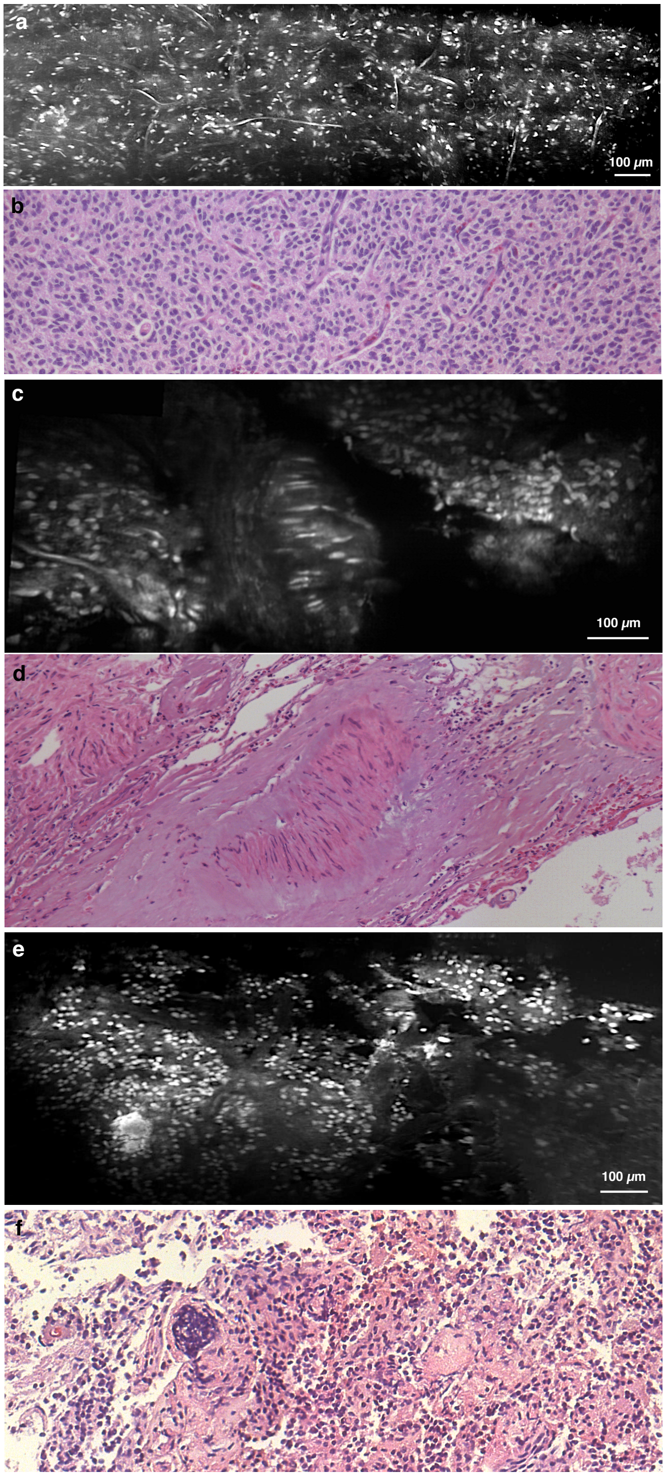

Figure 5.6

Examples of LS-DAC images showing a variety of cellularity in human gliomas (topically stained with acridine orange), with the corresponding H&E-stained histopathology.

-- **Figure 5.7** --

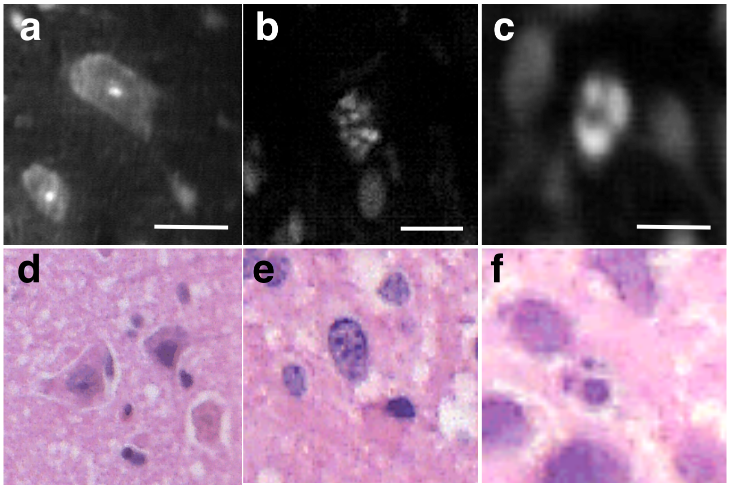

Figure 5.7 Examples of LS-DAC images showing a variety of sub-cellular features including mitosis in human gliomas (topically stained with acridine orange), with the corresponding H&E-stained histopathology. Scale bars represent 10 μm.

5.5 Summary and conclusion

This chapter presents our findings from the first clinical study (*ex vivo*) of a newly developed handheld LS-DAC microscope for fluorescence-guided neurosurgery. This study evaluates and optimizes the image quality, safety, and ergonomic factors of the device. We are able to identify important hallmarks of gliomas (e.g. hypercellularity, necrosis, microvascular proliferation, and mitosis) with image quality that approaches that of the gold-standard H&E histology. We also show that image-mosaicking is highly valuable as it provides more accurate representations of heterogeneous tissue as well as better visualizations of large histological features. From our experience working with seven glioma patients, we believe that it is feasible to incorporate this device in upcoming *in vivo* first-in-human studies and the eventual clinical adoption of the device in the surgical theater as a routine imaging tool. However, it will be important to address the remaining challenges that will be discussed in the next chapter.

Chapter 6: Summary and perspectives

6.1 Summary of work

This manuscript documents the development of a novel handheld confocal microscope for neurosurgical guidance, including results from device prototyping through clinical testing. This handheld microscope is based on the line-scanned dual-axis confocal (LS-DAC) architecture, a relatively new variation of confocal microscopy that utilizes (1) low-NA beams to achieve effective optical sectioning and superior image contrast in biological tissues and (2) simple low speed (20-30 Hz) miniature scanners to achieve video-rate imaging. In Chapter 1, the current clinical problems and standard-of-care of gliomas, an extremely deadly disease is discussed. The emerging field of fluorescence-guided neurosurgery as a promising solution to the clinical problem, and the state-of-the-art technologies for fluorescence visualization, are surveyed and compared. This analysis reveals the need of a probe-based high-resolution high-sensitivity microscopy as a powerful complement to most commonly used wide-area low-resolution surgical microscopes. This chapter is based on a recent review article in *Journal of Neuro-oncology* [27]. In Chapter 2, the principle and the variations of dual-axis confocal (DAC) microscopy are reviewed, with a focus on the most recent development of the line-scanned version DAC (LS-DAC), which has been shown as a promising optical sectioning design for high-speed high-resolution handheld probes. This chapter has been based on a recent review article in the *IEEE Journal of Selected Topics in Quantum Electronics* [160]. In Chapter 3, a tabletop LS-DAC microscope was optimized in a pilot clinical study to validate the feasibility of using LS-DAC microscopy to visualize and quantify the microscopic expression of PpIX fluorescence in human glioma biopsy, which is potentially impactful in the field of fluorescence-guided neurosurgery. In this work, a set of tools have also been developed to ensure reliable and reproducible PpIX quantification using optical-sectioning microscopy. This work has been summarized in an article in *Journal of Biomedical Optics* [125]. In Chapter 4, a handheld version of the LS-DAC microscope was developed and its performance was evaluated using animal models. The device shows both excellent frame rate and image quality when compared with similar devices in the market. A novel MEMS-based flat-field scanning mechanism has also been developed to further enhance the potential of the handheld LS-DAC system as a powerful intraoperative imaging tools. This work was summarized in a recent publication in *Optics Letters*. In Chapter 5, we report our first experience collaborating with neurosurgeons in utilizing this new technology to image fresh human brain tissue, showing the feasibility and advantages of using a handheld high-resolution, image-mosaicking LS-DAC microscope for improving glioma resections. Through the clinical testing, we also made a number of technical advancements and optimizations on both the hardware and software to further improve the clinical viability of the device. This work has been summarized in a manuscript under development.

6.2 Perspectives

The ultimate goal of this project is to improve the completeness of glioma resections by providing a high-resolution imaging tool for the neurosurgeons to delineate tumor margins intraoperatively. As mentioned earlier in Chapter 1, a new contrast agent for fluorescence-guided surgery (FGS), 5-ALA, has emerged as a standard-of-care for guiding HGG resections [65, 70, 161-176], has recently received FDA approval for routine neurosurgical guidance. In spite of its clear benefits, 5-ALA-based FGS still suffers from a number of shortcomings that have been detailed in Section 1.3. In brief, the current technique lacks the sensitivity to detect individual tumor cells even if they are properly labeled, and also, the visible fluorescence generated is usually interpreted subjectively [177] and is difficult to quantify because the visualized fluorescence is greatly affected by light-tissue interactions such as absorption and scattering, as well as detection parameters such as the angle and working distance of the microscope [27, 48]. While spectroscopy-based methods have been developed to mitigate these shortcomings, they are typically limited to sampling localized points of tissue at low spatial resolution rather than generating a more-intuitive image of the tissue with structure information. Our work in developing a high-speed handheld confocal microscopy with video-mosaicking capabilities has shown that this new technology has properly addressed these limitations. We believe that this device can be powerful tool to achieve optimal EOR for the ultimate benefit of patients suffering from both LGGs and HGGs. As we continue to refine the handheld LS-DAC microscope for 5-ALA-based neurology, we hereby provide a perspective on the future clinical workflow in which quantitative high-resolution microscopy is implemented, and outline the key challenges to overcome and potential strategies to facilitate the clinical acceptance of this new technology [178].

6.2.1 Proposed clinical workflow

In the current clinical workflow for 5-ALA-based FGS, glioma margins are defined by pre-operative or intraoperative magnetic resonance imaging (MRI), as well as wide-field (low-power) surgical microscopy. However, since all gliomas are diffuse and ill-defined, the contrast-enhancing regions revealed by these wide-field imaging methods (e.g. Gd-enhancement for HGGs, T2-hyperintensity for LGGs, and macroscopic PpIX fluorescence for most HGGs) are not indicative of the actual extent of tumor infiltration. While frozen-section histopathology can confirm tissue status during the course of glioma resection, this strategy is invasive (requiring a physical biopsy) and time consuming. Our hypothesis, to be investigated in future prospective studies, is that when operating on gliomas adjacent to eloquent cortical and subcortical pathways, quantitative high-resolution microscopy can be used at the final stages of resection to interrogate tumor burden and other quantitative biomarkers at multiple suspicious sites in order to optimize the EOR (including beyond the radiographic margins) without jeopardizing functional pathways. As shown in Figure 6.2, a specific workflow for future clinical use is provided below:

(1) At the initial stages of the surgery, standard neurosurgical methods will be used for debulking the central portions of the tumor. As the neurosurgeon approaches the radiographic or functional boundaries of the tumor (indicated by anatomical / visual cues, MRI-based neuronavigation, intraoperative stimulation mapping, and 5-ALA-based FGS using wide-field surgical microscopy), regions adjacent to non-eloquent brain can be resected more aggressively to minimize residual tumor burden.

(2) At the final stages of surgery, ambiguous regions at critical locations (e.g. near eloquent brain) will be probed with high-resolution video-mosaicked microscopy of the exposed tissue surfaces, enabling a quantitative measure of microscopic PpIX expression that should ideally correlate with clinicopathologic metrics such as tumor burden and proliferative/mitotic index in order to guide operative decision-making. This provides a non-invasive and real-time alternative to intraoperative consultation with frozen-section histology. It should be noted that similar sterile probe-based microscopy/spectroscopy strategies have been implemented during neurosurgeries, as described in several reports [34, 36, 44, 179, 180].

(3) Conventional surgical tools (e.g. ultrasonic aspirator, suction catheters, etc.) will be used in an iterative process with intraoperative microscopy until optimal resection has been achieved. Ideally, neuronavigation would be used to track the spatial coordinates of all surgical

devices (microscope, suction catheters, etc.) to ensure good co-registration between iterative rounds of imaging and resection.

-- Figure 6.1 --

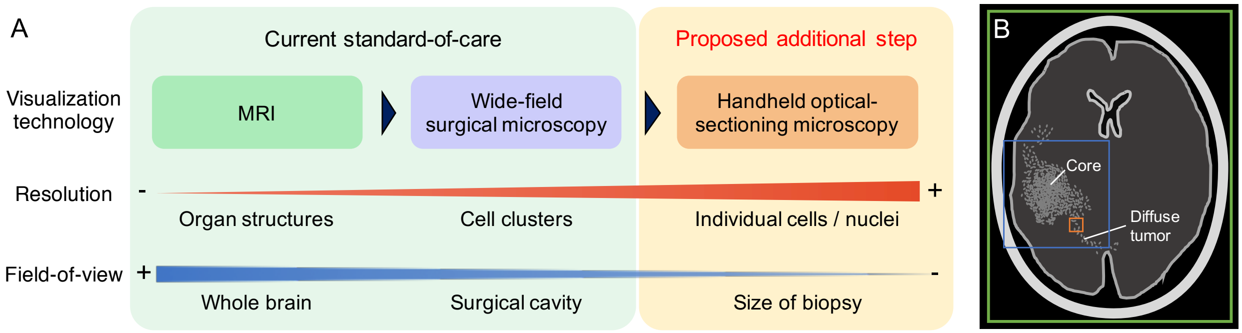

Figure 6.1

Comparison of routine and emerging imaging techniques for neurosurgical guidance. (A) In the current standard-of-care, pre-operative MRI is used to assess the location and size of the bulk tumor, and wide-field surgical microscopy is used intraoperatively to guide debulking. Neither method provides sufficient spatial resolution or sensitivity to effectively visualize diffuse tumors at the surgical margins. Handheld optical-sectioning microscopy is an intraoperative imaging technique that provides superior resolution and sensitivity to detect infiltrating tumor cells at the margins, and can be potentially used to quantify tumor parameters at localized regions at the final stages of resection. (B) The colored boxes indicate the relative field-of-view (FOV) of the imaging modalities described. Larger FOVs are advantageous to mitigate sampling errors when imaging heterogeneous tissues, but typically require trade-offs in terms of resolution and sensitivity. Green: MRI. Blue: wide-field microscopy. Orange: optical-sectioning microscopy with mosaicking.

-- **Figure 6.2** --

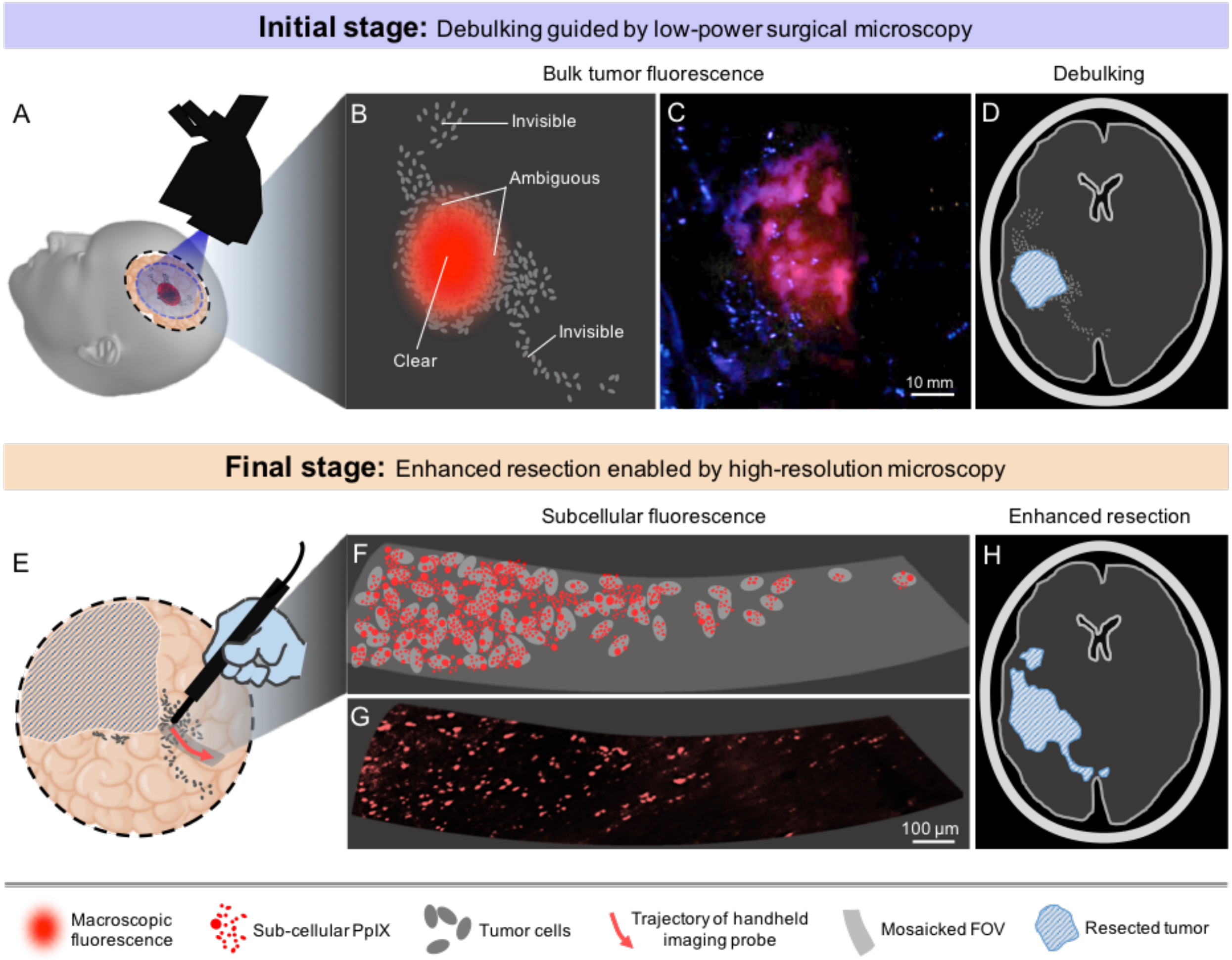

Figure 6.2

Proposed clinical workflow of 5-ALA-based fluorescence-guided neurosurgery. (A) Conventional low-power fluorescence surgical microscopy provides a wide FOV that often covers the entire surgical cavity. (B) Macroscopic PpIX fluorescence is visible at the central portions of most HGGs, but not at the infiltrative margins. (C) Example low-power fluorescence microscopy image of PpIX expression from a bulk HGG region. The margins of the tumor are subjectively delineated and ambiguous. (D) Debulking guided by macroscopic PpIX fluorescence, resulting in residual tumor burden. (E) High-sensitivity probe-based optical-sectioning microscopy is used to examine localized regions near the surgical margins, providing a non-invasive alternative to intraoperative frozen section histopathology. (F) Visualization of subcellular PpIX fluorescence can potentially enable quantification of tumor parameters in order to guide surgical decisions at the final stages of resection. (G) Example image of microscopic PpIX fluorescence in a HGG biopsy using high-resolution optical-sectioning microscopy. (H) Optimal extent of resection is achieved after iterative tumor resection guided by video-mosaicked handheld optical-sectioning microscopy.

6.2.2 Challenges & future work

A number of translational milestones should ideally be achieved in order to bolster confidence in a high-resolution intraoperative imaging technique for adoption by surgeons. First, and perhaps the most critical step, is to establish a biological context and understanding of the pattern of sub-cellular PpIX expression that is visualized with an optical-sectioning microscope. Note that numerous studies have already shown that PpIX expression provides specific delineation of a variety of neoplasms under wide-field (low-resolution) imaging and spectroscopy [181-183], including a general correlation between PpIX concentrations and proliferative score as well as World Health Organization (WHO) histologic score [181]. Preliminary studies (e.g. using high-resolution *in vivo* microscopy [11], or using fluorescent-activated cell sorting of dissociated human cells [unpublished data]) have also shown that PpIX expression at the cellular level is highly tumor-specific. However, larger-scale correlation studies are needed to improve our ability to interpret high-resolution images of PpIX in gliomas. For example, studies should ideally demonstrate a clear correlation between subcellular patterns of PpIX fluorescence and well-established clinicopathologic metrics such as tumor burden and proliferative/mitotic index (e.g. Ki-67 and pHH3 expression). Facilitated by the recent advancements in both imaging hardware (e.g. open-top light-sheet microscopy [132]) and artificial intelligence (e.g. deep-learning algorithms for classification and regression tasks), it should be possible to perform large correlative studies within a reasonable timeline. A second milestone, as mentioned previously, is to mitigate sampling bias due to tissue heterogeneity and to more-closely match the spatial precision of current surgical tools (typically several millimeters in scale). While it is technically challenging to engineer high-resolution microscopes with such large FOVs, robust computer vision algorithms have been developed and continue to be refined to stitch overlapping image frames together to create an extended FOV in real time while an imaging device is translated along the tissue surface [184-189].

It bears repeating that the goal of optical-sectioning microscopy is NOT to image deeply, but rather to perform quantitative imaging near the exposed tissue surface, which requires the high contrast of an optical-sectioning device. However, in practice, the ability to image over a shallow range of depths (<150 microns) may be of practical value to identify an optimal depth where image quality and tissue integrity are maximized. Complementary imaging modalities for detecting PpIX fluorescence from deep subsurface tumors [50, 54, 56] are beyond the scope of this work. In terms of resolution, since current resection tools lack the spatial precision of a high-resolution microscope, the value of high-resolution imaging is not to enable cellular-scale resection, but to enable accurate quantification of PpIX, which in turn should correlate with relevant metrics of tumor burden/proliferation to guide surgical decisions. As with all innovative technologies, clinical validation is needed through well-powered and controlled studies. For example, “malignancy scores” based on quantitative PpIX microscopy should agree with traditional assessment methods such as histopathology and post-operative MRI, and should also be predictive of patient outcomes (e.g. recurrence). Note that for most glioma patients, adjuvant radiotherapy is a logical next-step following tumor resection. The development of technology that enables microscopic quantification of tumor burden and proliferation, and therefore identification of resection cavity regions with high-risk of tumor recurrence, could also inform postoperative radiotherapy planning and improve the efficacy of radiation-based strategies to control tumor progression. In terms of hardware development, there is also considerable work remains in the pursuit of the clinical translation of this device. For example, a real-time video mosaicking algorithm would guide the user to image regions that have been missed, as well as to avoid regions that have already been imaged, and thus allowing the user to examine the tissue surface as efficiently as possible. Also, the user-friendliness of the device can be further improved by using more compact high-speed high-sensitivity line detectors, and equipping with either a zoomable objective lens or a motorized lens cap that provides interactive and precise depth adjustability (instead of through swapping the lens caps). Finally, it is also worth exploring the feasibility of fusing with external sensory data (e.g. from inertial measurement units, neuronavigation systems, motion-tracking cameras, etc.) to improve the accuracy and robustness of the current video-mosaicking algorithm, which is currently image-based.

In summary, the recent FDA approval of 5-ALA-based FGS and the advancement of handheld LS-DAC microscopy have provided a unique opportunity to improve glioma surgeries. We believe that the device described in the manuscript will have an important role to play in improving the EOR for glioma surgeries through quantitative and reproducible delineation of the infiltrative margins of diffuse gliomas, for which current techniques fail to provide adequate guidance at the final most-critical stages of resection procedures. The successful translation of this technology will require collaborative efforts amongst multidisciplinary teams that include optical engineers, neurosurgeons, pathologists/biologists, computer scientists, industry partners, and regulatory/reimbursement stakeholders. Together with wide-field imaging techniques such as MRI and low-power surgical microscopy, we believe that the use of intraoperative high-resolution microscopy within the surgical armamentarium should yield significant improvements in glioma patient outcomes.

BIBLIOGRAPHY

[1] N. Sanai and M. S. Berger, "Surgical oncology for gliomas: the state of the art," *Nat Rev Clin Oncol,* Nov 21 2017, doi: 10.1038/nrclinonc.2017.171.

[2] Q. T. Ostrom *et al.*, "CBTRUS Statistical Report: Primary brain and other central nervous system tumors diagnosed in the United States in 2010-2014," *Neuro Oncol,* vol. 19, no. suppl_5, pp. v1-v88, Nov 6 2017, doi: 10.1093/neuonc/nox158.

[3] D. A. Hardesty and N. Sanai, "The value of glioma extent of resection in the modern neurosurgical era," *Front Neurol,* vol. 3, p. 140, 2012, doi: 10.3389/fneur.2012.00140.

[4] R. Ahmadi *et al.*, "Long-term outcome and survival of surgically treated supratentorial low-grade glioma in adult patients," *Acta Neurochir (Wien),* vol. 151, no. 11, pp. 1359-65, Nov 2009, doi: 10.1007/s00701-009-0435-x.

[5] J. S. Smith *et al.*, "Role of extent of resection in the long-term outcome of low-grade hemispheric gliomas," *J Clin Oncol,* vol. 26, no. 8, pp. 1338-45, Mar 10 2008, doi: 10.1200/JCO.2007.13.9337.

[6] E. B. Claus *et al.*, "Survival rates in patients with low-grade glioma after intraoperative magnetic resonance image guidance," *Cancer,* vol. 103, no. 6, pp. 1227-33, Mar 15 2005, doi: 10.1002/cncr.20867.

[7] S. L. Hervey-Jumper and M. S. Berger, "Role of surgical resection in low- and high-grade gliomas," *Curr Treat Options Neurol,* vol. 16, no. 4, p. 284, Apr 2014, doi: 10.1007/s11940-014-0284-7.

[8] N. Sanai, M. Y. Polley, M. W. McDermott, A. T. Parsa, and M. S. Berger, "An extent of resection threshold for newly diagnosed glioblastomas," *J Neurosurg,* vol. 115, no. 1, pp. 3-8, Jul 2011, doi: 10.3171/2011.2.JNS10998
10.3171/2011.7.JNS10238.

[9] G. E. Keles, K. R. Lamborn, and M. S. Berger, "Low-grade hemispheric gliomas in adults: a critical review of extent of resection as a factor influencing outcome," *J Neurosurg,* vol. 95, no. 5, pp. 735-45, Nov 2001, doi: 10.3171/jns.2001.95.5.0735.

[10] N. Sanai, M. Y. Polley, and M. S. Berger, "Insular glioma resection: assessment of patient morbidity, survival, and tumor progression," *J Neurosurg,* vol. 112, no. 1, pp. 1-9, Jan 2010, doi: 10.3171/2009.6.JNS0952.

[11] N. Sanai *et al.*, "Intraoperative confocal microscopy in the visualization of 5-aminolevulinic acid fluorescence in low-grade gliomas," *J Neurosurg,* vol. 115, no. 4, pp. 740-8, Oct 2011, doi: 10.3171/2011.6.JNS11252.

[12] I. J. Gerard, M. Kersten-Oertel, K. Petrecca, D. Sirhan, J. A. Hall, and D. L. Collins, "Brain shift in neuronavigation of brain tumors: A review," *Med Image Anal,* vol. 35, pp. 403-420, Jan 2017, doi: 10.1016/j.media.2016.08.007.

[13] H. El-Hateer *et al.*, "Low-grade oligodendroglioma: an indolent but incurable disease? Clinical article," (in English), *J Neurosurg,* vol. 111, no. 2, pp. 265-271, Jul 31 2009, doi: 10.3171/2008.11.JNS08983.

[14] T. B. Johannesen, F. Langmark, and K. Lote, "Progress in long-term survival in adult patients with supratentorial low-grade gliomas: a population-based study of 993 patients

in whom tumors were diagnosed between 1970 and 1993," (in English), *J Neurosurg,* vol. 99, no. 5, pp. 854-862, Oct 31 2003, doi: 10.3171/jns.2003.99.5.0854.

[15] D. B. Mansur *et al.*, "Low grade gliomas treated with adjuvant radiation therapy in the modern imaging era," (in English), *Am J Clin Oncol,* vol. 23, no. 3, pp. 222-226, May 31 2000. [Online]. Available: http://www.ncbi.nlm.nih.gov/entrez/query.fcgi?db=pubmed&cmd=Retrieve&dopt=AbstractPlus&list_uids=10857881.

[16] M. J. McGirt *et al.*, "Extent of surgical resection is independently associated with survival in patients with hemispheric infiltrating low-grade gliomas," (in English), *Neurosurgery,* vol. 63, no. 4, pp. 700-7- author reply 707-8, Sep 30 2008, doi: 10.1227/01.NEU.0000325729.41085.73.

[17] M. Nakamura *et al.*, "Analysis of prognostic and survival factors related to treatment of low-grade astrocytomas in adults," (in English), *Oncology,* vol. 58, no. 2, pp. 108-116, Jan 31 2000. [Online]. Available: http://www.ncbi.nlm.nih.gov/entrez/query.fcgi?db=pubmed&cmd=Retrieve&dopt=AbstractPlus&list_uids=10705237.

[18] N. Sanai, M.-Y. Polley, and M. S. Berger, "Insular glioma resection: assessment of patient morbidity, survival, and tumor progression," (in English), *J Neurosurg,* vol. 112, no. 1, pp. 1-9, Dec 31 2010, doi: 10.3171/2009.6.JNS0952.

[19] E. Shaw *et al.*, "Prospective randomized trial of low- versus high-dose radiation therapy in adults with supratentorial low-grade glioma: initial report of a North Central Cancer Treatment Group/Radiation Therapy Oncology Group/Eastern Cooperative Oncology Group study," (in eng), *J Clin Oncol,* vol. 20, no. 9, pp. 2267-76, May 1 2002. [Online]. Available: http://www.ncbi.nlm.nih.gov/entrez/query.fcgi?db=pubmed&cmd=Retrieve&dopt=AbstractPlus&list_uids=11980997.

[20] J. S. Smith *et al.*, "Role of extent of resection in the long-term outcome of low-grade hemispheric gliomas," (in English), *J Clin Oncol,* vol. 26, no. 8, pp. 1338-1345, Mar 09 2008, doi: 10.1200/JCO.2007.13.9337.

[21] S.-A. Yeh *et al.*, "Treatment outcomes and prognostic factors of patients with supratentorial low-grade oligodendroglioma," (in English), *Int J Radiat Oncol Biol Phys,* vol. 54, no. 5, pp. 1405-1409, Nov 30 2002. [Online]. Available: http://www.ncbi.nlm.nih.gov/entrez/query.fcgi?db=pubmed&cmd=Retrieve&dopt=AbstractPlus&list_uids=12459363.

[22] P. D. Brown *et al.*, "A prospective study of quality of life in adults with newly diagnosed high-grade gliomas: the impact of the extent of resection on quality of life and survival," (in English), *Neurosurgery,* vol. 57, no. 3, pp. 495-504- discussion 495-504, Aug 31 2005. [Online]. Available: http://www.ncbi.nlm.nih.gov/entrez/query.fcgi?db=pubmed&cmd=Retrieve&dopt=AbstractPlus&list_uids=16145528.

[23] K. L. Chaichana *et al.*, "Factors involved in maintaining prolonged functional independence following supratentorial glioblastoma resection. Clinical article," (in English), *J Neurosurg,* vol. 114, no. 3, pp. 604-612, Feb 28 2011, doi: 10.3171/2010.4.JNS091340.

[24] K. L. Chaichana *et al.*, "Prognostic significance of contrast-enhancing anaplastic astrocytomas in adults," (in English), *J Neurosurg,* vol. 113, no. 2, pp. 286-292, Jul 31 2010, doi: 10.3171/2010.2.JNS091010.

[25] A. M. Stark, A. Nabavi, H. M. Mehdorn, and U. Blömer, "Glioblastoma multiforme-report of 267 cases treated at a single institution," (in English), *Surg Neurol,* vol. 63, no. 2, pp. 162-9- discussion 169, Jan 31 2005, doi: 10.1016/j.surneu.2004.01.028.

[26] Y. Ushio, M. Kochi, J.-i. Hamada, Y. Kai, and H. Nakamura, "Effect of surgical removal on survival and quality of life in patients with supratentorial glioblastoma," (in English), *Neurol Med Chir (Tokyo),* vol. 45, no. 9, pp. 454-60- discussion 460-1, Aug 31 2005. [Online]. Available: http://www.ncbi.nlm.nih.gov/entrez/query.fcgi?db=pubmed&cmd=Retrieve&dopt=AbstractPlus&list_uids=16195644.

[27] L. Wei, D. Roberts, N. Sanai, and J. T. C. Liu, "Visualization technologies for 5-ALA-based fluorescence-guided surgeries," *J Neuro-Oncol,* 2019.

[28] J. T. Liu, D. Meza, and N. Sanai, "Trends in fluorescence image-guided surgery for gliomas," *Neurosurgery,* vol. 75, no. 1, pp. 61-71, Jul 2014, doi: 10.1227/NEU.0000000000000344.

[29] G. E. Moore, W. T. Peyton, and et al., "The clinical use of sodium fluorescein and radioactive diiodofluorescein in the localization of tumors of the central nervous system," *Minn Med,* vol. 31, no. 10, pp. 1073-6, Oct 1948. [Online]. Available: https://www.ncbi.nlm.nih.gov/pubmed/18888792.

[30] G. E. Moore, W. T. Peyton, and et al., "The clinical use of fluorescein in neurosurgery; the localization of brain tumors," *J Neurosurg,* vol. 5, no. 4, pp. 392-8, Jul 1948, doi: 10.3171/jns.1948.5.4.0392.

[31] E. Belykh *et al.*, "Diagnostic Accuracy of a Confocal Laser Endomicroscope for In Vivo Differentiation Between Normal Injured And Tumor Tissue During Fluorescein-Guided Glioma Resection: Laboratory Investigation," *World Neurosurg,* vol. 115, pp. e337-e348, Jul 2018, doi: 10.1016/j.wneu.2018.04.048.

[32] N. L. Martirosyan *et al.*, "Potential application of a handheld confocal endomicroscope imaging system using a variety of fluorophores in experimental gliomas and normal brain," (in English), *Neurosurgical Focus,* vol. 36, no. 2, Feb 2014, doi: Artn E16
10.3171/2013.11.Focus13486.

[33] M. Behbahaninia *et al.*, "Intraoperative fluorescent imaging of intracranial tumors: A review," (in English), *Clin Neurol Neurosur,* vol. 115, no. 5, pp. 517-528, May 2013, doi: 10.1016/j.clineuro.2013.02.019.

[34] E. Belykh *et al.*, "Utilization of intraoperative confocal laser endomicroscopy in brain tumor surgery," *J Neurosurg Sci,* Aug 28 2018, doi: 10.23736/S0390-5616.18.04553-8.

[35] B. W. Pogue, S. Gibbs-Strauss, P. A. Valdes, K. Samkoe, D. W. Roberts, and K. D. Paulsen, "Review of Neurosurgical Fluorescence Imaging Methodologies," *IEEE J Sel Top Quantum Electron,* vol. 16, no. 3, pp. 493-505, May 2010, doi: 10.1109/JSTQE.2009.2034541.

[36] N. Sanai *et al.*, "Intraoperative confocal microscopy for brain tumors: a feasibility analysis in humans," *Neurosurgery,* vol. 68, no. 2 Suppl Operative, pp. 282-90; discussion 290, Jun 2011, doi: 10.1227/NEU.0b013e318212464e.

[37] H. G. Schlosser, O. Suess, P. Vajkoczy, F. K. van Landeghem, M. Zeitz, and C. Bojarski, "Confocal neurolasermicroscopy in human brain - perspectives for neurosurgery on a

cellular level (including additional comments to this article)," *Cent Eur Neurosurg,* vol. 71, no. 1, pp. 13-9, Feb 2010, doi: 10.1055/s-0029-1237735.

[38] W. Gobel, J. N. Kerr, A. Nimmerjahn, and F. Helmchen, "Miniaturized two-photon microscope based on a flexible coherent fiber bundle and a gradient-index lens objective," *Opt Lett,* vol. 29, no. 21, pp. 2521-3, Nov 1 2004. [Online]. Available: https://www.ncbi.nlm.nih.gov/pubmed/15584281.

[39] F. Helmchen, M. S. Fee, D. W. Tank, and W. Denk, "A miniature head-mounted two-photon microscope. high-resolution brain imaging in freely moving animals," *Neuron,* vol. 31, no. 6, pp. 903-12, Sep 27 2001. [Online]. Available: https://www.ncbi.nlm.nih.gov/pubmed/11580892.

[40] B. A. Flusberg, J. C. Jung, E. D. Cocker, E. P. Anderson, and M. J. Schnitzer, "In vivo brain imaging using a portable 3.9 gram two-photon fluorescence microendoscope," *Opt Lett,* vol. 30, no. 17, pp. 2272-4, Sep 1 2005. [Online]. Available: https://www.ncbi.nlm.nih.gov/pubmed/16190441.

[41] W. Piyawattanametha *et al.*, "Fast-scanning two-photon fluorescence imaging based on a microelectromechanical systems two- dimensional scanning mirror," *Opt Lett,* vol. 31, no. 13, pp. 2018-20, Jul 1 2006. [Online]. Available: https://www.ncbi.nlm.nih.gov/pubmed/16770418.

[42] J. T. Liu *et al.*, "Micromirror-scanned dual-axis confocal microscope utilizing a gradient-index relay lens for image guidance during brain surgery," *J Biomed Opt,* vol. 15, no. 2, p. 026029, Mar-Apr 2010, doi: 10.1117/1.3386055.

[43] Y. Xiang *et al.*, "Blood-Brain Barrier Disruption, Sodium Fluorescein, And Fluorescence-Guided Surgery Of Gliomas," *Br J Neurosurg,* vol. 32, no. 2, pp. 141-148, Apr 2018, doi: 10.1080/02688697.2018.1428731.

[44] J. Eschbacher *et al.*, "In vivo intraoperative confocal microscopy for real-time histopathological imaging of brain tumors," *J Neurosurg,* vol. 116, no. 4, pp. 854-60, Apr 2012, doi: 10.3171/2011.12.JNS11696.

[45] W. Stummer *et al.*, "Fluorescence-guided surgery with 5-aminolevulinic acid for resection of malignant glioma: a randomised controlled multicentre phase III trial," *Lancet Oncol,* vol. 7, no. 5, pp. 392-401, May 2006, doi: 10.1016/S1470-2045(06)70665-9.

[46] P. A. Valdes *et al.*, "Quantitative fluorescence using 5-aminolevulinic acid-induced protoporphyrin IX biomarker as a surgical adjunct in low-grade glioma surgery," *J Neurosurg,* vol. 123, no. 3, pp. 771-80, Sep 2015, doi: 10.3171/2014.12.JNS14391.

[47] E. Belykh *et al.*, "Scanning Fiber Endoscope Improves Detection of 5-Aminolevulinic Acid-Induced Protoporphyrin IX Fluorescence at the Boundary of Infiltrative Glioma," *World Neurosurg,* vol. 113, pp. e51-e69, May 2018, doi: 10.1016/j.wneu.2018.01.151.

[48] P. A. Valdes, F. Leblond, V. L. Jacobs, B. C. Wilson, K. D. Paulsen, and D. W. Roberts, "Quantitative, spectrally-resolved intraoperative fluorescence imaging," *Sci Rep,* vol. 2, p. 798, 2012, doi: 10.1038/srep00798.

[49] J. C. O. Richter, N. Haj-Hosseini, M. Hallbeck, and K. Wardell, "Combination of hand-held probe and microscopy for fluorescence guided surgery in the brain tumor marginal zone," *Photodiagnosis Photodyn Ther,* vol. 18, pp. 185-192, Jun 2017, doi: 10.1016/j.pdpdt.2017.01.188.

[50] S. D. Konecky *et al.*, "Spatial frequency domain tomography of protoporphyrin IX fluorescence in preclinical glioma models," *J Biomed Opt,* vol. 17, no. 5, p. 056008, May 2012, doi: 10.1117/1.JBO.17.5.056008.

[51] D. S. Kepshire *et al.*, "Imaging of glioma tumor with endogenous fluorescence tomography," *J Biomed Opt,* vol. 14, no. 3, p. 030501, May-Jun 2009, doi: 10.1117/1.3127202.

[52] A. Kim, M. Roy, F. N. Dadani, and B. C. Wilson, "Topographic mapping of subsurface fluorescent structures in tissue using multiwavelength excitation," *J Biomed Opt,* vol. 15, no. 6, p. 066026, Nov-Dec 2010, doi: 10.1117/1.3523369.

[53] F. Leblond *et al.*, "Analytic expression of fluorescence ratio detection correlates with depth in multi-spectral sub-surface imaging," *Phys Med Biol,* vol. 56, no. 21, pp. 6823-37, Nov 7 2011, doi: 10.1088/0031-9155/56/21/005.

[54] K. K. Kolste *et al.*, "Macroscopic optical imaging technique for wide-field estimation of fluorescence depth in optically turbid media for application in brain tumor surgical guidance," *J Biomed Opt,* vol. 20, no. 2, p. 26002, Feb 2015, doi: 10.1117/1.JBO.20.2.026002.

[55] M. Jermyn *et al.*, "Macroscopic-imaging technique for subsurface quantification of near-infrared markers during surgery," *J Biomed Opt,* vol. 20, no. 3, p. 036014, Mar 2015, doi: 10.1117/1.JBO.20.3.036014.

[56] D. W. Roberts *et al.*, "Red-light excitation of protoporphyrin IX fluorescence for subsurface tumor detection," *J Neurosurg,* vol. 128, no. 6, pp. 1690-1697, Jun 2018, doi: 10.3171/2017.1.JNS162061.

[57] J. C. Tonn and W. Stummer, "Fluorescence-guided resection of malignant gliomas using 5-aminolevulinic acid: practical use, risks, and pitfalls," *Clin Neurosurg,* vol. 55, pp. 20-6, 2008. [Online]. Available: https://www.ncbi.nlm.nih.gov/pubmed/19248665.

[58] W. Stummer *et al.*, "Intraoperative detection of malignant gliomas by 5-aminolevulinic acid-induced porphyrin fluorescence," *Neurosurgery,* vol. 42, no. 3, pp. 518-25; discussion 525-6, Mar 1998. [Online]. Available: http://www.ncbi.nlm.nih.gov/pubmed/9526986.

[59] W. Stummer, H. Stepp, G. Moller, A. Ehrhardt, M. Leonhard, and H. J. Reulen, "Technical principles for protoporphyrin-IX-fluorescence guided microsurgical resection of malignant glioma tissue," *Acta Neurochir (Wien),* vol. 140, no. 10, pp. 995-1000, 1998. [Online]. Available: http://www.ncbi.nlm.nih.gov/pubmed/9856241.

[60] P. A. Valdes, D. W. Roberts, F. K. Lu, and A. Golby, "Optical technologies for intraoperative neurosurgical guidance," *Neurosurg Focus,* vol. 40, no. 3, p. E8, Mar 2016, doi: 10.3171/2015.12.FOCUS15550.

[61] E. Belykh *et al.*, "Intraoperative Fluorescence Imaging for personalized Brain Tumor Resection: Current State and Future Directions," (in English), *Front Surg,* vol. 3, Oct 17 2016, doi: UNSP 55
10.3389/fsurg.2016.00055.

[62] Y. Tamura, T. Kuroiwa, Y. Kajimoto, Y. Miki, S. Miyatake, and M. Tsuji, "Endoscopic identification and biopsy sampling of an intraventricular malignant glioma using a 5-aminolevulinic acid-induced protoporphyrin IX fluorescence imaging system. Technical note," *J Neurosurg,* vol. 106, no. 3, pp. 507-10, Mar 2007, doi: 10.3171/jns.2007.106.3.507.

[63] N. Haj-Hosseini, J. Richter, S. Andersson-Engels, and K. Wårdell, "Photobleaching behavior of protoporphyrin IX during 5-aminolevulinic acid marked glioblastoma detection," 2009, vol. 7161, pp. 716131-716131-8. [Online]. Available: http://dx.doi.org/10.1117/12.808156. [Online]. Available: http://dx.doi.org/10.1117/12.808156

[64] A. A. Potapov *et al.*, "First experience in 5-ALA fluorescence-guided and endoscopically assisted microsurgery of brain tumors," *Medical Laser Application,* vol. 23, no. 4, pp. 202-208, 2008/11/01/ 2008, doi: https://doi.org/10.1016/j.mla.2008.07.006.

[65] P. A. Valdes *et al.*, "Quantitative fluorescence in intracranial tumor: implications for ALA-induced PpIX as an intraoperative biomarker," (in English), *Journal of Neurosurgery,* vol. 115, no. 1, pp. 11-17, Jul 2011, doi: 10.3171/2011.2.Jns101451.

[66] N. Haj-Hosseini, J. Richter, S. Andersson-Engels, and K. Wardell, "Optical touch pointer for fluorescence guided glioblastoma resection using 5-aminolevulinic acid," *Lasers Surg Med,* vol. 42, no. 1, pp. 9-14, Jan 2010, doi: 10.1002/lsm.20868.

[67] A. Kim, M. Khurana, Y. Moriyama, and B. C. Wilson, "Quantification of in vivo fluorescence decoupled from the effects of tissue optical properties using fiber-optic spectroscopy measurements," (in English), *Journal of Biomedical Optics,* vol. 15, no. 6, Nov-Dec 2010, doi: Artn 067006

10.1117/1.3523616.

[68] R. Ishihara, Y. Katayama, T. Watanabe, A. Yoshino, T. Fukushima, and K. Sakatani, "Quantitative spectroscopic analysis of 5-aminolevulinic acid-induced protoporphyrin IX fluorescence intensity in diffusely infiltrating astrocytomas," *Neurol Med Chir (Tokyo),* vol. 47, no. 2, pp. 53-7; discussion 57, Feb 2007. [Online]. Available: http://www.ncbi.nlm.nih.gov/pubmed/17317941.

[69] S. Utsuki *et al.*, "Possibility of using laser spectroscopy for the intraoperative detection of nonfluorescing brain tumors and the boundaries of brain tumor infiltrates - Technical note," (in English), *Journal of Neurosurgery,* vol. 104, no. 4, pp. 618-620, Apr 2006, doi: DOI 10.3171/jns.2006.104.4.618.

[70] W. Stummer *et al.*, "5-Aminolevulinic acid-derived tumor fluorescence: the diagnostic accuracy of visible fluorescence qualities as corroborated by spectrometry and histology and postoperative imaging," *Neurosurgery,* vol. 74, no. 3, pp. 310-9; discussion 319-20, Mar 2014, doi: 10.1227/NEU.0000000000000267.

[71] P. A. Valdes, V. L. Jacobs, B. C. Wilson, F. Leblond, D. W. Roberts, and K. D. Paulsen, "System and methods for wide-field quantitative fluorescence imaging during neurosurgery," *Opt Lett,* vol. 38, no. 15, pp. 2786-8, Aug 1 2013, doi: 10.1364/OL.38.002786.

[72] J. J. Bravo, J. D. Olson, S. C. Davis, D. W. Roberts, K. D. Paulsen, and S. C. Kanick, "Hyperspectral data processing improves PpIX contrast during fluorescence guided surgery of human brain tumors," *Sci Rep,* vol. 7, no. 1, p. 9455, Aug 25 2017, doi: 10.1038/s41598-017-09727-8.

[73] N. A. Markwardt, N. Haj-Hosseini, B. Hollnburger, H. Stepp, P. Zelenkov, and A. Ruhm, "405 nm versus 633 nm for protoporphyrin IX excitation in fluorescence-guided stereotactic biopsy of brain tumors," *J Biophotonics,* vol. 9, no. 9, pp. 901-12, Sep 2016, doi: 10.1002/jbio.201500195.

[74] D. J. Cuccia, F. Bevilacqua, A. J. Durkin, and B. J. Tromberg, "Modulated imaging: quantitative analysis and tomography of turbid media in the spatial-frequency domain," *Opt Lett,* vol. 30, no. 11, pp. 1354-6, Jun 1 2005. [Online]. Available: https://www.ncbi.nlm.nih.gov/pubmed/15981531.

[75] D. Wirth, K. Kolste, S. Kanick, D. W. Roberts, F. Leblond, and K. D. Paulsen, "Fluorescence depth estimation from wide-field optical imaging data for guiding brain tumor resection: a multi-inclusion phantom study," *Biomed Opt Express,* vol. 8, no. 8, pp. 3656-3670, Aug 1 2017, doi: 10.1364/BOE.8.003656.

[76] A. F. Gmitro and D. Aziz, "Confocal microscopy through a fiber-optic imaging bundle," *Opt. Lett.,* vol. 18, no. 8, pp. 565-567, 1993/04/15 1993, doi: 10.1364/OL.18.000565.

[77] R. R.-K. L. S. S. B. R. Descour, "Fiber-optic confocal imaging apparatus and methods of use," Patent US6370422B1, 2002.

[78] J. A. Udovich, N. D. Kirkpatrick, A. Kano, A. Tanbakuchi, U. Utzinger, and A. F. Gmitro, "Spectral background and transmission characteristics of fiber optic imaging bundles," (in English), *Appl Optics,* vol. 47, no. 25, pp. 4560-4568, Sep 1 2008, doi: 10.1364/Ao.47.004560.

[79] D. Wang, Y. Chen, Y. Wang, and J. T. Liu, "Comparison of line-scanned and point-scanned dual-axis confocal microscope performance," *Opt Lett,* vol. 38, no. 24, pp. 5280-3, Dec 15 2013, doi: 10.1364/OL.38.005280.

[80] C. Yin *et al.*, "Miniature in vivo MEMS-based line-scanned dual-axis confocal microscope for point-of-care pathology," *Biomed Opt Express,* vol. 7, no. 2, pp. 251-63, Feb 1 2016, doi: 10.1364/BOE.7.000251.

[81] K. B. Sung *et al.*, "Near real time in vivo fibre optic confocal microscopy: sub-cellular structure resolved," *J Microsc,* vol. 207, no. Pt 2, pp. 137-45, Aug 2002. [Online]. Available: https://www.ncbi.nlm.nih.gov/pubmed/12180959.

[82] H. J. Shin, M. C. Pierce, D. Lee, H. Ra, O. Solgaard, and R. Richards-Kortum, "Fiber-optic confocal microscope using a MEMS scanner and miniature objective lens," (in English), *Optics Express,* vol. 15, no. 15, pp. 9113-9122, Jul 23 2007, doi: Doi 10.1364/Oe.15.009113.

[83] L. Liu, E. K. Wang, X. Y. Zhang, W. X. Liang, X. D. Li, and H. K. Xie, "MEMS-based 3D confocal scanning microendoscope using MEMS scanners for both lateral and axial scan," (in English), *Sensor Actuat a-Phys,* vol. 215, pp. 89-95, Aug 15 2014, doi: 10.1016/j.sna.2013.09.035.

[84] K. Carlson *et al.*, "In vivo fiber-optic confocal reflectance microscope with an injection-molded plastic miniature objective lens," (in English), *Appl Optics,* vol. 44, no. 10, pp. 1792-1797, Apr 1 2005, doi: Doi 10.1364/Ao.44.001792.

[85] C. Olsovsky *et al.*, "Handheld tunable focus confocal microscope utilizing a double-clad fiber coupler for in vivo imaging of oral epithelium," (in English), *Journal of Biomedical Optics,* vol. 22, no. 5, May 2017, doi: Artn 056008
10.1117/1.Jbo.22.5.056008.

[86] R. Richards-Kortum, C. L. Smithpeter, B. S. Bowman, and M. R. Descour, "Fiber-optic confocal imaging apparatus and methods of use," ed: Google Patents, 2002.

[87] F. BERIER, S. BOURRIAUX, M. Genet, B. Viellerobe, A. Loiseau, and B. Abrat, "Miniaturized focusing optical head in particular for endoscope," ed: Google Patents, 2003.

[88] M. Kanai, "Condensing optical system, confocal optical system, and scanning confocal endoscope," ed: Google Patents, 2005.

[89] K. Kumar *et al.*, "Handheld histology-equivalent sectioning laser-scanning confocal optical microscope for interventional imaging," *Biomed Microdevices,* vol. 12, no. 2, pp. 223-33, Apr 2010, doi: 10.1007/s10544-009-9377-6.

[90] A. A. Tanbakuchi, A. R. Rouse, J. A. Udovich, K. D. Hatch, and A. F. Gmitro, "Clinical confocal microlaparoscope for real-time in vivo optical biopsies," *J Biomed Opt,* vol. 14, no. 4, p. 044030, Jul-Aug 2009, doi: 10.1117/1.3207139.

[91] T. D. Wang *et al.*, "Functional imaging of colonic mucosa with a fibered confocal microscope for real-time in vivo pathology," *Clin Gastroenterol Hepatol,* vol. 5, no. 11, pp. 1300-5, Nov 2007, doi: 10.1016/j.cgh.2007.07.013.

[92] E. J. Seibel, C. M. Brown, J. A. Dominitz, and M. B. Kimmey, "Scanning single fiber endoscopy: a new platform technology for integrated laser imaging, diagnosis, and future therapies," *Gastrointest Endosc Clin N Am,* vol. 18, no. 3, pp. 467-78, viii, Jul 2008, doi: 10.1016/j.giec.2008.05.001.

[93] C. M. Lee, C. J. Engelbrecht, T. D. Soper, F. Helmchen, and E. J. Seibel, "Scanning fiber endoscopy with highly flexible, 1 mm catheterscopes for wide-field, full-color imaging," *J Biophotonics,* vol. 3, no. 5-6, pp. 385-407, Jun 2010, doi: 10.1002/jbio.200900087.

[94] R. Kiesslich *et al.*, "Confocal laser endoscopy for diagnosing intraepithelial neoplasias and colorectal cancer in vivo," *Gastroenterology,* vol. 127, no. 3, pp. 706-13, Sep 2004. [Online]. Available: https://www.ncbi.nlm.nih.gov/pubmed/15362025.

[95] A. L. Polglase, W. J. McLaren, S. A. Skinner, R. Kiesslich, M. F. Neurath, and P. M. Delaney, "A fluorescence confocal endomicroscope for in vivo microscopy of the upper- and the lower-GI tract," *Gastrointest Endosc,* vol. 62, no. 5, pp. 686-95, Nov 2005, doi: 10.1016/j.gie.2005.05.021.

[96] K. Kumar, K. Hoshino, and X. Zhang, "Handheld subcellular-resolution single-fiber confocal microscope using high-reflectivity two-axis vertical combdrive silicon microscanner," *Biomed Microdevices,* vol. 10, no. 5, pp. 653-60, Oct 2008, doi: 10.1007/s10544-008-9176-5.

[97] A. A. Tanbakuchi, J. A. Udovich, A. R. Rouse, K. D. Hatch, and A. F. Gmitro, "In vivo imaging of ovarian tissue using a novel confocal microlaparoscope," *Am J Obstet Gynecol,* vol. 202, no. 1, pp. 90 e1-9, Jan 2010, doi: 10.1016/j.ajog.2009.07.027.

[98] C. L. Hoy *et al.*, "Miniaturized probe for femtosecond laser microsurgery and two-photon imaging," *Opt Express,* vol. 16, no. 13, pp. 9996-10005, Jun 23 2008. [Online]. Available: https://www.ncbi.nlm.nih.gov/pubmed/18575570.

[99] M. T. Myaing, D. J. MacDonald, and X. Li, "Fiber-optic scanning two-photon fluorescence endoscope," *Opt Lett,* vol. 31, no. 8, pp. 1076-8, Apr 15 2006. [Online]. Available: https://www.ncbi.nlm.nih.gov/pubmed/16625908.

[100] K. Murari, Y. Zhang, S. Li, Y. Chen, M. J. Li, and X. Li, "Compensation-free, all-fiber-optic, two-photon endomicroscopy at 1.55 mum," *Opt Lett,* vol. 36, no. 7, pp. 1299-301, Apr 1 2011, doi: 10.1364/OL.36.001299.

[101] X. Li, C. Chudoba, T. Ko, C. Pitris, and J. G. Fujimoto, "Imaging needle for optical coherence tomography," *Opt Lett,* vol. 25, no. 20, pp. 1520-2, Oct 15 2000. [Online]. Available: http://www.ncbi.nlm.nih.gov/pubmed/18066265.

[102] N. Bozinovic, C. Ventalon, T. Ford, and J. Mertz, "Fluorescence endomicroscopy with structured illumination," *Opt Express,* vol. 16, no. 11, pp. 8016-25, May 26 2008. [Online]. Available: https://www.ncbi.nlm.nih.gov/pubmed/18545511.

[103] T. N. Ford, D. Lim, and J. Mertz, "Fast optically sectioned fluorescence HiLo endomicroscopy," *J Biomed Opt,* vol. 17, no. 2, p. 021105, Feb 2012, doi: 10.1117/1.JBO.17.2.021105.

[104] M. Kyrish *et al.*, "Needle-based fluorescence endomicroscopy via structured illumination with a plastic, achromatic objective," *J Biomed Opt,* vol. 18, no. 9, p. 096003, Sep 2013, doi: 10.1117/1.JBO.18.9.096003.

[105] J. T. Liu *et al.*, "Miniature near-infrared dual-axes confocal microscope utilizing a two-dimensional microelectromechanical systems scanner," *Opt Lett,* vol. 32, no. 3, pp. 256-8, Feb 1 2007. [Online]. Available: https://www.ncbi.nlm.nih.gov/pubmed/17215937.

[106] M. Minsky, "Microscopy apparatus," ed: Google Patents, 1961.

[107] E. H. K. Stelzer and S. Lindek, "Fundamental Reduction of the Observation Volume in Far-Field Light-Microscopy by Detection Orthogonal to the Illumination Axis - Confocal Theta Microscopy," (in English), *Optics Communications,* vol. 111, no. 5-6, pp. 536-547, Oct 15 1994, doi: Doi 10.1016/0030-4018(94)90533-9.

[108] C. J. Cogswell, S. Lindek, E. H. Stelzer, and K. Carlsson, "<title>Confocal theta microscopy and 4Pi-confocal theta microscopy</title>," vol. 2184, pp. 188-194, 1994, doi: 10.1117/12.172093.

[109] S. Lindek and E. H. Stelzer, "Resolution improvement by nonconfocal theta microscopy," *Opt Lett,* vol. 24, no. 21, pp. 1505-7, Nov 1 1999. [Online]. Available: https://www.ncbi.nlm.nih.gov/pubmed/18079847.

[110] T. D. Wang, M. J. Mandella, C. H. Contag, and G. S. Kino, "Dual-axis confocal microscope for high-resolution in vivo imaging," *Opt Lett,* vol. 28, no. 6, pp. 414-6, Mar 15 2003. [Online]. Available: https://www.ncbi.nlm.nih.gov/pubmed/12659264.

[111] R. H. Webb and F. Rogomentich, "Confocal microscope with large field and working distance," *Appl Opt,* vol. 38, no. 22, pp. 4870-5, Aug 1 1999. [Online]. Available: https://www.ncbi.nlm.nih.gov/pubmed/18323977.

[112] T. D. Wang, C. H. Contag, M. J. Mandella, N. Y. Chan, and G. S. Kino, "Dual-axes confocal microscopy with post-objective scanning and low-coherence heterodyne detection," *Opt Lett,* vol. 28, no. 20, pp. 1915-7, Oct 15 2003. [Online]. Available: https://www.ncbi.nlm.nih.gov/pubmed/14587774.

[113] L. K. Wong, M. J. Mandella, G. S. Kino, and T. D. Wang, "Improved rejection of multiply scattered photons in confocal microscopy using dual-axes architecture," *Opt Lett,* vol. 32, no. 12, pp. 1674-6, Jun 15 2007. [Online]. Available: https://www.ncbi.nlm.nih.gov/pubmed/17572743.

[114] J. T. Liu, M. J. Mandella, J. M. Crawford, C. H. Contag, T. D. Wang, and G. S. Kino, "Efficient rejection of scattered light enables deep optical sectioning in turbid media with low-numerical-aperture optics in a dual-axis confocal architecture," *J Biomed Opt,* vol. 13, no. 3, p. 034020, May-Jun 2008, doi: 10.1117/1.2939428.

[115] J. T. Liu *et al.*, "Dual-axes confocal reflectance microscope for distinguishing colonic neoplasia," *J Biomed Opt,* vol. 11, no. 5, p. 054019, Sep-Oct 2006, doi: 10.1117/1.2363363.

[116] E. W. M. Born, *Principles of Optics, 7th ed.,* . Cambridge, UK: Cambridgge Press, 1999.

[117] J. Pawley, *Handbook of Biological Confocal Microscopy*. Springer, 2006.

[118] M. Rajadhyaksha, R. R. Anderson, and R. H. Webb, "Video-rate confocal scanning laser microscope for imaging human tissues in vivo," *Appl Opt,* vol. 38, no. 10, pp. 2105-15, Apr 1 1999. [Online]. Available: https://www.ncbi.nlm.nih.gov/pubmed/18319771.

[119] T. R. Corle, C. H. Chou, and G. S. Kino, "Depth response of confocal optical microscopes," *Opt Lett,* vol. 11, no. 12, pp. 770-2, Dec 1 1986. [Online]. Available: https://www.ncbi.nlm.nih.gov/pubmed/19738754.

[120] C. J. Sheppard and T. Wilson, "Depth of field in the scanning microscope," *Opt Lett,* vol. 3, no. 3, p. 115, Sep 1 1978. [Online]. Available: https://www.ncbi.nlm.nih.gov/pubmed/19684715.

[121] H. W. Robert, "Confocal optical microscopy," *Reports on Progress in Physics,* vol. 59, no. 3, p. 427, 1996. [Online]. Available: http://stacks.iop.org/0034-4885/59/i=3/a=003.

[122] Y. Chen and J. T. Liu, "Optimizing the performance of dual-axis confocal microscopes via Monte-Carlo scattering simulations and diffraction theory," *J Biomed Opt,* vol. 18, no. 6, p. 066006, Jun 2013, doi: 10.1117/1.JBO.18.6.066006.

[123] Y. Chen, D. Wang, and J. T. Liu, "Assessing the tissue-imaging performance of confocal microscope architectures via Monte Carlo simulations," *Opt Lett,* vol. 37, no. 21, pp. 4495-7, Nov 1 2012, doi: 10.1364/OL.37.004495.

[124] D. Meza, D. Wang, Y. Wang, S. Borwege, N. Sanai, and J. T. Liu, "Comparing high-resolution microscopy techniques for potential intraoperative use in guiding low-grade glioma resections," *Lasers Surg Med,* vol. 47, no. 4, pp. 289-95, Apr 2015, doi: 10.1002/lsm.22347.

[125] L. Wei, Y. Chen, C. Yin, S. Borwege, N. Sanai, and J. T. C. Liu, "Optical-sectioning microscopy of protoporphyrin IX fluorescence in human gliomas: standardization and quantitative comparison with histology," *J Biomed Opt,* vol. 22, no. 4, p. 46005, Apr 1 2017, doi: 10.1117/1.JBO.22.4.046005.

[126] H. Ra, W. Piyawattanametha, Y. Taguchi, D. Lee, M. J. Mandella, and O. Solgaard, "Two-dimensional MEMS scanner for dual-axes confocal microscopy," (in English), *J Microelectromech S,* vol. 16, no. 4, pp. 969-976, Aug 2007, doi: 10.1109/Jmems.2007.892900.

[127] Y. Chen, A. Glaser, and J. T. Liu, "Bessel-beam illumination in dual-axis confocal microscopy mitigates resolution degradation caused by refractive heterogeneities," *J Biophotonics,* vol. 10, no. 1, pp. 68-74, Jan 2017, doi: 10.1002/jbio.201600196.

[128] S. Y. Leigh, Y. Chen, and J. T. Liu, "Modulated-alignment dual-axis (MAD) confocal microscopy for deep optical sectioning in tissues," *Biomed Opt Express,* vol. 5, no. 6, pp. 1709-20, Jun 1 2014, doi: 10.1364/BOE.5.001709.

[129] Y. Chen *et al.*, "Video-rate in vivo fluorescence imaging with a line-scanned dual-axis confocal microscope," *J Biomed Opt,* vol. 20, no. 10, p. 106011, Oct 2015, doi: 10.1117/1.JBO.20.10.106011.

[130] D. Wang, D. Meza, Y. Wang, L. Gao, and J. T. Liu, "Sheet-scanned dual-axis confocal microscopy using Richardson-Lucy deconvolution," *Opt Lett,* vol. 39, no. 18, pp. 5431-4, Sep 15 2014, doi: 10.1364/OL.39.005431.

[131] J. Huisken, J. Swoger, F. Del Bene, J. Wittbrodt, and E. H. Stelzer, "Optical sectioning deep inside live embryos by selective plane illumination microscopy," *Science,* vol. 305, no. 5686, pp. 1007-9, Aug 13 2004, doi: 10.1126/science.1100035.

[132] A. K. Glaser *et al.*, "Light-sheet microscopy for slide-free non-destructive pathology of large clinical specimens," *Nature Biomedical Engineering,* Article vol. 1, p. 0084, 06/26/online 2017, doi: 10.1038/s41551-017-0084 https://www.nature.com/articles/s41551-017-0084#supplementary-information.

[133] A. K. Glaser, Y. Wang, and J. T. Liu, "Assessing the imaging performance of light sheet microscopies in highly scattering tissues," *Biomed Opt Express,* vol. 7, no. 2, pp. 454-66, Feb 1 2016, doi: 10.1364/BOE.7.000454.

[134] N. Chen, C. H. Wong, and C. J. Sheppard, "Focal modulation microscopy," *Opt Express,* vol. 16, no. 23, pp. 18764-9, Nov 10 2008. [Online]. Available: https://www.ncbi.nlm.nih.gov/pubmed/19581963.

[135] K. Isobe *et al.*, "Background-free deep imaging by spatial overlap modulation nonlinear optical microscopy," *Biomed Opt Express,* vol. 3, no. 7, pp. 1594-608, Jul 1 2012, doi: 10.1364/BOE.3.001594.

[136] Y. Chen, A. Glaser, and J. T. C. Liu, "Bessel-beam illumination in dual-axis confocal microscopy mitigates resolution degradation caused by refractive heterogeneities," (in English), *Journal of Biophotonics,* vol. 10, no. 1, pp. 68-74, Jan 2017, doi: 10.1002/jbio.201600196.

[137] T. A. Planchon *et al.*, "Rapid three-dimensional isotropic imaging of living cells using Bessel beam plane illumination," (in English), *Nature Methods,* vol. 8, no. 5, pp. 417-U68, May 2011, doi: 10.1038/Nmeth.1586.

[138] F. O. Fahrbach, P. Simon, and A. Rohrbach, "Microscopy with self-reconstructing beams," (in English), *Nat Photonics,* vol. 4, no. 11, pp. 780-785, Nov 2010, doi: 10.1038/Nphoton.2010.204.

[139] Y. Chen and J. T. Liu, "Characterizing the beam steering and distortion of Gaussian and Bessel beams focused in tissues with microscopic heterogeneities," *Biomed Opt Express,* vol. 6, no. 4, pp. 1318-30, Apr 1 2015, doi: 10.1364/BOE.6.001318.

[140] F. O. Fahrbach, V. Gurchenkov, K. Alessandri, P. Nassoy, and A. Rohrbach, "Light-sheet microscopy in thick media using scanned Bessel beams and two-photon fluorescence excitation," *Opt Express,* vol. 21, no. 11, pp. 13824-39, Jun 3 2013, doi: 10.1364/OE.21.013824.

[141] T. A. Planchon *et al.*, "Rapid three-dimensional isotropic imaging of living cells using Bessel beam plane illumination," *Nat Methods,* vol. 8, no. 5, pp. 417-23, May 2011, doi: 10.1038/nmeth.1586.

[142] D. Lorenser, C. Christian Singe, A. Curatolo, and D. D. Sampson, "Energy-efficient low-Fresnel-number Bessel beams and their application in optical coherence tomography," *Opt Lett,* vol. 39, no. 3, pp. 548-51, Feb 1 2014, doi: 10.1364/OL.39.000548.

[143] M. Zhao *et al.*, "Cellular imaging of deep organ using two-photon Bessel light-sheet nonlinear structured illumination microscopy," *Biomed Opt Express,* vol. 5, no. 5, pp. 1296-308, May 1 2014, doi: 10.1364/BOE.5.001296.

[144] D. S. Gareau, S. Abeytunge, and M. Rajadhyaksha, "Line-scanning reflectance confocal microscopy of human skin: comparison of full-pupil and divided-pupil configurations," *Opt Lett,* vol. 34, no. 20, pp. 3235-7, Oct 15 2009, doi: 10.1364/OL.34.003235.

[145] C. J. Koester, "Scanning mirror microscope with optical sectioning characteristics: applications in ophthalmology," *Appl Opt,* vol. 19, no. 11, pp. 1749-57, Jun 1 1980, doi: 10.1364/AO.19.001749.

[146] Y. G. Patel, M. Rajadhyaksha, and C. A. Dimarzio, "Optimization of pupil design for point-scanning and line-scanning confocal microscopy," *Biomed Opt Express,* vol. 2, no. 8, pp. 2231-42, Aug 1 2011, doi: 10.1364/BOE.2.002231.

[147] P. J. Dwyer, C. A. DiMarzio, J. M. Zavislan, W. J. Fox, and M. Rajadhyaksha, "Confocal reflectance theta line scanning microscope for imaging human skin in vivo," *Opt Lett,* vol. 31, no. 7, pp. 942-4, Apr 1 2006. [Online]. Available: http://www.ncbi.nlm.nih.gov/pubmed/16599219.

[148] P. J. Dwyer, C. A. DiMarzio, and M. Rajadhyaksha, "Confocal theta line-scanning microscope for imaging human tissues," *Appl Opt,* vol. 46, no. 10, pp. 1843-51, Apr 1 2007. [Online]. Available: https://www.ncbi.nlm.nih.gov/pubmed/17356629.

[149] S. Kumar, D. Wilding, M. B. Sikkel, A. R. Lyon, K. T. MacLeod, and C. Dunsby, "High-speed 2D and 3D fluorescence microscopy of cardiac myocytes," (in English), *Optics Express,* vol. 19, no. 15, pp. 13839-13847, Jul 18 2011, doi: 10.1364/Oe.19.013839.

[150] M. B. Bouchard *et al.*, "Swept confocally-aligned planar excitation (SCAPE) microscopy for high-speed volumetric imaging of behaving organisms," (in English), *Nat Photonics,* vol. 9, no. 2, pp. 113-119, Feb 2015, doi: 10.1038/Nphoton.2014.323.

[151] W. Piyawattanametha *et al.*, "In vivo near-infrared dual-axis confocal microendoscopy in the human lower gastrointestinal tract," *J Biomed Opt,* vol. 17, no. 2, p. 021102, Feb 2012, doi: 10.1117/1.JBO.17.2.021102.

[152] G. Li *et al.*, "Visualizing Epithelial Expression in Vertical and Horizontal Planes With Dual Axes Confocal Endomicroscope Using Compact Distal Scanner," *IEEE Trans Med Imaging,* vol. 36, no. 7, pp. 1482-1490, Jul 2017, doi: 10.1109/TMI.2017.2673022.

[153] C. Glazowski *et al.*, "Compact divided-pupil line-scanning confocal microscope for investigation of human tissues," vol. 8565, p. 856523, 2013, doi: 10.1117/12.2012630.

[154] N. Iftimia *et al.*, "Combined reflectance confocal microscopy/optical coherence tomography imaging for skin burn assessment," *Biomed Opt Express,* vol. 4, no. 5, pp. 680-95, May 1 2013, doi: 10.1364/BOE.4.000680.

[155] S. L. Gibbs, B. Chen, J. A. O'Hara, P. J. Hoopes, T. Hasan, and B. W. Pogue, "Protoporphyrin IX level correlates with number of mitochondria, but increase in production correlates with tumor cell size," *Photochem Photobiol,* vol. 82, no. 5, pp. 1334-41, Sep-Oct 2006, doi: 10.1562/2006-03-11-RA-843.

[156] F. Duffner, R. Ritz, D. Freudenstein, M. Weller, K. Dietz, and J. Wessels, "Specific intensity imaging for glioblastoma and neural cell cultures with 5-aminolevulinic acid-derived protoporphyrin IX," *J Neurooncol,* vol. 71, no. 2, pp. 107-11, Jan 2005, doi: 10.1007/s11060-004-9603-2.

[157] L. D. Stefano and A. Bulgarelli, "A simple and efficient connected components labeling algorithm," in *Image Analysis and Processing, 1999. Proceedings. International Conference on*, 1999 1999, pp. 322-327, doi: 10.1109/ICIAP.1999.797615.

[158] C. J. Engelbrecht, R. S. Johnston, E. J. Seibel, and F. Helmchen, "Ultra-compact fiber-optic two-photon microscope for functional fluorescence imaging in vivo," *Opt Express,* vol. 16,

no. 8, pp. 5556-64, Apr 14 2008. [Online]. Available: https://www.ncbi.nlm.nih.gov/pubmed/18542658.

[159] P. Thevenaz and M. Unser, "User-friendly semiautomated assembly of accurate image mosaics in microscopy," *Microsc Res Tech,* vol. 70, no. 2, pp. 135-46, Feb 2007, doi: 10.1002/jemt.20393.

[160] L. Wei, C. Yin, and J. T. C. Liu, "Dual-Axis Confocal Microscopy for Point-of-Care Pathology," *IEEE Journal of Selected Topics in Quantum Electronics,* vol. 25, no. 1, pp. 1-10, 2019, doi: 10.1109/JSTQE.2018.2854572.

[161] W. Stummer, A. Novotny, H. Stepp, C. Goetz, K. Bise, and H. J. Reulen, "Fluorescence-guided resection of glioblastoma multiforme by using 5-aminolevulinic acid-induced porphyrins: a prospective study in 52 consecutive patients," *J Neurosurg,* vol. 93, no. 6, pp. 1003-13, Dec 2000, doi: 10.3171/jns.2000.93.6.1003.

[162] P. P. Panciani *et al.*, "Fluorescence and image guided resection in high grade glioma," *Clin Neurol Neurosurg,* vol. 114, no. 1, pp. 37-41, Jan 2012, doi: 10.1016/j.clineuro.2011.09.001.

[163] S. Yamada, Y. Muragaki, T. Maruyama, T. Komori, and Y. Okada, "Role of neurochemical navigation with 5-aminolevulinic acid during intraoperative MRI-guided resection of intracranial malignant gliomas," *Clin Neurol Neurosurg,* vol. 130, pp. 134-9, Mar 2015, doi: 10.1016/j.clineuro.2015.01.005.

[164] D. W. Roberts *et al.*, "Coregistered fluorescence-enhanced tumor resection of malignant glioma: relationships between delta-aminolevulinic acid-induced protoporphyrin IX fluorescence, magnetic resonance imaging enhancement, and neuropathological parameters. Clinical article," *J Neurosurg,* vol. 114, no. 3, pp. 595-603, Mar 2011, doi: 10.3171/2010.2.JNS091322.

[165] R. Diez Valle, S. Tejada Solis, M. A. Idoate Gastearena, R. Garcia de Eulate, P. Dominguez Echavarri, and J. Aristu Mendiroz, "Surgery guided by 5-aminolevulinic fluorescence in glioblastoma: volumetric analysis of extent of resection in single-center experience," *J Neurooncol,* vol. 102, no. 1, pp. 105-13, Mar 2011, doi: 10.1007/s11060-010-0296-4.

[166] M. Hefti, G. von Campe, M. Moschopulos, A. Siegner, H. Looser, and H. Landolt, "5-aminolevulinic acid induced protoporphyrin IX fluorescence in high-grade glioma surgery: a one-year experience at a single institutuion," *Swiss Med Wkly,* vol. 138, no. 11-12, pp. 180-5, Mar 22 2008, doi: 2008/11/smw-12077.

[167] F. Acerbi *et al.*, "Fluorescein-guided surgery for grade IV gliomas with a dedicated filter on the surgical microscope: preliminary results in 12 cases," *Acta Neurochir (Wien),* vol. 155, no. 7, pp. 1277-86, Jul 2013, doi: 10.1007/s00701-013-1734-9.

[168] A. Tsugu *et al.*, "Impact of the combination of 5-aminolevulinic acid-induced fluorescence with intraoperative magnetic resonance imaging-guided surgery for glioma," *World Neurosurg,* vol. 76, no. 1-2, pp. 120-7, Jul-Aug 2011, doi: 10.1016/j.wneu.2011.02.005.

[169] C. G. Hadjipanayis, G. Widhalm, and W. Stummer, "What is the Surgical Benefit of Utilizing 5-Aminolevulinic Acid for Fluorescence-Guided Surgery of Malignant Gliomas?," *Neurosurgery,* vol. 77, no. 5, pp. 663-73, Nov 2015, doi: 10.1227/NEU.0000000000000929.

[170] M. Rapp, M. Kamp, H. J. Steiger, and M. Sabel, "Endoscopic-Assisted Visualization of 5-Aminolevulinic Acid-Induced Fluorescence in Malignant Glioma Surgery: A Technical

Note," (in English), *World Neurosurgery,* vol. 82, no. 1-2, pp. E277-E279, Jul-Aug 2014, doi: 10.1016/j.wneu.2013.07.002.

[171] J. P. Belloch, V. Rovira, J. L. Llacer, P. A. Riesgo, and A. Cremades, "Fluorescence-guided surgery in high grade gliomas using an exoscope system," *Acta Neurochir (Wien),* vol. 156, no. 4, pp. 653-60, Apr 2014, doi: 10.1007/s00701-013-1976-6.

[172] H. Liao *et al.*, "An integrated diagnosis and therapeutic system using intra-operative 5-aminolevulinic-acid-induced fluorescence guided robotic laser ablation for precision neurosurgery," (in English), *Med Image Anal,* vol. 16, no. 3, pp. 754-766, Mar 31 2012, doi: 10.1016/j.media.2010.11.004.

[173] A. Nabavi *et al.*, "Five-aminolevulinic acid for fluorescence-guided resection of recurrent malignant gliomas: a phase ii study," (in eng), *Neurosurgery,* vol. 65, no. 6, pp. 1070-6; discussion 1076-7, Dec 1 2009, doi: 10.1227/01.NEU.0000360128.03597.C7.

[174] W. Stummer *et al.*, "Fluorescence-guided surgery with 5-aminolevulinic acid for resection of malignant glioma: a randomised controlled multicentre phase III trial," (in eng), *Lancet Oncol,* vol. 7, no. 5, pp. 392-401, May 1 2006, doi: 10.1016/S1470-2045(06)70665-9.

[175] J.-C. Tonn and W. Stummer, "Fluorescence-guided resection of malignant gliomas using 5-aminolevulinic acid: practical use, risks, and pitfalls," (in English), *Clin Neurosurg,* vol. 55, pp. 20-26, Dec 31 2008. [Online]. Available: http://www.ncbi.nlm.nih.gov/entrez/query.fcgi?db=pubmed&cmd=Retrieve&dopt=AbstractPlus&list_uids=19248665.

[176] P. A. Valdés *et al.*, "Quantitative fluorescence in intracranial tumor: implications for ALA-induced PpIX as an intraoperative biomarker," (in English), *J Neurosurg,* vol. 115, no. 1, pp. 11-17, Jun 30 2011, doi: 10.3171/2011.2.JNS101451.

[177] D. Lau *et al.*, "A prospective Phase II clinical trial of 5-aminolevulinic acid to assess the correlation of intraoperative fluorescence intensity and degree of histologic cellularity during resection of high-grade gliomas," *J Neurosurg,* vol. 124, no. 5, pp. 1300-9, May 2016, doi: 10.3171/2015.5.JNS1577.

[178] L. Wei, Y. Fujita, N. Sanai, and J. T. C. Liu, "Toward Quantitative Neurosurgical Guidance With High-Resolution Microscopy of 5-Aminolevulinic Acid-Induced Protoporphyrin IX," *Front Oncol,* vol. 9, p. 592, 2019, doi: 10.3389/fonc.2019.00592.

[179] N. L. Martirosyan *et al.*, "Prospective evaluation of the utility of intraoperative confocal laser endomicroscopy in patients with brain neoplasms using fluorescein sodium: experience with 74 cases," (in English), *Neurosurgical Focus,* vol. 40, no. 3, Mar 2016, doi: Artn E11
10.3171/2016.1.Focus15559.

[180] V. Pavlov *et al.*, "Intraoperative Probe-Based Confocal Laser Endomicroscopy in Surgery and Stereotactic Biopsy of Low-Grade and High-Grade Gliomas: A Feasibility Study in Humans," *Neurosurgery,* vol. 79, no. 4, pp. 604-12, Oct 2016, doi: 10.1227/NEU.0000000000001365.

[181] P. A. Valdés *et al.*, "δ-aminolevulinic acid-induced protoporphyrin IX concentration correlates with histopathologic markers of malignancy in human gliomas: the need for quantitative fluorescence-guided resection to identify regions of increasing malignancy," (in English), *Neuro-Oncology,* vol. 13, no. 8, pp. 846-856, Jul 31 2011, doi: 10.1093/neuonc/nor086.

[182] H. Yano, N. Nakayama, N. Ohe, K. Miwa, J. Shinoda, and T. Iwama, "Pathological analysis of the surgical margins of resected glioblastomas excised using photodynamic visualization with both 5-aminolevulinic acid and fluorescein sodium.," (in English), *J Neurooncol,* vol. 133, no. 2, pp. 389-397, Jun 2017, doi: 10.1007/s11060-017-2445-5.

[183] T. Yoneda *et al.*, "Spectral Radiance of Protoporphyrin IX Fluorescence and Its Histopathological Implications in 5-Aminolevulinic Acid-Guided Surgery for Glioblastoma.," (in English), *Photomedicine and laser surgery,* vol. 36, no. 5, pp. 266-272, May 2018, doi: 10.1089/pho.2017.4384.

[184] L. Wei, C. Yin, Y. Fujita, N. Sanai, and J. T. C. Liu, "Handheld line-scanned dual-axis confocal microscope with pistoned MEMS actuation for flat-field fluorescence imaging," *Opt Lett,* vol. 44, no. 3, pp. 671-674, Feb 1 2019, doi: 10.1364/OL.44.000671.

[185] T. Vercauteren, A. Perchant, X. Pennec, and N. Ayache, "Mosaicing of confocal microscopic in vivo soft tissue video sequences," (in English), *Lect Notes Comput Sc,* vol. 3749, pp. 753-760, 2005. [Online]. Available: <Go to ISI>://WOS:000233337000093.

[186] T. Vercauteren, A. Perchant, G. Malandain, X. Pennec, and N. Ayache, "Robust mosaicing with correction of motion distortions and tissue deformations for in vivo fibered microscopy," *Med Image Anal,* vol. 10, no. 5, pp. 673-92, Oct 2006, doi: 10.1016/j.media.2006.06.006.

[187] K. E. Loewke *et al.*, "In Vivo Micro-Image Mosaicing," (in English), *Ieee T Bio-Med Eng,* vol. 58, no. 1, pp. 159-171, Jan 2011, doi: 10.1109/Tbme.2010.2085082.

[188] K. Kose, M. Cordova, M. Duffy, E. S. Flores, D. H. Brooks, and M. Rajadhyaksha, "Video-mosaicing of reflectance confocal images for examination of extended areas of skin in vivo," *Br J Dermatol,* vol. 171, no. 5, pp. 1239-41, Nov 2014, doi: 10.1111/bjd.13050.

[189] K. Kose *et al.*, "Automated video-mosaicking approach for confocal microscopic imaging in vivo: an approach to address challenges in imaging living tissue and extend field of view," *Sci Rep,* vol. 7, no. 1, p. 10759, Sep 7 2017, doi: 10.1038/s41598-017-11072-9.